MEMBRANE DEGRADATION STUDIES IN PEMFCS

A Dissertation
Presented to
The Academic Faculty

by

Cheng Chen

In Partial Fulfillment
of the Requirements for the Degree
Doctor of Philosophy in the
School of Chemical & Biomolecular Engineering

Georgia Institute of Technology
August 2009

MEMBRANE DEGRADATION STUDIES IN PEMFCS

Approved by:

Dr. Thomas F. Fuller, Advisor
School of Chemical & Biomolecular Engineering
Georgia Institute of Technology

Dr. Carson J. Meredith
School of Chemical & Biomolecular Engineering
Georgia Institute of Technology

Dr. Dennis W. Hess
School of Chemical & Biomolecular Engineering
Georgia Institute of Technology

Dr. Haskell W. Beckham
School of Polymer, Textile & Fiber Engineering
Georgia Institute of Technology

Dr. William J. Koros
School of Chemical & Biomolecular Engineering
Georgia Institute of Technology

Date Approved: April 15, 2009

ACKNOWLEDGEMENTS

My first, and most earnest, acknowledgement must go to my advisor Dr. Tom Fuller. I still remember our first meeting when I was completely motivated and the first paper he assigned me was Four Golden Lessons by Nobel laureate Steven Weinberg on how to start a scientific career. Dr. Fuller gave me much freedom in developing my own idea with great patience. When I was frustrated, he was always there to support me and give advice. I was also happy to obtain teaching experience while being a TA in his class for three semesters. I would also like to acknowledge Dr. Dennis Hess for his help in starting this project. I wish to thank Dr. William Koros, who taught my mass transfer class which provided me with a solid theoretical background for the modeling study in this dissertation. I am grateful to Dr. Carson Meredith for allowing me to use high-throughput membrane characterization equipments. I would like to thank all of them and Dr. Haskell Beckham who showed great interest in my research and served as my committee members.

I cannot express enough of my appreciation to Dr. Galit Levitin for her consistent help with XPS measurement. I would also like to acknowledge Dr. Cheng-Tsung Lee from Dr. Cliff Henderson's group for the FTIR studies in this work. Special thanks to Mr. Keith Reed from Dr. Carson Meredith's group for helping me with the measurement of membrane properties.

Sincere appreciation is due to all my research group members for their support during my PhD work. I would like to acknowledge Dr. Wu Bi for help with SEM measurement. I always enjoy discussing with Mr. Kevin Gallagher, Ms. Rajeswari Chandrasekaran and Mr. Norimitsu Takeuchi and learnt a lot from them. Also, I have to thank Mr. David Wong for helping me prepare MEA samples and my supervised undergraduate student Mr. Brian Pinckney for the experimental work on FER studies.

Finally, I am particularly indebted to my parents who provided unlimited support and love from China throughout the years of study and research.

TABLE OF CONTENTS

LIST OF TABLES

LIST OF FIGURES

LIST OF ABBREVIATIONS

ATR	Attenuated Total Reflection
ESCA	Electron Spectroscopy for Chemical Analysis
ESR	Electron Spin Resonance
FER	Fluoride ion Emission Rate
FTIR	Fourier Transform Infrared Spectroscopy
GDE	Gas Diffusion Electrode
GDL	Gas Diffusion Layer
HTMECH	High-Throughput Mechanical Characterization
ICP	Inductively Coupled Plasma
MEA	Membrane Electrode Assembly
NMR	Nuclear Magnetic Resonance
OCV	Open Circuit Voltage
ORR	Oxygen Reduction Reaction
PBI	Polybenzimidazole
PEMFC	Proton Exchange Membrane Fuel Cell
PFSA	Perfluorosulfonic Acid
PHI	Physical Electronics, Inc.
PTFE	Polytetrafluoroethylene
RHE	Reversible Hydrogen Electrode
SEM	Scanning Electron Microscope
SER	Sulfate ion Emission Rate
SPEEK	Poly(ether ether ketone)
TER	Trifluoroacetic acid Emission Rate

TFA	Trifluoroacetic Acid
TGA	Thermogravimetric Analysis

LIST OF SYMBOLS

Chapter 6

Roman

c	Concentration, mol m^{-3}
D	Diffusion coefficient, m^2 s^{-1}
E_a	Anode potential, V
E_c	Cathode potential, V
E_d	Active energy for O_2 diffusion in ionomer
E_{O2}	Standard potential for reaction $O_2 + 2H^+ + 2e^- \rightarrow H_2O_2$, 0.695 V
E_{H2O2}	Standard potential for reaction $H_2O_2 + 2H+ + 2e^- \rightarrow 2H_2O$, 1.763 V
Er	Effectiveness factor
F	Faraday's constant, 96485 C $equiv^{-1}$
$H_{O2,m}$	Henry's constant of O_2, J mol^{-1}
$H_{H2O2,m}$	Henry's constant of H_2O_2, J mol^{-1}
i_{O2}	Exchange current density of reaction $O_2 + 2H^+ + 2e^- \rightarrow H_2O_2$, A m^{-2}
i_{H2O2}	Exchange current density of reaction $H_2O_2 + 2H+ + 2e^- \rightarrow 2H_2O$, A m^{-2}
k_C	O_2 intrinsic reaction rate constant in the agglomerate, s^{-1}
k_{O2}	O_2 reaction rate constant at anode, s^{-1}
k_{O2}'	O_2 reaction rate constant at cathode, s^{-1}
K_{eq}	The equilibrium constant of H_2 adsorption on Pt, m^3 mol^{-1}
N_{H2O2}	H_2O_2 flux, mol m^{-2} s^{-1}

N_{O2}	O_2 flux, mol m^{-2} s^{-1}
p_{O2}	O_2 partial pressure in gas phase, kPa
p_{H2O2}	H_2O_2 partial pressure in gas phase, kPa
R	Gas constant, 8.314 J mol-1 K-1
R_i	Reaction rate of O_2/H_2O_2 at different locations (electrodes and membrane)
RH	Relative humidity
r_{agg}	Radius of the agglomerate, m
T	Temperature, K

Greek

α_{agg}	Agglomerate surface area to volume ratio, m^{-1}
α_{O2}	Cathodic transfer coefficient for reaction $O_2 + 2H^+ + 2e^- \rightarrow H_2O_2$
α_{H2O2}	Cathodic transfer coefficient for reaction $H_2O_2 + 2H^+ + 2e^- \rightarrow 2H_2O$
ε_{CL}	Porosity of catalyst layer
ε_{H2O}	Membrane water percentage
ε_{agg}	Porosity of agglomerate
δ_{agg}	Thickness of electrolyte film around agglomerate, m
ϕ_L	Spherical catalyst modulus
λ	Moles of water per mole of sulfonic acid sites

Superscript

CL	Catalyst layer

M	Membrane electrolyte
G	Gas phase
l	Liquid phase
GDL	Gas diffusion layer
agg	Agglomerate

Subscript

ref	Reference
g/m	Gas-electrolyte interface
m/s	Electrolyte-catalyst interface
eff	Effective diffusion coefficient

SUMMARY

An important challenge for PEMFC is stability and durability of the membrane separator. In this dissertation, we applied both experimental and modeling methods to investigate the chemical durability of PFSA membranes for fuel-cell applications.

Degradation data were collected and the membrane samples were analyzed by XPS after Fenton's test; FTIR was also invoked to validate the XPS results. The effects of Fe^{2+} concentration and temperature on membrane degradation were discussed. Following fuel-cell durability tests, the degraded MEA was also analyzed and results were compared with those from a fresh MEA. This is the first application of XPS to correlate surface analysis and degradation studies of Nafion® membranes. The experimental results provide evidence of chemical attack of the CF_2 backbone.

In-situ fuel-cell tests were conducted to study the effect of operating conditions such as relative humidity, oxygen partial pressure and temperature on membrane degradation by measuring FER from exhaust water. The impact of water transport was investigated by varying the humidity at each electrode of the fuel cell. An example of a long-term durability test result was also presented.

Since the level of H_2O_2 was found to be key to membrane degradation, we designed a novel spectrophotometric method to quantitatively determine H_2O_2 concentration in a fuel cell by using a multilayer MEA. The effects of relative humidity, oxygen partial pressure and membrane thickness on H_2O_2 concentration were studied. H_2O_2 emission rates were measured in anode- and cathode-only MEAs to separately study H_2O_2 formation at each electrode. In addition, a model for H_2O_2 formation,

transport, and reaction in PEMFCs is established for the first time to validate experimental data and study formation mechanism.

Catalyst agglomerates were included in this H_2O_2 formation model, thereby allowing profiles of oxygen and H_2O_2 concentration inside the fuel cell to be simulated. The average H_2O_2 concentration in the membrane was predicted under different operating conditions. Membrane properties, including membrane thickness, levels of metal ion contaminants, oxygen diffusivity, were varied to evaluate their effects on H_2O_2 concentration in the membrane. Moreover, electrode properties such as thickness, catalyst activity, *etc*. were studied to minimize H_2O_2 formation in the fuel cell. Insights to reduce the formation of H_2O_2 and to extend membrane lifetime were suggested.

The humidity effect on membrane degradation was studied by collecting vent water during the tests. The membrane conductivities and mechanical properties were measured by *ex-situ* high-throughput instruments. The ion exchange capacity of membrane samples was determined by ICP Emission Spectrometer. FTIR was applied to study both the formation of new groups and the relative abundance of existing groups in the degraded membrane. The thermal stability of degraded membranes was determined by TGA. The cross section of a degraded MEA sample was imaged with SEM to investigate the mechanical structure change. Simulation results from a simple degradation model were compared with experimental data. The representative reaction pathway in each degradation scheme was also postulated.

The effect of temperature on membrane degradation was also investigated. FERs were determined, and the apparent activation energy was calculated from an Arrhenius Equation. XPS spectra were collected from both anode and cathode sides of fuel-cell

membrane to compare the effect of temperature on each side. Atomic analysis was performed to study the impact of temperature on both backbone decomposition and side group degradation. A multilayer MEA was used to study the effects of location and thickness on membrane degradation. An improved kinetic model of membrane degradation was built to simulate the experimental data.

Finally, an attempt to mitigate membrane degradation by using peroxide decomposition reagent was performed. OCV curves were recorded during two fuel-cell durability tests with and without the addition of this additive. Both FER and TER were compared. Recommendations for the improvement of peroxide decomposition additive were suggested.

CHAPTER 1

INTRODUCTION

As the desire to reduce emissions of greenhouse gases grows, there is greater interest in commercializing carbon-free systems for transportation. A fuel cell operating on renewably generated hydrogen (from solar, wind, biomass, etc.) is one option, and proton exchange membrane fuel cells (PEMFCs) are considered to be the best type for automobile applications due to their high power density, low operating temperature, high power-to-weight ratio and absence of corrosive fluids. They have also shown great promise for mobile applications such as portable electronics with alcohol as the fuel, such as a DMFC (direct methanol fuel cell). For operation with hydrogen as the fuel, the only chemical byproduct is water, thus the process is clean. The fuel cell is generally more efficient in its direct conversion of chemical energy to electrical energy than internal combustion and steam engines, which are restricted by Carnot cycle efficiency. The efficiency of fuel cells for generating electricity is 40 % – 60 % and can reach 85 % – 90 % in combined heat and power (CHP) mode, i.e. if the heat generated from the cell reaction is also used. Fuel cells can be used on a micro/local level without loss of efficiency, thereby avoiding transmission losses associated with long distance power lines. For the hydrogen PEMFC, two major electrochemical reactions occur simultaneously at the two electrodes as shown in Figure 1.1: hydrogen is oxidized at anode to release protons and electrons; these protons transport through membrane electrolyte and electrons are conducted through an external circuit to the cathode to react with oxygen molecule, where water is formed. Therefore, the only chemical product

during the whole process is water, showing great potential of reducing the problems associated with carbon-based energy production and mitigating the environmental pollution.

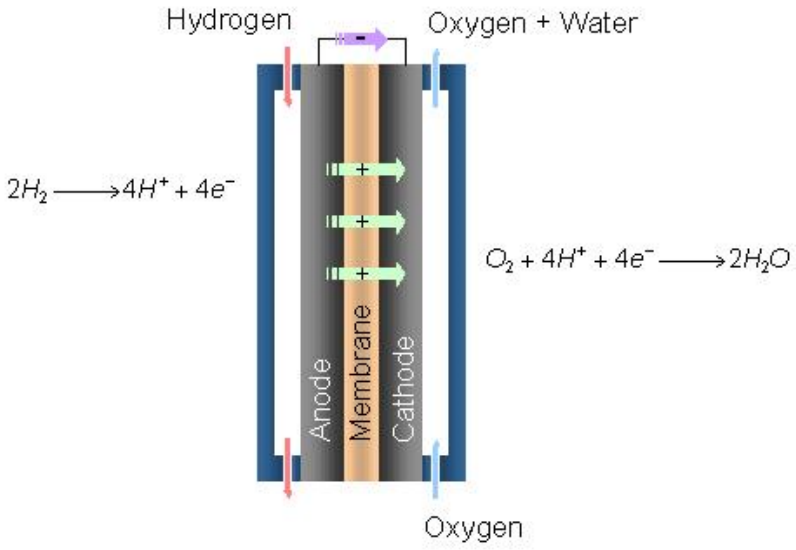

Figure 1.1. A fuel-cell cross section.

The electrodes are often made from highly dispersed platinum (3-5 nm) or its alloy supported on high surface area carbons with electrolyte ionomer as a binder that creates a porous structure. The electrocatalysts are typically 20 - 40 wt% with loadings in the range 0.1 - 0.5 mg cm^{-2}. This structure greatly facilitates gas transport, proton conduction and surface reaction kinetics. Generally, the loading and type of catalyst at both anode and cathode can be the same; however, the activity of platinum may be severely decreased by small amount (> 10 ppm) of carbon monoxide (CO) in the reactant gas. This is of particular concern for systems using reformate (hydrogen produced from

natural gas or other hydrocarbon fuels). For this reason the anode electrocatalyst is often a PtRu alloy, which is more resistant to CO poisoning and generates less H_2O_2 while bleeding O_2 to mitigate CO poisoning [1].

The reactant gas is fed to each electrode through a gas diffusion layer (GDL), which is typically made from carbon cloth or carbon paper. The dual function of the GDL is (a) to allow reactant gas to diffuse uniformly to the electrocatalyst layers under the ribs of the flow fields and (b) to collect current from reaction sites. In addition, a hydrophobic phase (usually PTFE) is often coated on the GDL to avoid flooding. The ideal GDL material must have high porosity, low electrical resistance, good chemical stability and low cost.

The electrolyte in a PEMFC is a proton exchange membrane; typically a film made from an inert polymer framework containing a proton-conducting structure that is usually consists of pendant acid endgroup on the side chain. This membrane is positioned between two electrodes, which are in turn sandwiched between two porous gas diffusion layers. The whole construction forms a membrane electrode assembly as shown in Figure 1.2. The MEAs are electrically connected in series by alternately stacking with conductive bipolar plates to form fuel cell stack. These bipolar plates have gas flow fields and are usually made from graphite or stainless steel. The basic requirements for the membrane include high electrical conductivity to minimize cell resistance and maximize efficiency. Moreover, these membranes act as gas barrier to separate reactant gases, so they must possess good mechanical properties, be uniform and flexible, free of defects, as well as low gas permeability. In addition, since the membrane is subjected to a strong oxidative environment with the existence of O_2, H_2O_2 and even free radicals, the

membrane should also have excellent chemical stability towards hydrolysis, oxidation and reduction to various chemicals and maintain this property during its lifetime. So in general, the merits of fuel cell membrane we desire for can be summarized as follows:

- High proton conductivity
- Low electronic conductivity
- Low gas permeability
- Excellent chemical stability
- Good mechanical properties
- Low cost

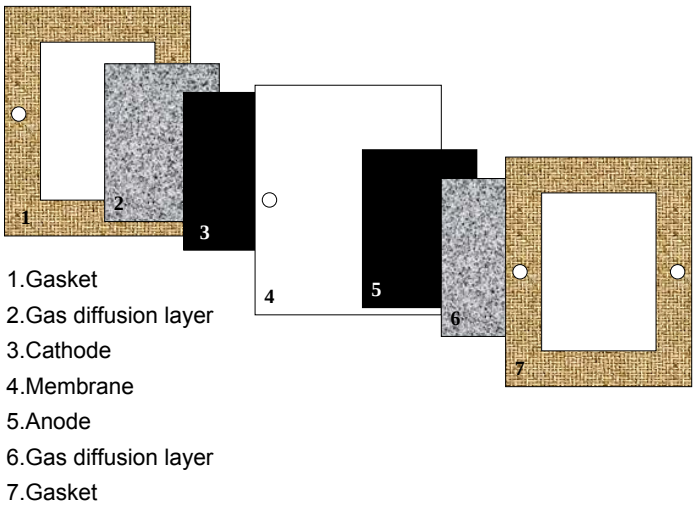

Figure 1.2. Schematic representation of an MEA.

Typically, the membranes for PEMFC are made of perfluorosulfonic acid (PFSA) ionomer, such as DuPont's Nafion®, Asahi Glass's Flemion®, Solvay Solexis's Hyflon®

[2] and other ionomers developed by 3M and Dow Chemical [3]. These membranes are generated by copolymerization of a perfluorinated vinyl ether comonomer with tetrafluoroethylene (TFE) [4], resulting in the chemical structure given below:

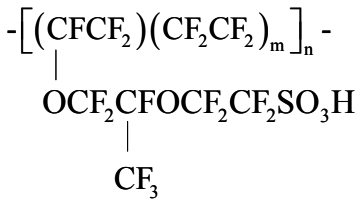

Figure 1.3. Nafion® chemical structure.

The other types of membrane materials being developed can be classified into three categories: (1) modified PFSA membranes by incorporating hydroscopic oxides and solid inorganic proton conductors such as SiO_2 [5] and carbon nanotube [6]; (2) sulfonated polyaromatic polymers and composite membranes, such as SPEEK [7]; (3) acid–base polymer membranes, such as phosphoric acid-doped PBI [8].

Although progress has been made in developing these alternative membrane materials, the current state-of-the-art proton exchange membrane is still Nafion®, which was developed by E. I. Dupont Company in mid-1960s [9]. Owing to its chemical stability, permselectivity and high proton conductivity, Nafion® PFSA polymer has been used in a broad range of applications [10-12]. After the development of Nafion® membrane, the first Nafion-based PEMFC was tested in 1966; however, by the early-1980s, membrane electrolysis production of chlorine and sodium hydroxide from sodium chloride emerged as the largest application for Nafion® membranes. Nowadays, Nafion® membranes are widely used in many applications including fuel cells, electrochemical

devices, production of high purity oxygen and hydrogen, recovery of precious metals, gas drying or humidification, water electrolysis, plating, surface treatment of metals, batteries, sensors, Donnan dialysis cells, drug release, and super-acid catalysis for organic reactions. However, there are still a lot of challenges in the application of Nafion® as a proton exchange membrane in fuel cells.

The first and most frequently identified challenge is the membrane cost. The price of PFSA membrane is very high (~$5000/kg) compared with the commodity PTFE (polytetrafluoroethylene) membrane (~$10/kg). And the cost of Nafion® membrane is about $50 ~ 100/kW for a typical hydrogen PEM fuel-cell system, whereas the target is $3/kW. This represents about 3% of the system cost [13]. However, the price is expecting to drop significantly with mass production. The price projections were studied by Mathias *et al.* [14] and are shown in Figure 1.4 and indicate that at 1 million vehicles/yr, which would require approximately 1,000 MT/yr of PFSA, the membrane cost would drop to less than $100/kg. This translates to approximately $1/kW. Whereas there are reasons why alternatives to PFSA membranes are of interest, the high price of PFSA membrane is at best a secondary one.

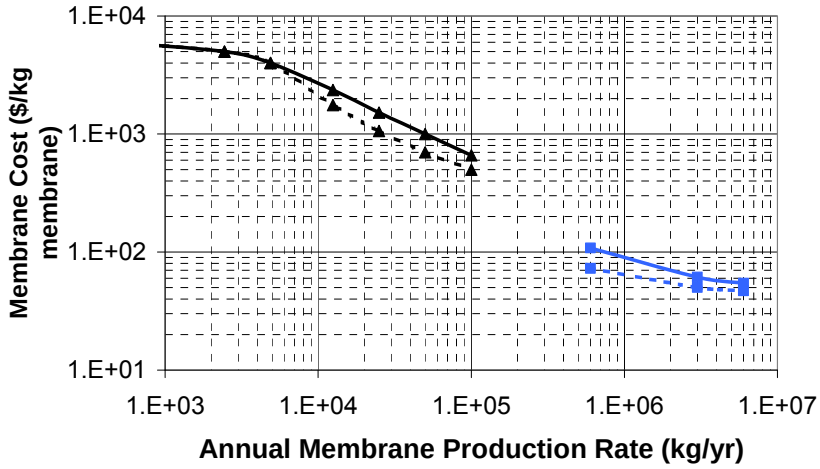

Figure 1.4. Price projection of PFSA membrane (25 micron, 0.05 kg/m^2, 1100 EW) at high volume [14].

The second challenge is the membrane performance. The conductivity of Nafion® is strongly dependent on the level of hydration [15]. The water content in Nafion® drops dramatically under conditions of high temperature and low humidity. In a fuel-cell system, the reactants therefore have to be humidified in order to prevent membrane dry out, despite the generation of large quantities of product water at the cathode. When proton exchange membranes are subjected to temperatures above 100 ^{o}C at atmospheric pressure, their conductivity decreases significantly due to dehydration. Somewhat higher temperatures can be reached when reactant pressures exceeding the water vapor pressure are employed. Clearly, pressurizing reactants to more than 1 to 2 bar above ambient is not desirable in fuel-cell systems due to the high parasitic power requirement for compressors. This, in addition to thermal stability issues, makes this proton conducting material unsuitable for elevated temperatures (120 – 200 ^{o}C). Recently, much work has focused on the development of alternative high-temperature membranes to Nafion® that

would have good conductivity and membrane performance with very low humidification requirement.

The final and most important challenge is the membrane durability, which is also the topic of this dissertation. Although Nafion® perfluorosulfonic acid (PFSA) polymer has demonstrated highly efficient and stable performance in fuel-cell applications, evidence of polymer degradation is found after a few hundred to a few thousand hours depending on operating conditions [4, 16, 17]. The membrane becomes thinner, some pinholes are developed in it, and fluoride ions are detected in the waste water. These defects result in high rates of hydrogen crossover, which in turn causes rapid performance decay, even catastrophic failure of the cell in the worst case. Therefore, an important issue to achieving the lifetime target of fuel cells will be the stability and durability of membrane, which strongly affects cell performance and the membrane system price during operation. In order to meet requirements for automotive applications, membrane electrode assemblies used in proton exchange membrane fuel cells will be required to demonstrate durability of about 5,000 hours under normal operating conditions [16].

Although qualitative information is emerging, scant fundamental understanding of the mechanisms has been elucidated. This dissertation seeks to address the needs for greater understanding of membrane degradation mechanisms and phenomena in PEMFCs. So the objectives of my project are:

1) to understand the role of humidity, temperature, partial pressure and level of metal contaminants in the degradation mechanism,
2) to develop spectroscopic techniques to detect chemical changes in the membrane,

3) to provide experimental data and support the development of macroscopic degradation model.

CHAPTER 2

BACKGROUND AND PRIOR WORK

2.1 Challenges in PEMFCs

The PEMFC is working under harsh conditions, such as low pH, high potential (cathode), and exposure to strong oxidants, oxygen and H_2O_2 intermediates for example. The durability difficulties of PEMFC becomes especially severe under low humidity and high temperature, which are the desired operation conditions for PEMFC [17]. Unfortunately, as the temperature increases and the humidity decreases, the major material durability challenges, which include Pt dissolution [18], carbon corrosion [19] and membrane degradation, will be significantly pronounced.

2.1.1 Pt dissolution

Pt and its alloys are the most common and effective catalyst for the oxygen reduction reaction (ORR) in PEMFC. However, the small solubility of Pt in acid electrolyte leads to Pt dissolution. Specifically, this process is accelerated under potential cycling and high temperature conditions [20].

2.1.2 Carbon corrosion

Since the electrochemical oxidation of carbon has relatively low standard potential (0.203 V), carbon supports suffer electrochemical corrosion under fuel-cell conditions especially during start-up and shutdown procedure and hydrogen starvation [19, 21]. The above two degradation processes are principally driven by electron transfer

reactions, and therefore the rates are highly dependent on the electrochemical potential, In contrast, membrane degradation, the topic of this dissertation, is due to chemical attack and mechanical stress.

2.1.3 Membrane degradation

Membrane degradation has been observed from the initial development of PEM fuel-cell technology by General Electric in the 1960s for use by NASA on their first manned space missions. The electrolyte membrane was poly (styrene sulfonic acid) polymer that proved unstable due to degradation problems, prompting NASA to switch to alkaline fuel cell technology for subsequent missions. Later, the advent of Nafion®, a PFSA membrane gave a boost to the PEM industry and gave rise to a membrane with improved performance and lifetime. In the late 1980s Ballard Power Systems (Vancouver) and Los Alamos National Labs (California) began developing PEM fuel cells with a Nafion® membrane, which is more stable than the hydrocarbon membrane. However, in recent years, it has been established that the degradation of the MEA (membrane electrode assembly) occurred with the coexistence of H_2, O_2 and Pt catalyst and are highly dependent on the operation conditions of the fuel cell [22]. The failure mechanisms of PFSA membranes can be classified as mechanical (pinhole and crack formation), thermal (dryout, solvolysis, and desulfonation), and chemical (peroxide initiated free radical degradation) degradations [23]. Mechanical and thermal degradation can be minimized by proper choice of materials, careful fuel-cell fabrication, and by maintaining reasonable operating temperatures and humidities. However, chemical degradation of the membrane can be difficult to mitigate. One reason for this difficulty is

the generation of hydrogen peroxide via surface reaction between chemi-adsorbed H atom and O_2 molecule or two-electron oxygen reduction reaction [24]. It was also reported that degradation of Nafion® produces F^-, SO_4^{2-}, CO_2, SO_2 and some fluorocarbons [25]. The loss of these small molecules from polymer would cause both physical and chemical change in the membrane. Changes in the chemical structure, such as bond cleavage and formation of new moieties, are more important because of the effect on the physical properties of these membranes could further exacerbate the mechanical and thermal degradation and cause the failure of the whole fuel-cell system [26].

2.2 Background of membrane degradation mechanism

Membrane degradation in fuel-cell is a complicated process especially for PFSA membranes. Although much work has been conducted in this area, the detailed mechanism is still under debate. Generally, three pathways for membrane degradation have been proposed. In the first, H_2O_2 is formed by a reaction between oxygen and hydrogen. The peroxide then decomposes giving ·OH or ·OOH radicals that attack the H-containing terminal bonds, such as carboxylic groups [4, 27], and this initiates chemical decomposition. However, the difficulty is that the H-containing terminal bonds exist in small quantities and can't account for the large fluorine loss observed over fuel-cell lifetimes. Recent research showed that even chemically modified Nafion® membrane, where the carboxylic acid content has been eliminated, still undergo chemical attack; although the rate of fluoride ion emission has been reduced [28]. Therefore, the research has focused on the stability of sulfonic acid groups instead of carboxylic acid groups

[29]. A second proposed mechanism begins with H_2O_2 formation and radical attack steps as described above. Hydrogenation of the main chain to generate C-H bonds [30, 31], which are more susceptible to chemical attack, is the next step in the decomposition pathway proposed. However, no direct observations by spectroscopic methods of C-H bonds in the membrane have been made, and no detailed mechanism of further radical attack was provided. Finally, a third alternative mechanism of membrane degradation that does not involve H_2O_2 [32, 33] has been argued. It is suggested that some reactive species other than H_2O_2, such as OH free radical, is directly formed on the surface of the Pt catalyst via the reaction between H_2 and O_2 and subsequently attacks the membrane. However, the details of reactive species are still unclear, and the study of OH free radical formation on Pt catalyst is limited to molecular simulation.

It is possible that multiple degradation mechanisms coexist. The experimental evidence [34] best supports the mechanism involving H_2O_2 formation and subsequent radical attack, although the attacking site on Nafion® polymer chain is still unclear [35]. More recently, formation of hydrogen peroxide has been detected in an operating fuel cell; the rate of peroxide formation was strongly influenced by the thickness of the membrane, suggesting that transport of oxygen and hydrogen in the membrane may limit the formation of peroxide [36]. Therefore, this chemical attack is believed to be due to formation of peroxide caused by the diffusion of oxygen across the membrane where it reacts with hydrogen at the anode. In other words, the rate of chemical degradation of the membrane will depend on the rate of gas crossover.

Although the existence of hydrogen peroxide has been confirmed during fuel-cell operation [36, 37], the formation mechanism is still ambiguous due to the poor

understanding of surface reactions on Pt catalyst. At the anode, a possible H_2O_2 formation mechanism was described by LaConti *et al*. [23] based on the reaction between chemi-sorbed atomic hydrogen and an oxygen molecule that diffuses from the cathode:

$$H_2 \rightarrow 2H\cdot \text{(on Pt or Pt/Ru catalyst)} \qquad \text{(Reaction 2.1)}$$

$$H\cdot + O_2 \rightarrow HO_2\cdot \text{(O_2 diffused through PEM)} \qquad \text{(Reaction 2.2)}$$

$$HO_2\cdot + H^+ + e^- \rightarrow H_2O_2 \qquad \text{(Reaction 2.3)}$$

At cathode, two-electron ORR occurs when potential is below 0.695 V. Since two-electron ORR rate is inherently faster than peroxide reduction reaction rate, one expects to observe peroxide formation in the cathodic consumption of oxygen.

$$O_2 + 2H^+ + 4e^- \rightarrow 2H_2O(1.229V) \qquad \text{(Reaction 2.4)}$$

$$O_2 + 2H^+ + 2e^- \rightarrow H_2O_2(0.695V) \qquad \text{(Reaction 2.5)}$$

$$H_2O_2 + 2H^+ + 2e^- \rightarrow 2H_2O(1.763V) \qquad \text{(Reaction 2.6)}$$

It is thought that the radicals generated from the catalytic decomposition of peroxide attack polymer end groups having H-containing terminal bonds (such as -CF_2COOH) that are formed during membrane processing [4]. One common example of radical generation from hydrogen peroxide decomposition is in the Fenton's test, where peroxyl or hydroxyl radicals can be formed through the reaction of hydrogen peroxide with ferrous ion:

$$Fe^{2+} + H_2O_2 \rightarrow Fe^{3+} + OH^- + \cdot OH \qquad \text{(Reaction 2.7)}$$

$$H^+ + OH^- \rightarrow H_2O \qquad \text{(Reaction 2.8)}$$

The mechanism of attack on the endgroup CF_2-COOH includes the following reactions [4] abstraction of hydrogen from an acid endgroup to give a perfluorocarbon

radical, carbon dioxide and water (step 1); the perfluorocarbon radical can react with hydroxyl radical to form an intermediate that rearranges to an acid fluoride and one equivalent of hydrogen fluoride (step 2); hydrolysis of the acid fluoride generates a second equivalent of HF and another acid endgroup (step 3).

$$Rf - CF_2COOH + \cdot OH \rightarrow Rf - CF_2 \cdot + CO_2 + H_2O \qquad \text{(Reaction 2.9)}$$

$$Rf - CF_2 \cdot + \cdot OH \rightarrow Rf - CF_2OH \rightarrow Rf - COF + HF \qquad \text{(Reaction 2.10)}$$

$$Rf - COF + H_2O \rightarrow Rf - COOH + HF \qquad \text{(Reaction 2.11)}$$

In the above scheme, one product of the reaction is HF. The rate of membrane degradation, during fuel-cell operation, can be determined by measuring the fluoride ion emission rate (FER) from the fuel-cell exhaust water. Membrane degradation rate is affected by many factors, such as relative humidity, temperature and mechanical stress. Worthy of note, degradation may be localized and the membrane may fail before significant polymer degradation occurs.

2.2.1 Membrane degradation study by *ex-situ* durability tests

Due to the number and complexity of the factors that influence degradation during fuel-cell operation, various *ex-situ* tests were designed to study membrane durability. These save time and are well-controlled; more important, it is easy to obtain an undamaged sample without the interference from the Pt catalyst layer for subsequent analysis. Qiao *et al.* [38] studied degradation of perfluorinated ionomer membranes during treatment in H_2O_2 solution by FTIR and Thermogravimetric Analysis (TGA). The IR spectra provided clear evidence of S-O-S formation for membrane subjected to H_2O_2. The authors further suggested that cross-linking between two side groups in the cluster

resulted in breakdown of hydrogen bonding in the water and the destruction of ion clusters and therefore, the degradation of proton conductivity.

The most important and widely used *ex-situ* durability test is the so-called Fenton's test. It provides a well-known source of hydroxyl radicals, and some similarities between the *in-situ* (fuel-cell operation) and *ex-situ* (Fenton's test) degradation mechanism have been reported [39]. Kinumoto *et al.* [27] studied the effect of different metal ions in Fenton's reaction including alkali and alkaline transition metal ions and found that the presence of Fe^{2+} and Cu^{2+} greatly enhanced the decomposition rate of Nafion® membrane. Further FT-IR and ^{19}F NMR measurements of deteriorated membrane revealed that both the main and side chains are decomposed at similar rates by radical attack, most probably because the decomposition proceeds through a radical.

Kundu *et al.* [40] compared two types of Fenton's tests: the solution method and the exchange method. FTIR, IEC (ion exchange capacity), and EDS analysis showed no change in Nafion® chemical structure. Analysis of the cross-sections of degraded membrane by the solution method revealed that the bubbles originated at the center of the membrane, splitting it into two. Membranes degraded by the exchange method did not split into two, but instead areas close to the surface appeared 'foamy'. Rhoades *et al.* [41] used broadband dielectric spectroscopy to analyze polymer chain motions after Fenton's test. They found the β-relaxation peak maximum (f_{max}) was seen to shift to lower values with degradation, reflecting slower chain motions. This may be caused by the loss of soluble short chain fractions in the molecular weight distribution, thereby increasing the average molecular weight.

The experimental procedure of Fenton's test was also improved to simulate better the fuel-cell environment. Delaney and Liu [42] developed a vapor phase Fenton's test using a test chamber and applied FTIR to measure the formation of –COOH groups in the membrane. They suggested that the vapor phase test is more similar to OCV and low power conditions in fuel cell, whereas the liquid phase test corresponds to high current operation.

Nonetheless, the difference between the *ex-situ* Fenton's test and *in-situ* fuel-cell tests may limit the applicability of these results [35] because the performance of a membrane in such a test is not necessarily a good prediction of its durability under fuel-cell conditions. Recently developed non-fluorinated membranes such as 4,4'-biphenol based poly(arylene ether sulfone) copolymers [43] have been reported to degrade extensively in Fenton's test but demonstrate longer lifetimes than do Nafion® membranes in open circuit voltage tests due to low O_2 permeability in the non-fluorinated membranes.

Therefore, a new method to evaluate the decomposition rate of polymer electrolyte caused by crossover was developed [44], where the gas composition, its humidity, and the temperature were controlled individually. It was found that PFSA ionomer coated on Pt/C catalysts decomposed faster at high humidity. Pt particles in the electrolyte were found to suppress its decomposition by scavenging H_2O_2 and/or OH radicals.

2.2.2 Membrane degradation study by *in-situ* fuel-cell tests

Durability of membrane was normally tested by an accelerated fuel-cell test under high temperature, low humidity and current densities, especially open-circuit voltage

(OCV) conditions. Endoh *et al.* studied PFSA membrane degradation under low humidity conditions and observed faster potential decay and increased hydrogen crossover compared to normal conditions. They found the formation of carbon radicals in the catalyst layers of degraded MEA by Electron Spin Resonance, which were presumably generated by a reaction of the carbon black and either the hydroxyl radical or hydroperoxyl radical or both.

Inaba *et al.* [45] measured rates of hydrogen crossover and fluoride ion emissions during an OCV test and observed an increase of hydrogen crossover after 30 days. They also studied the effect of gas humidification on membrane degradation and found FERs increased with the decrease of humidity. They attributed gas crossover and catalytic combustion at the electrodes as the key factors for membrane degradation. The impact of gas partial pressure on membrane degradation was investigated by Liu *et al.* [46]. They found a strong dependency of FERs on H_2 partial pressure in the range from 20 - 200 kPa. On the contrary, there is no significant difference in FER when O_2 partial pressure increases from 40 - 200 kPa whereas a linear relationship between FER and O_2 partial pressure is observed from 2 - 20kPa.

More detailed membrane degradation studies were performed by Mittal *et al.* using different cell configurations (anode only, cathode only and bilayer membrane modes) [47]. They were able to detect H_2O_2 in the effluent water when there was an electrode only on one side of the membrane. The FER from a cell under load was dependent on the H_2 crossover rate through the membrane. They suggested the possibility of an alternate membrane degradation mechanism other than H_2O_2 formation. In a further study, they found that pre-exposure of catalyst to O_2 significantly affected the membrane

degradation rate [16], but the carbon support does not have a strong impact on degradation. The effect of current densities was also studied, and a decrease in FER was observed with an increase in the current density. Finally they concluded that the degradation mechanism is most likely initiated by the species formed as a result of the H_2 and O_2 reaction on the catalyst.

The choice of a cathode alloy catalyst was found to impact membrane life as well. Sulek *et al.* [48] found base metal cations, such as Ni^{2+}, are more benign than Fe^{2+} to the Nafion® membrane. PtNi/C and heat-treated Pt/C could extend membrane lifetime by about 60 % because the amount of Pt leached from the catalyst was reduced. They hypothesized that the membrane life extension may depend on a lowered amount of leached Pt when the alloyed cations are benign. This result suggests that the Pt particle diffused from cathode side into the membrane may influence membrane degradation. In fact, some researchers have already investigated the impact of Pt dissolution on membrane degradation specifically the formation of a Pt band. However, whether a Pt band could accelerate membrane degradation is still under debate. Endoh *et al.* [49] used an infrared imaging method and EPMA analysis and found that the chemically degraded portion of the membrane did not correlate with the Pt band position. Further OCV tests confirmed that Pt with a clean surface did not decompose the PFSA polymer. They concluded that Pt particles deposited in the membrane will not contribute to the degradation of the membrane. In contrast, Ohma *et al.* [50] found that the membrane around the Pt band was markedly degraded using micro-Raman spectroscopy and the magnitude of the FER was consistent with the location of Pt band. They argued that the

Pt band formed in the membrane during the OCV hold duration is one of the factors accelerating membrane degradation.

2.2.3 Radical type and its attacking site

Electron Spin Resonance (ESR) is a spectrometric method that is well-known technique for the study of free radicals. ·OOH and superoxide radicals O_2^- were detected in Nafion® exposed to the Fenton's reagent based on Ti^{3+} by Bosnjakovic and Schlick [51]. O_2^- radical were observed only in dry Nafion®, which were stable for about 14 days. That would explain the stability of radicals during chemical attack. *In-situ* ESR has also been developed to observe the free radicals during fuel cell operation [52-54]. Panchenko and his coworkers found that direct ESR investigation in a running fuel cell provides evidence for unspecified radical centers at the cathode side of the membrane.

Cipollini [35] compared rate constants in Fenton's reaction and concluded that both hydroxyl and peroxyl radicals are involved in membrane degradation. He also found that both ends and side chains are attacked by hydroxyl leading to rapid, local material loss. His supposition is that the C-S bond in Nafion® membrane is slowly hydrolyzed to remove the sulfonate group and convert the adjacent $–CF_2$ to a –COOH, which could serve as another endgroup decomposition center. Endoh [55] found significant decrease in FER for Na^+ exchanged PFSA membrane. He hypothesized that OH radical can attack sulfonic acid groups, and the formation of $–CF_2SO_3·$ radical will lead to side chain degradation.

Coms [56] performed a comprehensive thermochemical analysis of PFSA ionomers and the reactive oxygen species formed in fuel cell and revealed that hydroxyl

radical is the only oxidant capable of abstracting a hydrogen atom from a carboxylic acid intermediate. Accordingly, two chemically specific, and thermochemically sound, main chain scission mechanisms are proposed. The first involves formation of a sulfonyl radical under dry membrane conditions. The second involves hydrogen atoms formed from reaction between hydrogen gas and hydroxyl radical.

Degradation of model compounds of PFSA membranes in Fenton's reagent was studied by Zhou *et al.* [57] and carboxyl chain ends were found to be the preferred sites of attack. Ether linkages are also viable points of attack for peroxide radicals and can lead to side chain cleavage. They concluded that the side chain ether attack can become the dominant mechanism for polymer degradation with highly modified fuel-cell membranes.

Ramaswamy *et al.* [58] employed a novel segmented fuel cell for membrane durability characterization and post analysis of the membrane indicated that cleavage of the side chain ether linkage, which intrudes into the hydrophilic ionic cluster, is the key initiator of conductivity and ion exchange capacity loss.

CHAPTER 3

EXPERIMENTAL METHODS AND ANALYTICAL TECHNIQUES

3.1 *Ex-situ* Fenton's test protocol

In order to achieve the same degradation effect in a relative shorter amount of time, Fenton's test is the most commonly employed as an *ex-situ* accelerated chemical degradation experimental method of fuel cell membranes [40]. Fenton's reagents are often made by mixing ferrous ions (from $FeSO_4$) with hydrogen peroxide to generate OH free radicals as shown in Reaction 2.7.

This primary test is accomplished by adding a sample of Nafion® membrane into prepared Fenton's reagent and is called the solution method. The procedure of this test is as follows:

Membrane Pretreatment - First the membrane was treated with a 2 % solution of hydrogen peroxide at 80 ^{o}C and rinsed in boiling de-ionized water for 0.5 hr. Then the membrane was heated in 0.5 M sulfuric acid for 0.5 hr at 80 ^{o}C to remove metallic impurities. Subsequently, the membrane was repeatedly washed with de-ionized water at the same temperature to remove the sulfuric acid and then dried in air.

Fenton's test by solution method - The membrane was weighed and placed in a wide mouth bottle. Hydrogen peroxide solution was heated on a hot plate to the desired reaction temperature (normally a little lower since temperature will increase quickly after adding salts). Then ferrous ions were added into the solution and subsequently the pretreated Nafion® membrane sample was immersed into the solution for several hours. After treatment, the degraded membrane was removed from solution, then repeatedly washed with de-ionized water and dried by carefully pressing between two filter papers.

FER measurement - The resulting solution was first filtered to remove the metal precipitate. Platinum mesh was used to remove the residual hydrogen peroxide which

may influence fluoride ion determination with ion chromatography. Finally the clear solution was injected into an ion chromatograph and checked for fluoride ion content.

In the alternative method, ferrous ions were exchanged with protons in the Nafion® membrane, which was then submerged into hydrogen peroxide solution and allowed to degrade. Therefore, the first and final steps are the same, and only second step is different:

Fenton's test by exchange method - Ferrous ion solution was prepared by adding a known amount of ferrous sulfate into de-ionized water. At room temperature, Nafion® was soaked in the ferrous sulfate solution for a day to complete ion exchange process. The ion-exchanged Nafion® membrane was then washed with de-ionized water repeatedly to remove residual solution on the surface. At the same time, hydrogen peroxide solution was heated on a hot plate to the desired reaction temperature. The ion-exchanged Nafion® membrane sample was quickly immersed into the solution to react with hydrogen peroxide. After treatment, the degraded membrane was removed from solution, then repeatedly washed with de-ionized water and dried by carefully pressing between two filter papers.

3.2 *In-situ* accelerated membrane degradation test protocol

3.2.1 MEA Fabrication

The detailed procedure is described in Appendix D. Briefly, the Pt/C catalyst system is mixed with IPA, de-ionized water and Nafion® ionomer solution so as to maintain an ionomer to carbon ratio of 0.8 ~ 1.0 : 1 by mass. The mixture is ultrasonicated for 5-10 minutes before airbrushing onto Teflon™ decals. These decals are laid on a hot plate to promote drying between coating passes. The finished decals are transferred to Nafion® 112 membrane, by hot pressing at 140 ~ 160 °C and 1700 kPa.

3.2.2 Cell Assembly

5 × 5 cm membrane electrode assemblies were purchased from Fuelcellstore.com or fabricated by in house. The MEA included Nafion® 112 membrane and Pt/C catalyst layers with Pt loadings of 0.3 mg/cm^2 in both anode and cathode. The MEA and gas diffusion layers (GDLs) were carefully assembled together in the 25 cm^2 fuel-cell testing hardware (Fuel Cell Technologies, Inc.) with Teflon™ coated fiberglass gasket (from the Saint-Gobain Performance Plastics) around MEA for sealing purposes. The hardware is equipped with serpentine flow patterns machined into two graphite plates. All bolts were torqued to a constant value to ensure a uniform compressive load was applied over the entire MEA for all durability tests.

3.2.3 Accelerated Durability Test Procedure

Long-term fuel-cell durability tests were conducted on the Fuel Cell Test Station (Scribner Associates Model 890CL) after connecting the fuel-cell testing hardware to this system. Mass flow controllers were used to meter the gas flow rates. During the experiments, the cell and saturator temperatures were varied to achieve the control of fuel-cell humidity and temperature. Water from anode and cathode vents was collected in polypropylene bottles for analysis. All water samples collected were then analyzed by ICS-2000 Ion Chromatography System from Dionex Corporation. The fluoride ion emission rate (FER) under a particular operational condition and time was calculated from the volume and fluoride ion concentration of water. FER is considered to be an indicator of the rate of membrane degradation. The sulfate ion (SER) and trifluoroacetic acid (TER) emission rates were similarly calculated from the concentration of SO_4^{2-} and TFA in the exhaust water.

3.2.4 Membrane Sample Preparation

After the accelerated test, the fuel-cell hardware was disassembled, and the GDL and catalyst layers from the anode and cathode were removed to leave the membrane

separator for analysis. Normally a small amount of catalyst remained on the membrane surface. The membrane was subsequently immersed in dilute isopropyl alcohol (concentration ~ 1 %) to remove this residual Pt catalysts and carbon black. Sometimes a sharp knife was used to carefully peel off the soaked catalyst. After the catalyst was completely removed, the membrane was thoroughly washed in de-ionized water and dried in vacuum at 50 ^{o}C for 24 hrs before further measurement.

3.3 Analytical Techniques

3.3.1 Polarization Curve

A polarization curve, which is the potential/current density relationship, was used to evaluate the performance of fuel cell especially the change of membrane resistance in degradation studies. Data were measured in a constant current (galvanostatic) mode. The cell temperature was 65 ºC, and fuel and oxidant gases were fully humidified. Hydrogen and air flow rates were 0.95 dm^3/min and 3.64 dm^3/min, respectively. A fuel-cell polarization curve is obtained from the following procedure.

(a) First operate the cell without load but supplying gases (N_2 flushing) for 15 minutes. Then switch from nitrogen to the fuel on the anode followed by oxidant gas flows to the cathode, apply a load (200 mA/cm^2) and run the cell for 15 minutes.

(b) Disconnect the load but leave the flow of gases unaltered, wait 15 minutes for the system to stabilize. The average cell potential is recorded as the Open Circuit Voltage during the last 5 minutes testing.

(c) Then increase the current density, measure the cell potentials (and iR drop potentials) typically at 20, 30, 50, 100, 200, 500, 800, 1000 (mA/cm^2) values of current density. Normally, the test is stopped when the potential falls below 0.3 V. Similarly, report the average cell potential in the last 5 minutes during each 15 minutes testing.

3.3.2 Hydrogen Crossover Measurement

The rate of hydrogen crossover was determined by measuring a limiting current. During the test, hydrogen and nitrogen flowed at the anode and the cathode, respectively. Using a potentiostat, the potential of the cathode (working electrode) was slowly scanned from OCV (around 0.1 V vs. RHE) to 0.4 V (vs. RHE) and held at 0.4 V (vs. RHE) to measure the pseudo-steady limiting oxidation current (mA/cm^2), which was used to calculate the rate of H_2 crossover ($mol/cm^2/h$). The gas flow rates were 0.38 dm^3/min for hydrogen and 0.91 dm^3/min for nitrogen.

3.3.3 Ion Chromatography

Fluoride ion concentration in the exhaust water was measured by ICS-2000 Ion Chromatography System from Dionex Corporation. The ICS-2000 is available with a dual piston pump, LCD touch-pad front panel, Reagent-Free eluent generation, thermally controlled conductivity cell, column heater, and optional vacuum degas. When coupled with AutoSuppression, the ICS-2000 system provides high performance with unequalled ease of use. Automation provides full control and digital data collection from a PC using a USB, high-speed communication protocol. The fluoride ion peak at approximately 3.1 minutes is the first anion to elute and was quantified using a calibration curve generated with fluoride standards (Ricca Chemical) as shown in Figure 3.1. The retention time of sulfate ion for this ion chromatography system is 6.8 minutes, which was also calibrated by sulfate standards (Ricca Chemical).

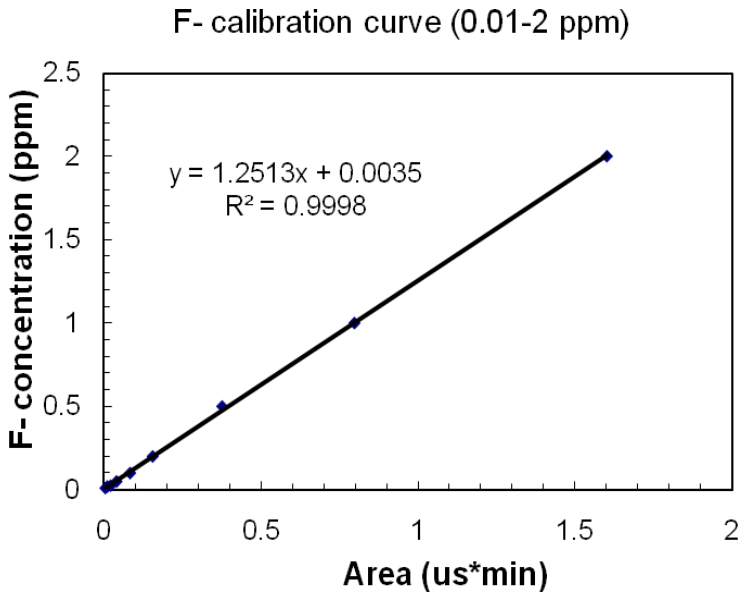

Figure 3.1. Fluoride ion concentration calibation curve.

3.3.4 Ion Exchange Capacity

All membrane samples were stabilized in 0.5 M sulfuric acid for 1 hr at 80 ^{o}C to remove metallic impurities. Subsequently, the samples were rinsed in de-ionized water for 0.5 hr to remove any residual sulfuric acid. The samples are then soaked for 24 hrs in a 1 M NaCl solution to ion-exchange H^+ with Na^+. To remove the excess NaCl, the membranes were repeatedly washed with de-ionized water for 0.5 hr and then dried under vacuum at room temperature for 24 hrs before being weighed. The Na^+ was ion-exchanged with H^+ by immersion in a 0.1 M sulfuric acid solution for 24 hrs. The sodium ion concentration in the latter solution was determined by Inductively Coupled Plasma Emission Spectrometer.

3.3.5 Conductivity and Mechanical Properties

The conductivity of membrane samples were measured by immersing in de-ionized water under room temperature using a high-throughput conductivity instrument developed by Meredith *et al.* [59] The mechanical properties of degraded membrane samples were evaluated using high-throughput mechanical characterization (HTMECH) system [60] as shown in Figure 3.2. All mechanical tests were performed under ambient conditions.

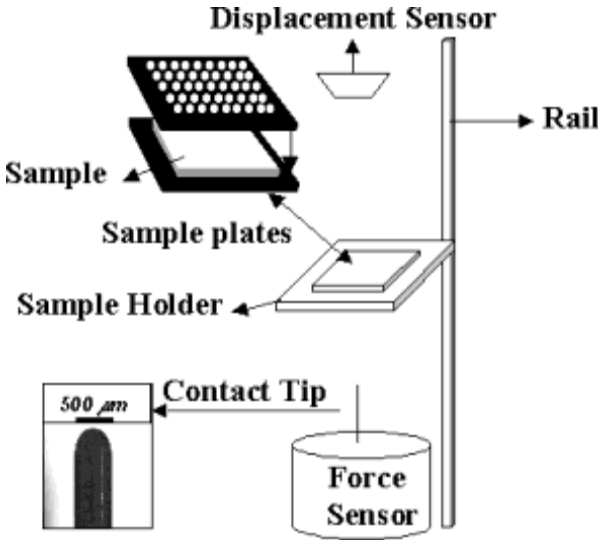

Figure 3.2. Schematic representation of the HTMECH apparatus [60].

3.3.6 X-ray Photoelectron Spectroscopy (XPS)

XPS, also known as ESCA (Electron Spectroscopy for Chemical Analysis), was used to analyze membranes samples. The spectra were collected using a Physical Electronics (PHI) Model 1600 XPS system equipped with a monochromator and an Al Kα source (hν = 1486.8 eV) operating at 350 W beam power. Ejected photoelectrons were detected by a hemispherical analyzer that provided both high sensitivity and

resolution. The operating pressure in the sampling chamber was below 5×10^{-9} Torr. Samples were aligned in the beam by maximizing photoelectron counts corresponding to the primary C1s peak in C-C bonds located at a binding energy of 284.8 eV. A neutralizer beam was used during XPS measurements to compensate for peak shifting that occurs due to charging of samples during X-ray exposure. All high resolution spectra were collected using a pass energy of 46.95 eV. The step size and time per step were chosen to be 0.025 eV and 100 ms, respectively. Atomic concentrations of different elements were calculated based on the photoelectron intensities of each element and the elemental sensitivity factors provided by the PHI. Samples were scanned at different locations and the peak intensity and composition at different locations were compared to assure uniformity of film composition over the sample surface.

3.3.7 Fourier Transform Infrared Spectroscopy (FTIR)

The FTIR spectra were collected on a Bruker IFs66vS FTIR or a Nicolet 560 ATR-FTIR system with KBr as a beam splitter. Spectra, collected as the average of 128 scans with a resolution of 4 cm^{-1}, were recorded from 4000 to 400 cm^{-1} in transmission mode.

3.3.8 Scanning Electron Microscope (SEM)

Cross sections of degraded membrane samples were either directly cut from MEA or prepared in epoxy resin [18] and surface-coated with a uniform thin layer of gold by sputtering (International Scientific Instruments). SEM observation was conducted on a LEO 1530 thermally assisted field emission (TFE) scanning electron microscope with an acceleration voltage of 3 kV.

3.3.9 Thermogravimetric Analysis (TGA)

TGA was carried out in flowing nitrogen (60 cm^3 min^{-1}) using a TA Q50 thermal analyzer. Samples were heated from ambient temperature to 600 ^oC at a heating rate of 2 ^oC min^{-1}.

CHAPTER 4

EX-SITU MEMBRANE DEGRADATION STUDIES

Previous work has suggested that hydroxyl free radicals, generated from homolytic cleavage of H_2O_2 catalyzed by metal impurities, can attack polymer end groups having H-containing terminal bonds (such as $-CF_2COOH$) that are formed during membrane processing [4]. The formation of hydrogen peroxide is caused by diffusion of oxygen across the membrane where it reacts with hydrogen. Therefore, the rate of chemical degradation of the membrane will depend upon the rate of gas crossover. For example, H_2 and O_2 permeability across an MEA with Nafion® 111 membrane are reported to be 1.61×10^{-8} and 1.3×10^{-9} mol cm^{-2} s^{-1} respectively [18]. After achieving steady state, we can assume that O_2 and H_2 crossover will be constant under a fixed O_2 partial pressure. Normally, cell potential is not expected to change significantly, so the generation of peroxide should also be nearly constant. Under these conditions, the membrane degradation rate is determined solely by the level of metal ion contaminants such as Fe^{2+} and Cu^{2+}. Fenton's reagent is a well-known source of hydroxyl radicals, and the similarity between the *in-situ* (fuel-cell operation) and *ex-situ* (Fenton's test) degradation mechanism has been reported [39]. Moreover, since the level of metal contaminants and peroxide concentration are much easier to control with Fenton's test compared to fuel-cell durability tests, we first develop analytical tools to analyze membranes exposed to Fenton's test before considering analyses of membranes that have been exposed to fuel-cell conditions.

4.1 Effect of Fe^{2+} concentration on membrane degradation

Nafion® membrane samples were exposed to Fe^{2+} concentrations of 3, 30 and 300 ppm (corresponding to samples 3, 2 and 1 respectively) and a constant H_2O_2 concentration of 10 wt% at 80 ^oC for 24 hrs. To investigate the effect of time and solution temperature, an additional membrane sample was exposed to 30 ppm Fe^{2+} (sample 4) at 60 ^oC for 8 hrs. (Table 4.1)

Figure 4.1 shows the effect of Fe^{2+} concentration on membrane degradation. It is interesting to note that the highest Fe^{2+} concentration corresponds to lowest FER, which is consistent with the results from Kodama et al. [61] However, Schiraldi [28] has pointed out that literature reports that show surprisingly low FER under aggressive Fenton's test may be in error due to the existence of Fe^{3+} in Fenton's reagent when using commercial ion-selective electrodes. In the current study, we avoided this error by using ion chromatography to measure fluoride ion content. More likely, the decrease in FER is due to different degradation products under different Fe^{2+} concentrations. At low Fe^{2+} concentrations, the main degradation product would be fluoride ion and a very small number of polymer fragments in this mild environment. As the Fe^{2+} concentration increases, the radicals may attack less active bonds such as C-O in the polymer. For example, Healy et al. [39] found a degradation product in a Fenton's test bath water with the structure $HOOC\text{-}CF(CF_3)\text{-}O\text{-}CF_2\text{-}CF_2\text{-}SO_3H$. Therefore, polymer fragments may have been a dominant degradation product, but are not detectable by ion chromatography. Although the XPS spectra discussed below show a large loss of fluorine from the membrane after Fenton's test with the highest Fe^{2+} concentration, the low F^- emission rate cannot account for this large loss. Nevertheless, Fenton's test under aggressive

conditions may provide sufficient degradation products for further study by NMR and mass spectroscopy.

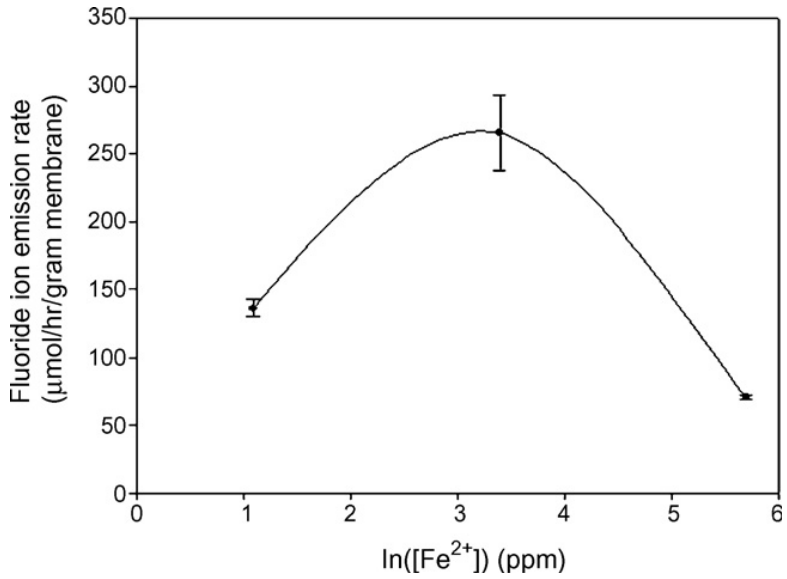

Figure 4.1. Effect of Fe^{2+} concentration on membrane degradation.

4.2 Effect of temperature on membrane degradation

Figure 4.2 shows membrane degradation rates at different temperatures for the Fenton's test. Clearly, degradation rates increase with temperature; FER increased by approximately a factor of two after a temperature increase of 10 ^{o}C. These results suggest that the lifetime of Nafion® membranes will be greatly diminished when operating above 100 ^{o}C. Therefore, identifying the membrane degradation mechanism is crucial to the improvement of membrane durability and can serve as a guide to the development of novel high temperature membranes.

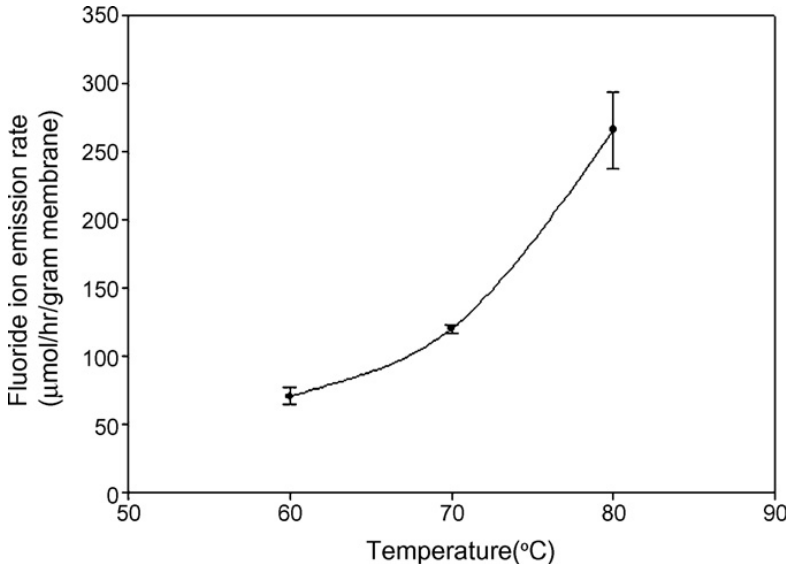

Figure 4.2. Degradation rates under different temperatures (Fe^{2+} fixed at 30 ppm).

4.3 XPS investigation on membrane degradation

4.3.1 X-ray radiation effect on membrane degradation

Pretreated Nafion® membrane samples were exposed to X-ray radiation in the XPS chamber and XPS spectra were recorded (Figure 4.3) as a function of exposure time. X-ray radiation did not cause a discernable change in the chemical structure of the membrane, even after 2 hours of exposure. Since the typical XPS analysis time for these membranes is only ~20 minutes, these results demonstrate that there is a sufficient time window to allow XPS analysis of membrane degradation resulting from electrochemical activity without introducing additional changes due to radiation exposure.

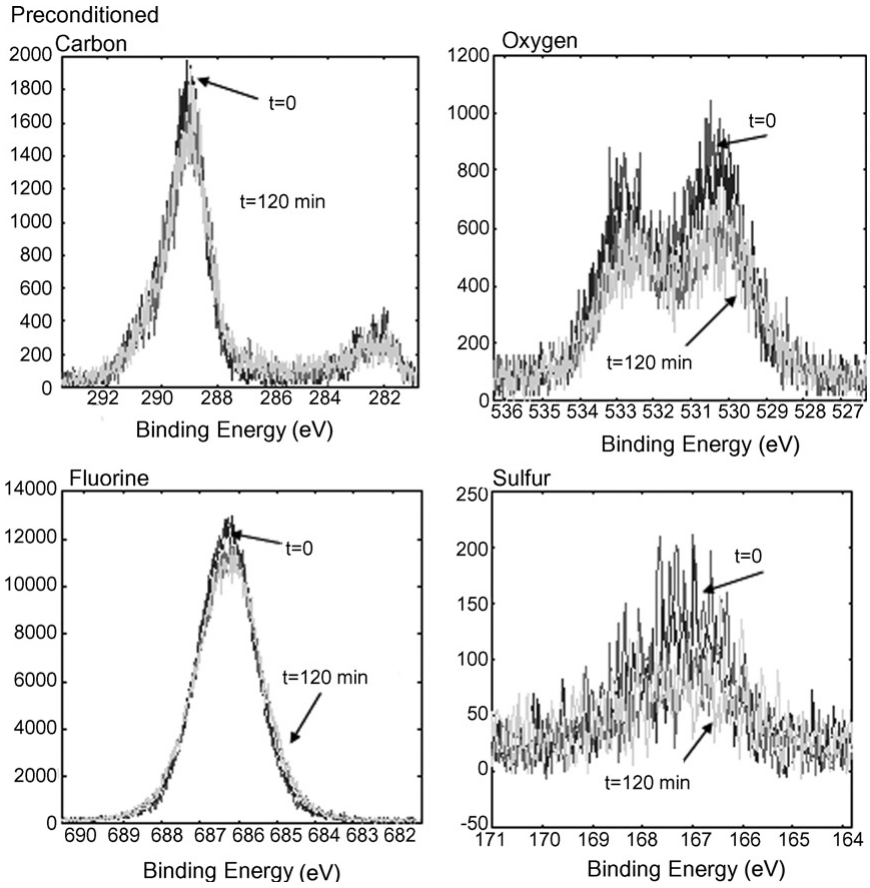

Figure 4.3. XPS spectra changes with X-ray exposure time.

4.3.2 XPS analyses of the membranes

Figure 4.4 (a) shows the C1s spectra of different membrane samples. For carbon in the CF_2 configuration, the binding energy (E_b) is ~ 291 eV (highest binding energy peak). The XPS peak at E_b = 284.2 eV can be related to the carbon in C–CF or C-C configuration. It is apparent that the intensity of the peak at 291 eV decreases when the Fe^{2+} concentration is increased; after treatment with the 300 ppm Fe^{2+} solution, this peak is nearly undetectable, indicating that the (CF_2)n polymer backbone has decomposed. However, the intensity of the peak at 284.2 eV for samples 2 and 3 has increased,

indicating that the relative concentrations of C-C or C-CF configurations have increased with increasing Fe^{2+}.

These results demonstrate that fluorine atoms are removed from the CF_2 bonding configuration to form fluorine depleted configurations as a result of treatment with Fenton's reagent. For the highest Fe^{2+} concentration (sample 1), the CF_2 intensity decreased and the binding energy shifted to lower values. Such observations are consistent with a removal of fluorine atoms, resulting in a reduced binding energy for C1s.

Figure 4.4 (b) shows the O1s spectrum for different membrane samples. Oxygen in Nafion® membranes has two different binding states. Three oxygen atoms are bound in each sulfonic acid group, indicated by E_b = 535.7 eV (highest binding energy peak). Two of the oxygen atoms in the polymer chain are in ether configurations with E_b = 533 eV (lower binding energy peak). After treatment of samples 1, 2, and 3 (Table 4.1) in Fenton's reagent, only the ether bonding configuration is observed. Furthermore, with an increase in Fe^{2+} concentration, the oxygen binding energy is shifted to lower values. This shift is consistent with the formation of an oxo-bonded iron complex on the membrane surface [62, 63] along with the loss of $-SO_3H$ groups from the membrane. Such results also agree with the detection of SO_4^{2-} in the exhaust water by ion chromatography.

Figure 4.4 (c) shows the S2p spectrum for different membrane samples; S2p electrons have a binding energy of 168 eV. The binding energy of sulfur does not change after exposure to Fenton's reagent, but the signal intensity decreases, indicating a loss of sulfur from the polymer. Such observations and conclusions are consistent with the changes observed in the O1s spectrum and the detection of SO_4^{2-} in the effluent [27].

Figure 4.4 (d) shows the F1s spectrum for different membrane samples; F1s electrons have a binding energy of 688 eV. A substantial decrease in peak intensity has occurred as a result of the Fenton's reagent treatment. In fact, for the highest Fe^{2+} concentration (sample 1), the fluorine signal is weak, indicating a low fluorine atomic percentage (Figure 4.4 (d) and Table 4.1).

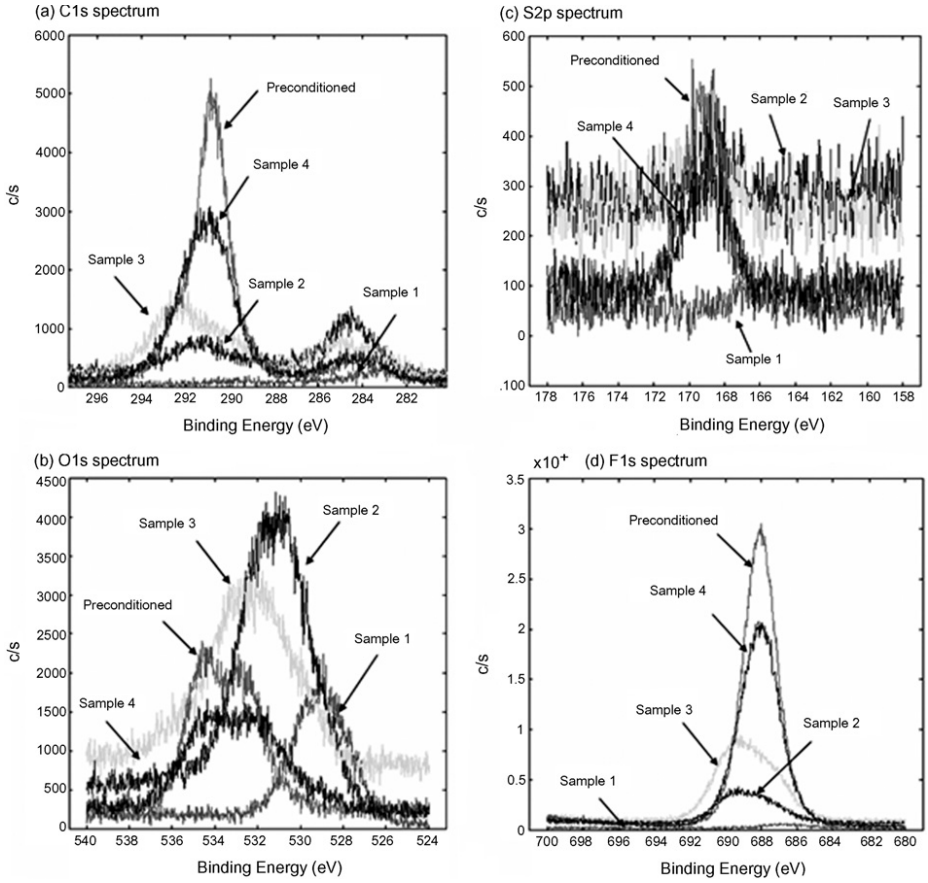

Figure 4.4. XPS spectra of different membrane samples.

4.3.3 Atomic percentage data analyses

Table 4.1 gives the treatment conditions and quantitative (peak fitting) XPS results for various samples that were exposed to Fenton's reagent. Limited changes in elemental concentrations were observed after Fenton's test at 60 ^{o}C (sample 4). These

results are consistent with the FER data from Figure 2, which shows that the FER at 80 ^{o}C is three times larger than that at 60 ^{o}C. Such observations are expected, since the polymer degradation rate should be reduced at lower temperatures.

Table 4.1 XPS results for different samples in Fenton's test

(H_2O_2 concentration is fixed at 10 wt%)

	Treatment conditions			Element composition in atom%				
	$[Fe^{2+}]$ (ppm)	T (^{o}C)	Time (hr)	C	O	S	F	Impurities
Pretreated	-	80	-	31.5	8.4	1.3	58.8	-
Sample 1	300	80	24	20.2	53.1	1.4	5.8	19.5
Sample 2	30	80	24	27.8	36.6	0.9	21.3	13.4
Sample 3	3	80	24	29.7	19.5	1.4	44.7	4.7
Sample 4	30	60	8	32.4	8.7	1.3	57.7	-

The oxygen concentration in the polymer increases during each test, whereas the sulfur concentration remains low. This result indicates that most of the oxygen atoms are not bonded to sulfur. Two plausible reasons for the increase in oxygen concentration can be offered. First, the main contribution is likely due to the oxo-bonded iron complex. Since the hydrophilic sulfonic acid group in the side chain can move from the membrane bulk to the surface during treatment [64], the oxo-bonded iron complex can form after a proton in $-SO_3H$ is exchanged with a ferric ion in Fenton's reagent [62]. However, the oxygen concentration in the polymer still increases even after subtracting the maximum number of oxygen atoms bonded to iron (in the form of Fe-OOH). Second, although

carbon and fluorine are removed as a result of chemical attack and replaced by oxygen, there is also considerable oxygen loss from the removal of $-SO_3H$ groups. Therefore, loss of carbon and fluorine is probably not the dominant reason for the increase in oxygen concentration in the polymer. The most probable source of oxygen is from the hydroxyl free radical (·OH). Attack of the polymer chain by this radical forms O-O or C=O moieties. The atomic ratio of carbon to oxygen drops after each test. The high oxygen content relative to carbon suggests the formation of polymeric species that contain large amounts of oxygen. That is, one result of chemical attack of the polymer chain may be the formation of peroxide or carbonyl groups in the degraded membrane.

4.4 FTIR Studies of the membrane

In order to verify XPS results, FTIR was used to study the chemical structure of Nafion® membranes before and after Fenton's test. Figure 4.5 shows the FTIR spectra of initial, pretreated, 3 ppm Fe^{2+} treated and 300 ppm Fe^{2+} treated (both with 10% H_2O_2) membrane samples. Spectra of initial and pretreated Nafion® membranes are consistent with observations on Nafion® membranes reported previously [65, 66]. The broad absorption between 3700 and 2900 cm^{-1} is assigned to the fundamental stretching vibration of water. A shift of this band from 2900 cm^{-1} to 3200 cm^{-1} is observed in the tested membrane. This shift results from the fact that the band at 2900 cm^{-1} can also be assigned to the stretching band of H_3O^+ [65]. That is, after Fenton's test, some of the protons attached to sulfonic groups have been exchanged with Fe^{2+} or Fe^{3+}, thereby decreasing the H_3O^+ content in the membrane and resulting in a peak shift. This conclusion is consistent with the disappearance of the band at 1710 cm^{-1} in the degraded

membrane, which corresponds to the H_3O^+ asymmetric bending mode [65] The band at 2200 cm^{-1} is assigned to the CF_2 stretching combination [67, 68]. A shift to higher wave number accompanied by an intensity decrease was observed for tested membranes, which demonstrated a loss of CF_2 groups in the degraded membrane and is consistent with XPS spectra. The band at 1630 cm^{-1} is assigned to the HOH fundamental bending mode [21,24]. It should be noticed that on the high wavenumber shoulder of this peak a weak but broad band appears; this spectral region is enlarged in Figure 4.6. The band at 1765 cm^{-1} may be assigned to the carbonyl bond in esters or carboxylic acids. Such observations offer evidence of the formation of oxygen-rich groups such as esters or carboxylic acid groups, which is in agreement with XPS results. A very weak absorption at 1434 cm^{-1} is also evident; this peak has been assigned to a cross-linking S-O-S band by J. Qiao et al. [38] This assignment can be further verified by the fact that two water bands appear in the range 3000-4000 cm^{-1}. In the previous degradation [38] study using H_2O_2, these peaks were not observed until the membrane was exposed to H_2O_2 for 3 weeks; this can be compared to 24 hours of exposure to Fenton's test in our study. Such observations indicate that free radicals will aggressively attack the membrane and lead to the loss of sulfonic groups which may cause performance decay in fuel-cell tests. Another absorption detected is the band at 870 cm^{-1}, which can be assigned to oxo-bonded Fe-O-Fe in Fe^{3+}-Nafion [62]. However, since the O-O stretch in Nafion® has also been reported [69] to be in this narrow range (845 – 875 cm^{-1}), this peak could be due to O-O, or to a combination of O-O and Fe-O-Fe bands.

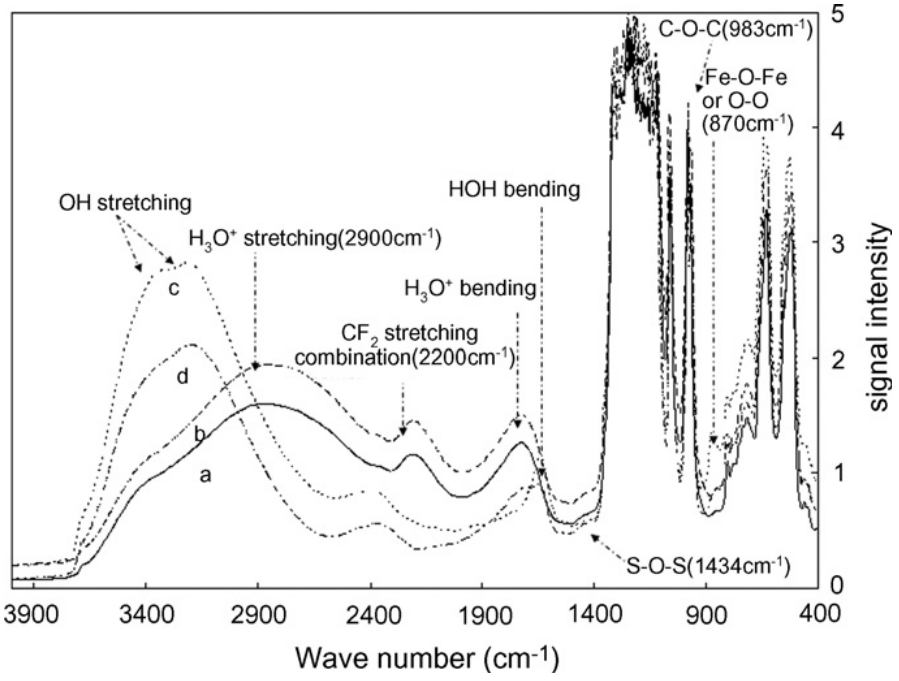

Figure 4.5. FTIR spectra of initial, pretreated and tested membrane samples: a(——) initial membrane sample, b(- - - - -) pretreated membrane sample, c(·····) 300 ppm Fe^{2+} treated membrane sample, d(- · - · -) 3 ppm Fe^{2+} treated membrane sample.

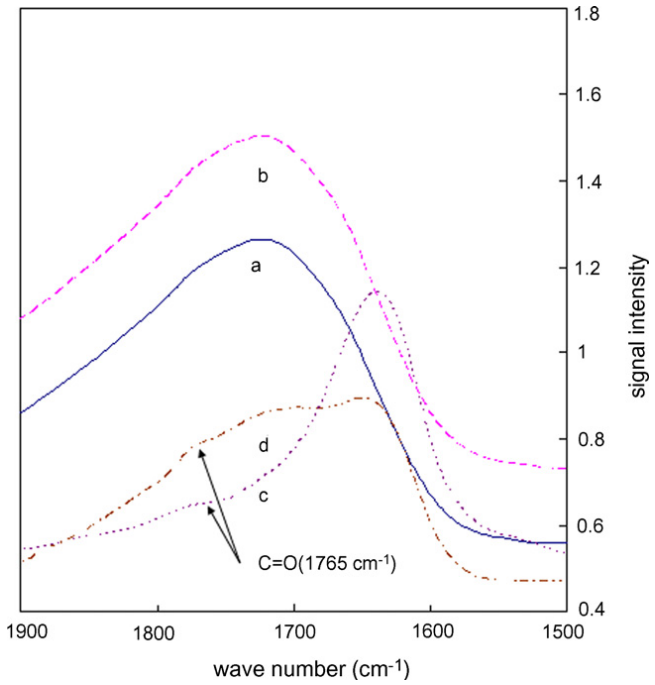

Figure 4.6. FTIR spectra of membrane samples in 1900 cm^{-1} and 1500 cm^{-1} short range: a(——) initial membrane sample, b(- - - -) pretreated membrane sample, c(·····) 300 ppm Fe^{3+} treated membrane sample, d(- · - · -) 3 ppm Fe^{3+} treated membrane sample.

4.5 Degradation mechanism in Fenton's test

Based on the experimental results provided above, the degradation mechanism of Nafion® can be considered to occur via two schemes. The first scheme occurs due to the attack of defects in the main chain such as "residual" C-H bonds that have been reported to exist in the Nafion® polymer [70]. It is well-known that carbon-fluorine bonds are strong (~ 460 kJ/mol) compared to carbon-hydrogen bonds (~ 410 kJ/mol) [71]. In fact, C-F bonds are responsible for the chemical stability of Nafion® membranes, and are thus unlikely to be attacked extensively by free radicals. However, defects such as C-H or C=C bonds, which may form in the polymer during the manufacturing process, are sufficient to initiate radical reactions and eventually degrade Nafion® [70]. These defects can be attacked by hydroxyl or hydroperoxy radicals to form carbon-centered radicals, which have been observed by EPR studies [51, 53]. The carbon-centered radical is not stable; thus, it can undergo further radical reaction with hydroxyl radicals or even O_2 and water to generate more stable peroxyl radicals or ester structures and thereby produce fluoride ions and polymer fragments. This process can lead to the cleavage of polymer chains, which is referred to "decomposition of $(CF_2)_n$ polymer backbone". Another degradation scheme is associated with the end group $–SO_3H$, the first step of which is the formation of cross-linking S-O-S bonds under the strong oxidation effect of H_2O_2 and free radicals. This anhydride may react with another sulfonic acid group to produce a

sulfonate ester and release SO_2 gas, which has been detected in the exhaust gas of fuel cells by direct gas mass spectroscopy (DGMS) [25]. Reaction of this ester with water produces a carboxylic acid that can be further attacked by hydroxyl radicals. This reaction of the $–SO_3H$ group may account in part for the non-zero intercept in plots of fluoride generation rate versus carboxylic acid content in Nafion® [28]. That is, the sulfonic acid end group could be an additional point of attack by peroxide after transformation into a carboxylic acid end group occurs via the above scheme. Moreover, S. Hommura et al. reported that the carboxylic acid content in the membrane increased during OCV tests [72], which also indicates the possibility of –COOH formation from $–SO_3H$ groups. This scheme is analogous to one of the degradation schemes reported for Nafion® during thermal degradation [73]. However, it should be stressed that this process is kinetically very slow under fuel-cell conditions compared to the degradation of carboxylic acid end groups; as a result, this mechanism may explain the observed continuous fluoride ion emission during the fuel-cell lifetime.

4.6 XPS spectra of the MEA

Figures 4.7 (a) – 4.7 (d) show XPS spectra of the electrode surface of both fresh and degraded MEA. Because the electron mean free path in solids is <10 nm, XPS samples only near surface regions, and thus yields chemical information regarding the electrode surface, which contains Pt catalyst and Nafion® ionomers. No significant difference between the structure of fresh and degraded MEA was found by XPS. However, analysis of the water collected from the anode and cathode regions showed that ~ 8.4% of the total fluorine was lost after 236 hrs of operation. Such results suggest that

the Pt catalyst in the electrode may help to protect Nafion® ionomers from degradation [44]. If this is correct, the degradation may occur primarily within the membrane or in the electrode but near the membrane interface. Further XPS and FTIR analyses, including depth profiling of the membrane separated from MEA is therefore required to obtain additional insight into the membrane degradation mechanism.

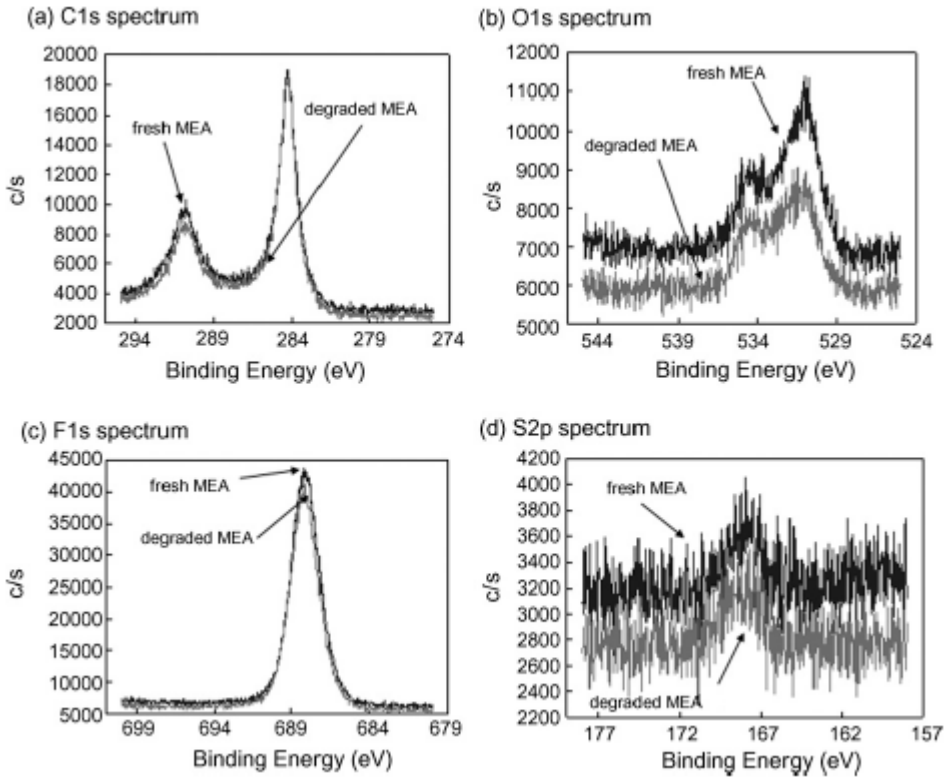

Figure 4.7 XPS spectra of fresh and degraded MEAs.

4.7 Summary

Fenton's tests on Nafion® membranes demonstrate the effects of Fe^{2+} concentration and temperature on membrane degradation. Under various Fe^{2+} concentrations, different degradation products were generated. With increasing Fe^{2+}

concentrations, the fraction of degradation products that are polymer fragments increase. Furthermore, membrane degradation is accelerated at high temperatures. After pretreatment and Fenton's test, Nafion® membrane samples were analyzed by XPS to investigate chemical changes in the polymer. Results indicate that X-ray radiation has little effect on membrane degradation even up to 2 hours of exposure. These observations confirm that changes in XPS spectra of treated membranes give an indication of chemical bonding and composition changes resulting from treatment with Fenton's reagent. Carbon XPS studies of membranes after treatment show an intensity decrease in the bonding peak related to the CF_2 configuration. Analyses of the O1s spectra suggest that the oxygen present after treatment is primarily in the ether configuration or bonded with iron, since $-SO_3H$ groups have been diminished. The loss of fluorine and sulfur as indicated by S2p and F1s XPS spectra is consistent with the detection of F^- and SO_4^{2-} in exhaust water from MEAs during fuel-cell operation. Oxygen atom analyses indicate that chemical groups with a high carbon to oxygen ratio are generated in the membrane, apparently due to free radical attack of the polymer backbone by ·OH. FTIR studies verified the formation of oxygen-rich moieties in the degraded membrane, since C=O and O-O bands were evident in the spectra. Moreover, formation of cross-linking S-O-S was observed which can initiate further degradation by producing carboxylic acid groups. Two membrane degradation schemes have been proposed: degradation initiated by polymer defects and by cross linking of sulfonic end groups. No significant difference between fresh and degraded MEAs is found in the XPS spectra, indicating that membrane degradation likely occurs at the electrode-membrane interface or within the membrane bulk. Further XPS and FTIR analyses, including depth profiling of the membrane

separated from MEA is therefore required to obtain additional insight into the membrane degradation mechanism.

CHAPTER 5

IN-SITU FUEL-CELL DURABILITY TESTS

Although *ex-situ* Fenton's test has many advantages and provides important information on membrane degradation, it is difficult to study the influence of different operational parameters such as relative humidity, temperature and gas partial pressures on membrane degradation solely by such a test. These parameters, especially humidity and temperature, are extremely important to fuel-cell operation and membrane lifetime. In this chapter, the effects of relative humidity, temperature, oxygen partial pressure and water transport were studied to reveal their relationship with membrane degradation.

5.1 Initial FER Stability Test

In order to make the data more reliable, it must be assured that the fluoride ion emission from the membrane has reached a pseudo steady state when collecting the water. As shown in Figure 5.1, a ten-hour durability test was carried out to verify the consistency of degradation rates. Cathode FERs showed very good stability from beginning to end. It only took two hours for the anode FERs to become stable. Therefore, in all the fuel-cell tests after varying the operation conditions, before collecting water samples, at least 2 ~ 3 hours were always allowed to make sure that FERs at both anode and cathode achieved steady state.

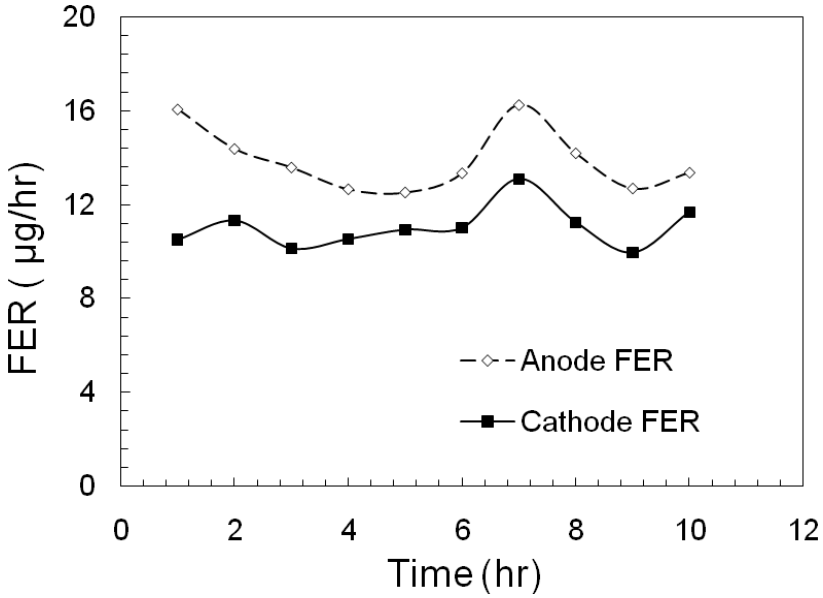

Figure 5.1. Anode and cathode FER stability test in initial ten hours.

Operating conditions: H_2 // Air, T_{cell} = 65 ^{o}C, Ambient Pressure, RH = 100 %, OCV.

5.2 Cell performance before and after test

Figure 5.2 shows the MEA performance before and after the open-circuit voltage (OCV) test. MEA performance decay was clearly observed after one week's durability test. Significant performance decay occurs in the low current region, which is mainly ascribed to the decrease in ORR activity of the Pt catalyst. The ohmic loss, which corresponds to membrane resistance, remains constant during the OCV test. It indicates that no significant change occurs in membrane conductivity. Therefore, the decomposition of sulfonic acid group is not the major degradation scheme under such experimental conditions. The degradation is a slow process under normal conditions although it can be de catastrophic after long time operation for automobile applications. An accelerated durability test protocol needs to be developed in order to study the

membrane structural change and degradation mechanism in a relatively short period of time.

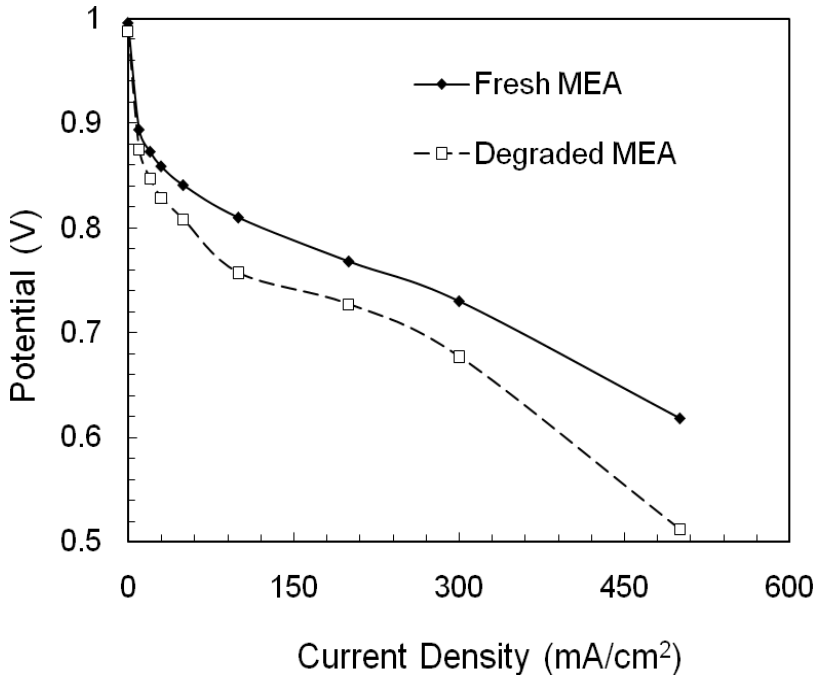

Figure 5.2. MEA Performance before and after membrane degradation.

Operating conditions: H_2 // Air, T_{cell} = 65 ^oC, Ambient Pressure, RH = 100 %, OCV, total testing time 7 days.

5.3. Effect of relative humidity

Figure 5.3 shows the effect of relative humidity on membrane degradation using pure oxygen as cathode gas. Both cathode and anode FERs increase with a decrease in relative humidity. The increase in FERs becomes more rapid as the humidity is lowered. The curve shows similar pattern as water-sorption isotherms of Nafion® [74], which suggests the strong correlation between the degradation and water content in the membrane. This effect will be exclusively discussed later in the chapter 7.

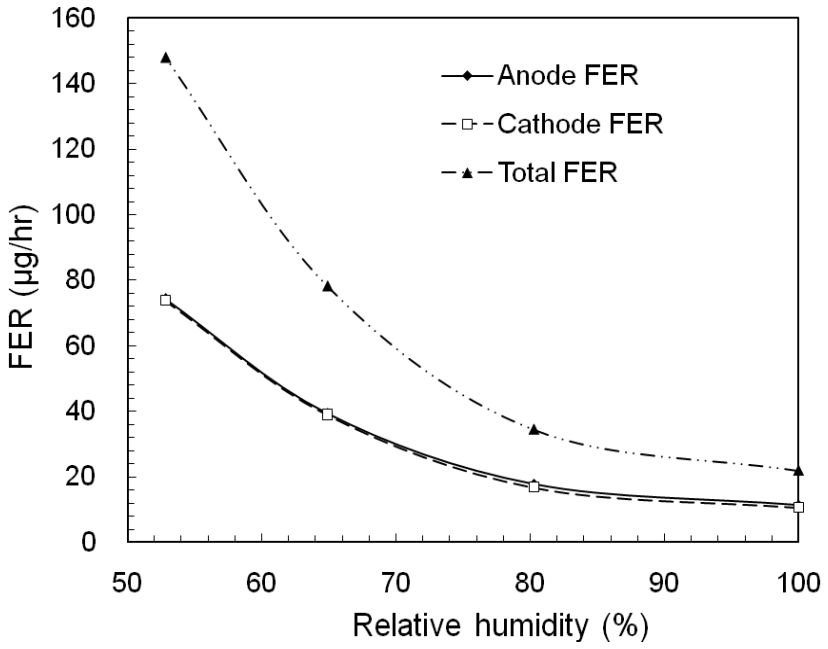

Figure 5.3. Effect of relative humidity on FER.

Operating conditions: H_2 // O_2, T_{cell} = 65 ^oC, Ambient Pressure, OCV.

5.4 Effect of oxygen partial pressure

Because the formation of H_2O_2 at the anode is dependent on oxygen crossover, oxygen partial pressure at cathode has significant impact on the rate of membrane degradation. Figure 5.4 shows the effect of oxygen partial pressure on membrane degradation. As expected, high oxygen partial pressure, resulting high oxygen permeation through the membrane, generates more free radicals and membrane degradation is accelerated. But this impact becomes weak when the oxygen partial pressure at cathode drops below 5 %. In contrast, FERs increased tremendously under high partial pressure, even by an order of magnitude. It indicates that oxygen crossover may not be the rate-limiting step when oxygen concentration is very low.

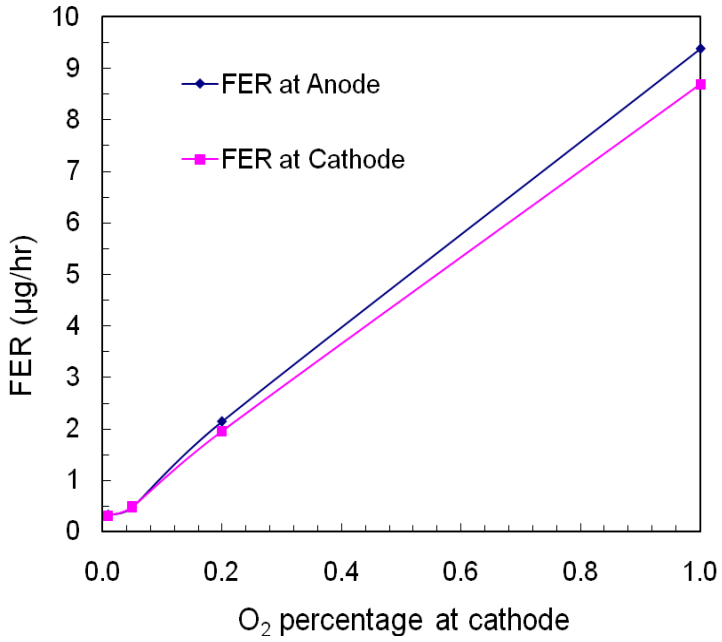

Figure 5.4. Effect of oxygen partial pressure on FER. Percentage of oxygen is on a dry basis. Operating conditions: Anode gas H_2, T_{cell} = 65 ^oC, Ambient Pressure, RH = 100 %, OCV.

5.5 Effect of temperature

Figure 5.5 shows the effect of temperature on membrane degradation. Obviously, degradation rates increases with temperature, which should be attributed to the accelerated kinetics of both oxidative species formation and degradation reactions. The straight line represents a fit to the Arrhenius equation, resulting in an apparent activation energy for degradation of ~ 13 kJ mol^{-1}, which is less than the value of ~ 39.5 kJ mol^{-1} of Fenton's reaction and may be due to the change of gas partial pressure under different temperature since the gases are all fully humidified. However, since these FER data was determined under relatively milder conditions (low temperature and high humidity); in

the chapter 8 we will see a dramatic increase of activation energy in fuel-cell test under highly accelerated conditions.

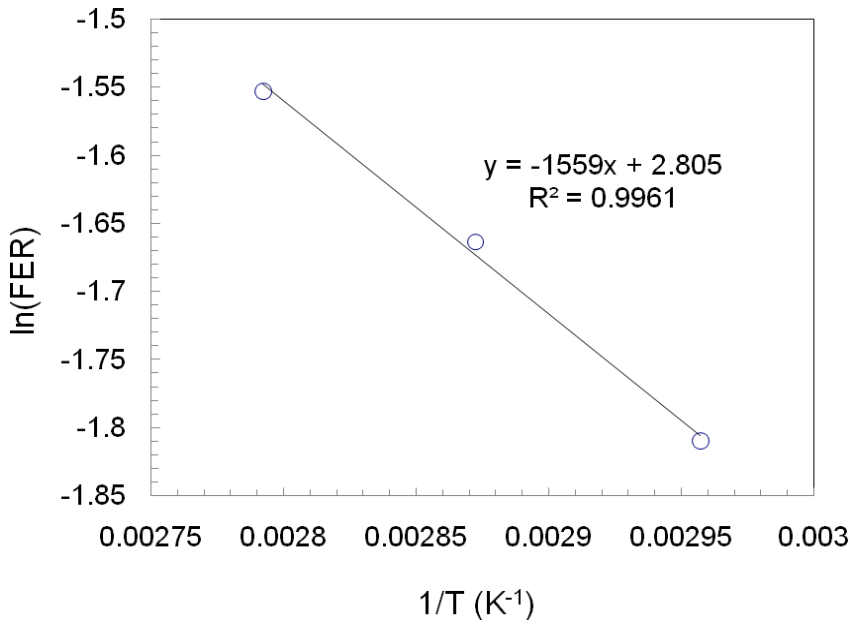

Figure 5.5. Effect of temperature on FER.

Operating conditions: H_2 // Air, T_{cell} = 65 ^oC, Ambient Pressure, RH = 100 %, OCV.

5.6 The effect of water transport

Water management is critical to fuel-cell operation and has a strong impact on membrane degradation since low level of water content in the membrane was proved to accelerate degradation. Here, we kept either the cathode or the anode under fully humidified condition and varied the humidity on the other electrode to study the effect of water transport on membrane degradation.

Figure 5.6 (a) shows the change of FER with cathode RH when the anode RH was kept at 100%. We can see that FER increases with the decrease of humidity and the FERs from both anode and cathode are nearly the same. However, when RH at cathode was

kept at 100% and the anode RH decreased as shown in Figure 5.6 (b), FERs increase quickly especially at anode side, which seems to be more sensitive to the humidity change. More interestingly, the FERs at both anode and cathode stopped increasing when RH dropped below 50 %. The reason may be due to faster water transport from cathode to anode when anode is completely dry, less H_2O_2 arrived at cathode and the gas permeation was reported to increase with an increase of relative humidity [75]. Figure 5.6 (c) and (d) shows the outlet RH of different tests calculated from the amount of exhaust water. Since water transports is fast in Nafion® membrane and the membrane thickness is only 50 μm, all the tests achieved equilibrium at the outlet which can be observed by the same outlet humidity of anode and cathode. This condition is closer to fuel cell operation with loading, therefore, proton transport electro-osmotically drags water from the anode [76], lowering the water content at the anode and exacerbating the degradation. Therefore, reasonable humidity has to be kept at anode side in order to avoid fast membrane degradation.

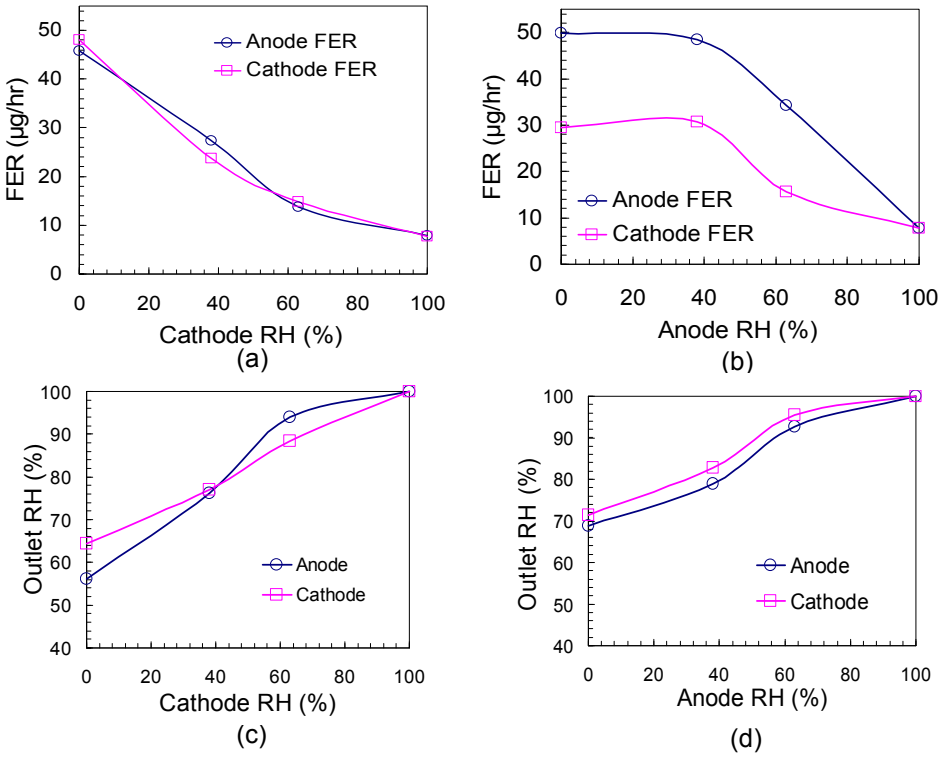

Figure 5.6. Effect of water transport on FER and outlet RH.

Operating conditions: H_2 // O_2, T_{cell} = 65 ^oC, Ambient Pressure, OCV.

(a) and (c): anode RH was kept at 100 %.

(b) and (d): cathode RH was kept at 100 %.

5.7 An example of long-term durability test

Figure 5.7 shows the FER and the rate of H_2 crossover during a long-term durability test. The FER increased quickly at the beginning and decreased subsequently until a pseudo steady state was achieved. H_2 crossover current remained at a low level until membrane failed at 242 hrs when a sudden increase of crossover current was observed. This behavior is typical of membrane failure caused by chemical attack. The test was stopped at 193 hrs and restarted after a day. After the test was restarted, FER

dropped and then increased back to the same level before stopping the test. A similar phenomenon was observed in other tests. This result indicates that the slow termination process occurs during membrane degradation, where the generated carbon radicals could combine together and reduce the available attacking sites. Since the increase of H_2 crossover current was observed, SEM images of cross section of degraded MEA were taken to study the formation of defects in the membrane. The formation of pinholes was clearly found in the membrane close to anode side, which confirms the degradation mechanism initiated by H_2O_2. Some cracks in the membrane were also observed and these cracks and pinholes are the main reasons for the high rates of gas crossover, which could ultimately result in the failure of the membrane electrolyte and even the whole fuel-cell system.

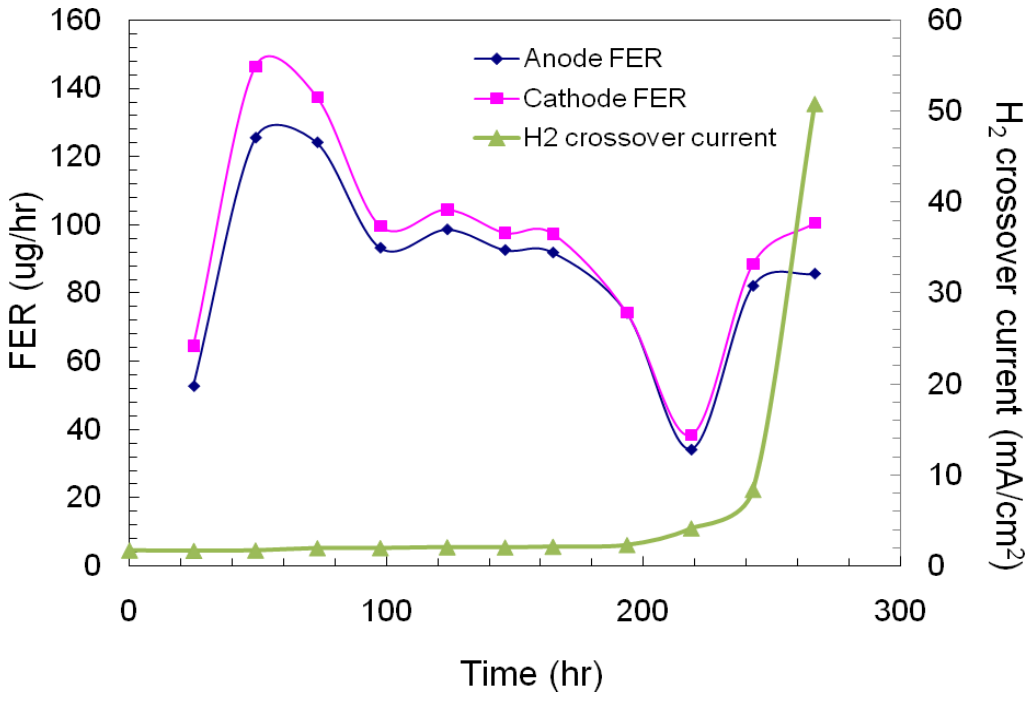

Figure 5.7. FER and H_2 crossover rate in a long-term durability test.

Operation conditions: Nafion® 112 MEA, $H_2//O_2$, T_{cell} = 75 °C, RH = 50 % at both sides, OCV, total testing time 266 hrs.

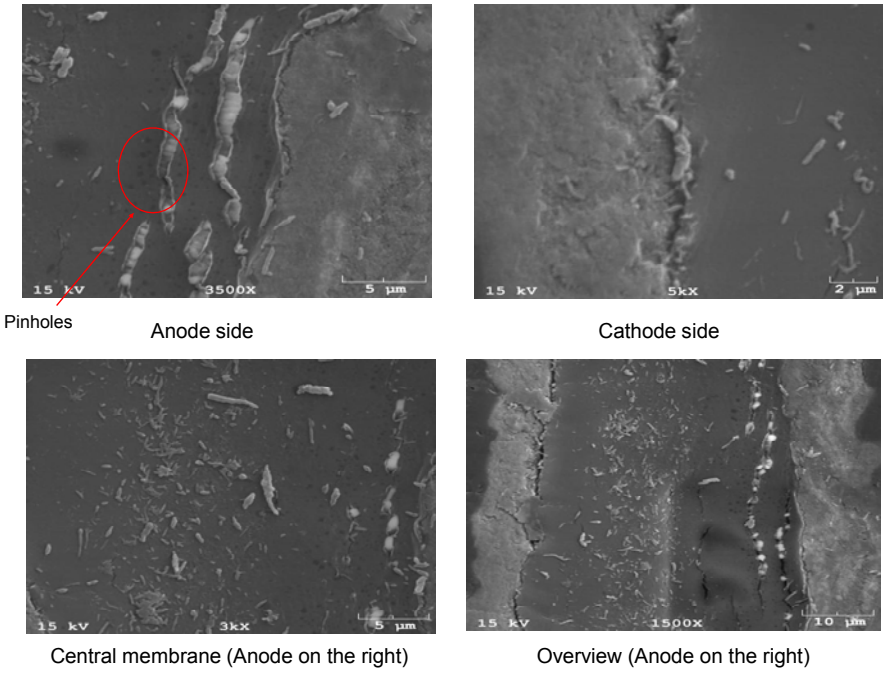

Figure 5.8. SEM images of MEA cross section.

5.8 Summary

In-situ fuel-cell tests were conducted to study the effect of operating conditions such as relative humidity, oxygen partial pressure and temperature on membrane degradation by measuring FER from exhaust water. It has been demonstrated that the fluoride ion emission from the membrane has reached a quasi steady state after only two hours of operation. Cell performance decay was observed after one week's durability test; however, catalyst degradation was determined to be the main reason. It was found that low relative humidity, high oxygen partial pressure and high temperature accelerated

membrane degradation. Water transport also impacts degradation and the anode side is more sensitive to this effect than the cathode. A long-term durability test shows a sudden increase of H_2 crossover when membrane failed and the formation of pinholes in the membrane that were observed close to the anode side of degraded MEA from SEM images.

CHAPTER 6

H_2O_2 DETERMINATION UNDER FUEL-CELL CONDITIONS

Although the detailed mechanisms of the chemical degradation are not fully understood, this chemical attack is believed to be due to formation of peroxide caused by the diffusion of oxygen across the membrane where it reacts with hydrogen. Therefore, the rate of chemical degradation of the membrane will depend on the rate of gas crossover. More recently formation of hydrogen peroxide has been detected in an operating fuel cell, and further the rate was strongly influenced by the thickness of the membrane, suggesting that transport of oxygen and hydrogen in the membrane may limit the formation of peroxide [36]. However, some researchers suggest the direct formation of radicals on Pt catalyst may be the main reason of degradation, although H_2O_2 can also be formed during the reaction between radicals [32]. Nevertheless, H_2O_2 formation is the key point in membrane degradation. Unfortunately, the formation of H_2O_2 in the fuel cell and its impact on chemical degradation are still unclear. The difficulty is that hydrogen peroxide decomposition rate is extremely high on platinum catalyst [47]. Therefore, novel H_2O_2 detection method under different fuel-cell conditions needs to be developed in order to elucidate the role of H_2O_2 in membrane degradation.

H_2O_2 is a very important reactant, intermediate and product in many reactions due to its oxidative and reductive characteristics; therefore a large number of analytical methods have been developed for micro and trace determination of H_2O_2 in either gas phase or liquid phase. These methods include titrimetry [77, 78], spectrophotometry [79, 80], fluorescence [81, 82], enzymatic methods [83], Raman spectroscopy [84], as well as

electrochemical methods [36, 85]. Spectrophotometry has been chosen as the preferred method owing to its widespread use in analytical laboratories.

6.1 Experimental Design

MEA Configuration - Due to high hydrogen peroxide decomposition rate on platinum catalyst, H_2O_2 measurement from the cell with normal configuration is difficult and the result could be unreliable. Therefore, three different MEA configurations were used: anode only, cathode only, and multilayer MEA as shown in figure 1 below. Anode only and cathode only MEA designs were the same as those described by Mittal *et al*. [32]

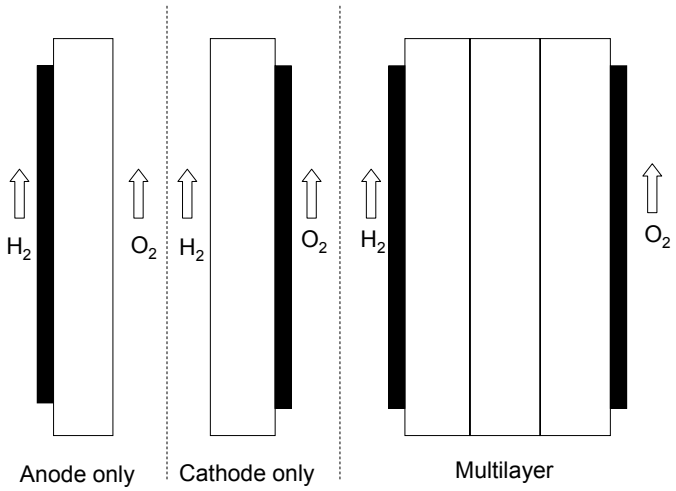

Figure 6.1. Schematic diagram of anode only, cathode only, and multilayer MEAs. Black and white areas denote Pt/C catalyst layer and Nafion® 112 membrane, respectively.

I_3^- methods - H_2O_2 concentration can be measured by a number of spectrophotometric methods owing to its oxidative and reductive ability. Since polymer

fragments such as Rf-COOH are reported to be a product of membrane degradation [34, 39], spectrophotometric method by oxidizing H_2O_2 will cause positive errors. Therefore, I_3^- method was chosen for H_2O_2 detection in membrane due to its accuracy ($\varepsilon_{max}(I_3^-)$ was measured to be 26450 M^{-1} cm^{-1}) and less interference from organic impurities [86]. The reactions of H_2O_2 with KI solution to produce I_2 and I_3^- can be described as follows:

$$H_2O_2 + 2I^- + 2H^+ \rightarrow I_2 + 2H_2O \qquad \text{(Reaction 6.1)}$$

$$I_2 + I^- \leftrightarrow I_3^- \qquad \text{(Reaction 6.2)}$$

I^- has two absorption peaks at 193 and 226 nm. I_3^- also has two broad absorption peaks at 288 and 350 nm. To avoid interference from the UV absorption of I^-, I_3^- spectrum at 350 nm was selected for measurement, and it has been found that the iodide ion does not absorb at 350 nm for KHP and ammonium molybdate [87]. It was also found that the UV absorption at 350 nm didn't change after mixing with 10 μg/g F^- standard solution, fuel-cell exhaust water from both anode and cathode or Nafion® 112 membrane.

Materials - Ammonium molybdate tetrahydrate and potassium iodide was obtained from Fisher Scientific Inc. (ACS reagent). Sodium hydroxide (98%) was purchased from J. T. Baker Inc. Potassium hydrogen phthalate (KHP; certified ACS) was also purchased from Fisher Scientific.

Procedures - Solution A and B for the I_3^- method were prepared according to the usual recipe [88]. Solution A consisted of 33 g of KI, 1 g of NaOH and 0.1 g of ammonium molybdate tetrahydrate diluted to 500 ml with DI water. Ammonium molybdate can catalyze Reaction 6.1 resulting in a half-life of ~ 2.5 s compared to a half-life of 8 min without it [86]. The addition of NaOH is used to stabilize KI solution and form a buffer solution with KHP to control the pH value of resulting solution. The pH

value of I_3^- solution should be controlled in a small range because in strong acid solutions I^- could be oxidized by O_2 in the air, showing an increase in absorbance with time [89].

For the multilayer MEA, after fuel cell was under stable operation for at least two hours, the reactants were stopped, and the central membrane removed. This procedure took less than 2 minutes so the H_2O_2 concentration inside membrane would not have significant change. Then membrane was soaked into prepared KI solution for 15 minutes to guarantee the H_2O_2 inside membrane was completely reacted. The UV absorption in result solution was measured by HP 8453 UV-Visible spectrophotometer. For anode and cathode only MEA, fuel-cell exhaust water from cathode and anode was collected correspondingly for a certain period of time and the H_2O_2 concentration in the exhaust water was also quantitatively determine by I_3^- method. The rate of H_2O_2 emission was calculated from the H_2O_2 concentration and the volume of water sample. The H_2O_2 detection limit of this method is less than 0.1 μg/g H_2O_2 in water. H_2O_2 concentrations in Nafion® membranes or fuel-cell exhaust water were calculated under different fuel-cell conditions such as relative humidities and oxygen partial pressures.

6.2 H_2O_2 measurement in multilayer MEA

6.2.1 H_2O_2 concentration under different relative humidities.

Figure 6.2 shows the H_2O_2 concentration inside membrane under different relative humidities. The volume of dry Nafion® 112 membrane with 25 cm^2 area is about 0.125 cm^3. Therefore H_2O_2 concentration based on dry Nafion® was calculated as: total H_2O_2 amount in the membrane (μg) / 0.125 cm^3. An increase in H_2O_2 concentration with relative humidity can be seen from the figure. This seems reasonable because gas

crossover in Nafion® membrane has been reported to increase at high relative humidities [29]. Considering membrane swelling, membrane volume was corrected by this equation: $V/V_0 = 1 + 0.0336*\lambda$ ($\lambda = n_{H2O}/n_{-HSO3}$). For example, the value of λ is reported to be 15 when membrane equilibrated with 100 % RH air; however, this value decreases to 2 when RH = 15 % [15, 90]. H_2O_2 concentrations in the sections that follow have all been corrected. After volume correction, H_2O_2 concentrations in membrane under various humidities are nearly on the same level of ~ 6 $\mu g/cm^3$. The H_2O_2 concentration inside membrane seems to be only dependent on membrane volume under certain temperature and gas composition. It indicates H_2O_2 concentration profiles are not strongly affected by relative humidities, whereas temperature and gas composition are important. That being said, the water content in membrane is greatly influenced by relative humidity, and H_2O_2 can be diluted by water. This corrected concentration still can not truly reflect the real H_2O_2 existing state and reactive concentration. Therefore, H_2O_2 concentration especially when related to membrane degradation needs to be further corrected, and ratio between H_2O_2 and H_2O in membrane was used to represent the intrinsic H_2O_2 reactive concentration. Figure 3 shows the ratio between H_2O_2 and H_2O in membrane under different relative humidities. Low humidity leads to high H_2O_2 concentration in membrane and may accelerate membrane degradation. Two reasons can be proposed for H_2O_2 concentration increase under low humidity: water content decrease in the membrane and gas partial pressure increase. The increase in gas partial pressure is caused by reducing water partial pressure in the gas phase at both cathode and anode under low humidity. For example, saturated water partial pressure in gas phase is 25 kPa at 65 °C [91], which makes H_2 and O_2 partial pressure of 75 kPa under this condition. However,

the water partial pressure under 30 % RH is only 7.37 kPa at the same temperature and it raises H_2 and O_2 partial pressure to 93 kPa. The increase in gas partial pressure leads to higher gas crossover [92] and accelerates H_2O_2 formation. Due to multiple effects of membrane swelling, water content and gas partial pressure change under different relative humidities, ratio between H_2O_2 and H_2O in membrane versus relative humidity can be fitted as a straight line as shown in the Figure 6.3. Worthy of mention, it does not suggest that the rate of membrane degradation is also linear with relative humidity. Membrane degradation is a more complicated process that is influenced by a number of factors such as metal contaminant level, catalyst loading, oxygen partial pressure, and membrane structure. Our objective is to show the trend of H_2O_2 formation with relative humidity, and thereby to correlate H_2O_2 formation with membrane degradation in order to elucidate the membrane degradation mechanism.

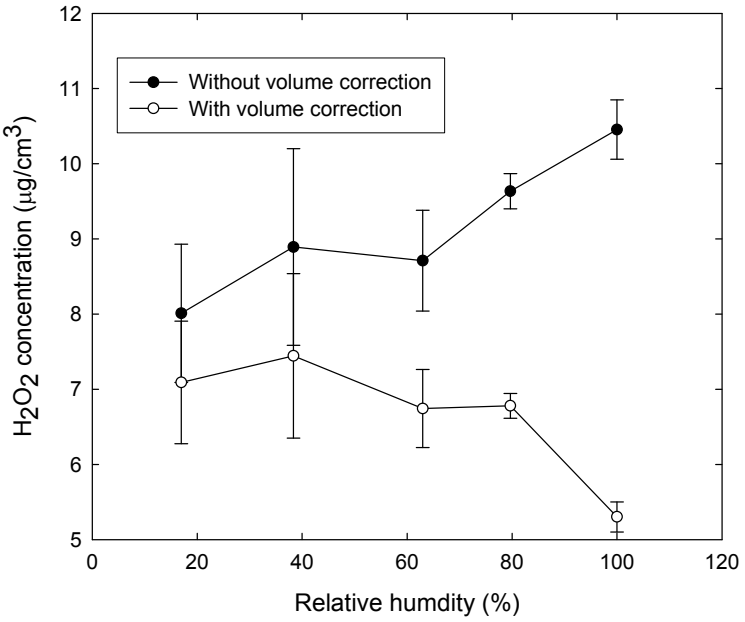

Figure 6.2. H_2O_2 concentration inside central membrane under different relative humidities.

Operating conditions: H_2 // O_2, T_{cell} = 65 ^oC, Ambient Pressure.

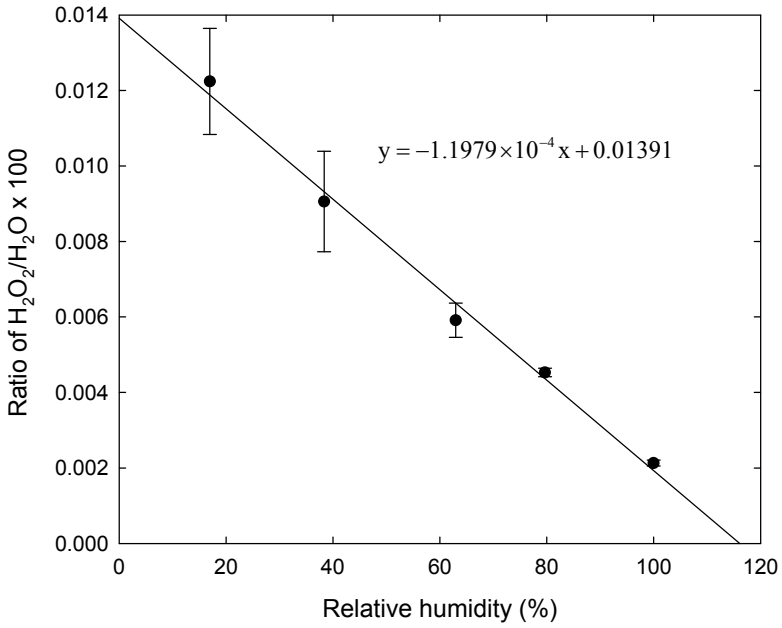

Figure 6.3. Ratio between H_2O_2 and H_2O in membrane under different relative humidities.

Operating conditions: H_2 // O_2, T_{cell} = 65 ^oC, Ambient Pressure.

6.2.2 H_2O_2 concentration under different oxygen partial pressure

Membrane degradation during fuel-cell operation is believed to be due to the formation of hydrogen peroxide caused by diffusion of oxygen across the membrane where it reacts with hydrogen. One way to increase oxygen crossover is to increase the oxygen partial pressure at cathode. Figure 6.4 shows H_2O_2 concentration under different oxygen partial pressures (from 1 % O_2 in nitrogen to pure O_2). The H_2O_2 concentration

increases with increasing oxygen partial pressure. However, H_2O_2 concentration didn't change significantly after switching from air to pure oxygen. This may be caused by a different H_2O_2 concentration profile inside the membrane under different oxygen partial pressures or may be an artifact of the technique. Since only central membrane was taken out for H_2O_2 measurement, H_2O_2 concentration in the center may not correctly reflect the total H_2O_2 amount if H_2O_2 concentration varies at different locations. For example, under pure oxygen condition, H_2O_2 may mostly concentrate near anode because much H_2O_2 is generated there, and its concentration may be low at the center. In order to clarify this, two Nafion® 112 membranes were put between two single-electrode MEAs and H_2O_2 concentration in each membrane was measured. H_2O_2 concentration in the membrane near anode was calculated to be 3.25 $\mu g/cm^3$, which was higher than the other membrane near cathode with 2.63 $\mu g/cm^3$. Therefore, in order to study the effect of oxygen partial pressure, H_2O_2 concentration near anode needs to be measured for further comparison. Moreover, H_2O_2 concentration is nonlinear with oxygen partial pressure, showing H_2O_2 may also be generated at cathode due to hydrogen crossover.

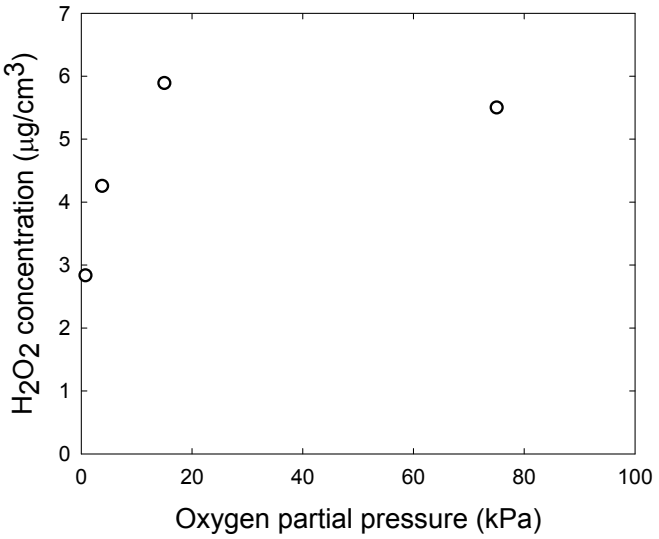

Figure 6.4. H_2O_2 concentration in central membrane under different oxygen partial pressures.

Operating conditions: Anode gas H_2, T_{cell} = 65 ^oC, Ambient Pressure, RH = 100%.

6.2.3 H_2O_2 concentration under different membrane thickness

H_2O_2 concentrations were also measured by putting Nafion® membranes with different thickness between two single-electrode MEAs (one Nafion® 112 membrane, two Nafion® 112 membranes and one Nafion® 117 membrane). Figure 6.5 shows the H_2O_2 concentration under different membrane thickness. Obviously H_2O_2 concentration decreases with increasing membrane thickness because both oxygen and hydrogen crossover are dependent on membrane thickness. This result is consistent with H_2O_2 measurement reported by Liu and Zuckerbrod [36] using *in-situ* Pt wire probes. Because of the increase in gas diffusion resistance at membrane interface, H_2O_2 concentration within two Nafion® 112 membranes is slightly lower than the value from linearly fitting line.

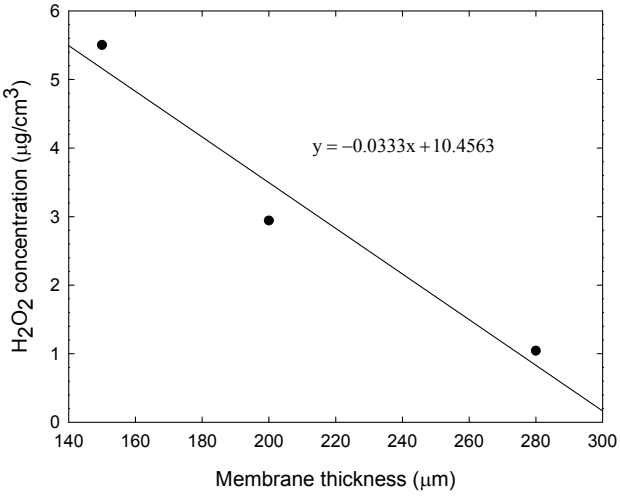

Figure 6.5. H_2O_2 concentration in central membrane under different membrane thickness. Operating conditions: H_2 // O_2, T_{cell} = 65 ^oC, Ambient Pressure.

6.3 H_2O_2 measurement in anode only MEA

6.3.1 H_2O_2 emission rates under different relative humidities.

Figure 6.6 shows the H_2O_2 emission rates under different relative humidities in anode only MEA. The anode gas was varied while the cathode gas was kept at 30 % humidity in order to transport H_2O_2 along with water from anode and increase the H_2O_2 concentration in cathode water for more accurate determination. It can be seen that low humidity increases the rate of H_2O_2 emission. This may be because under low humidity the H_2O_2 concentration gradient inside the membrane is increased due to the decrease of water amount. H_2O_2 emission rate at cathode is equal to H_2O_2 flux at the cathode-gas interface, which is determined by H_2O_2 concentration gradient there. On the other hand, the rate of H_2O_2 emission is directly proportional to H_2O_2 partial pressure in the gas phase under certain gas flow rate (fixed at 0.5 dm^3/min). Assuming H_2O_2 achieves phase

equilibrium at the cathode-gas interface, which can be described by Henry's law, low humidities increase H_2O_2 concentration there, therefore increases H_2O_2 equilibrium partial pressure and leads to high H_2O_2 emission rate.

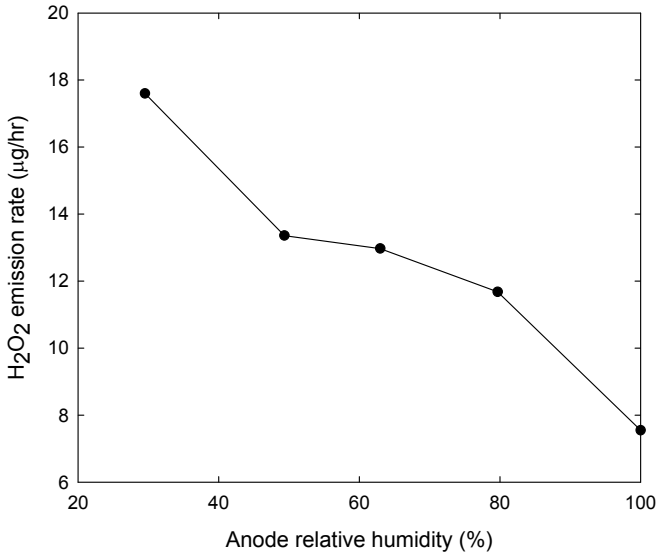

Figure 6.6. Effect of relative humidity on H_2O_2 emission rates in anode only MEA. Operating conditions: H_2 // O_2, T_{cell} = 65 ^oC, Ambient Pressure, RH = 30 % at cathode.

6.3.2 H_2O_2 emission rates under different oxygen partial pressures.

Rates of H_2O_2 emission were also determined under different levels of oxygen crossover by changing oxygen partial pressure. Figure 6.7 shows the effect of oxygen partial pressure on H_2O_2 emission rates in anode only MEA. As expected, high oxygen partial pressure, resulting in high oxygen crossover through the membrane, generates more H_2O_2. H_2O_2 emission rates are nearly linear to oxygen partial pressure above 3.75 kPa, which shows good agreement with anode H_2O_2 formation mechanism [36].

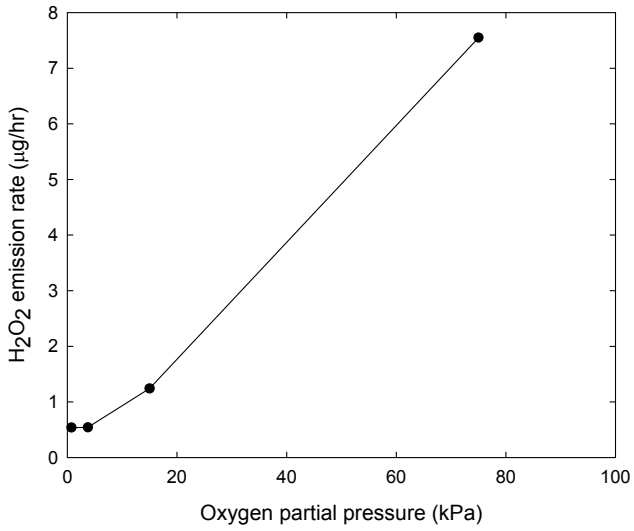

Figure 6.7. Effect of oxygen partial pressure on H_2O_2 emission rates in anode only MEA. Operating conditions: Anode gas H_2, T_{cell} = 65 ^oC, Ambient Pressure, RH = 100 % at anode and RH = 30% at cathode.

6.4 H_2O_2 measurement in cathode only MEA

Although Liu and Zuckerbrod [36] presented data indicating that peroxide was mainly generated at the fuel-cell anode, the cathode was shown to be the main point of peroxide attack by Zhang and Mukerjee [93]. It's reasonable because hydrogen can similarly penetrate from anode to cathode through membrane [92], react with oxygen there and generate H_2O_2. That being said, people generally believe H_2O_2 is not stable at the cathode due to high electrochemical potential [47]. In an operating fuel cell, the electrochemical potential in membrane (as measured with a reference electrode) is near the potential of the hydrogen electrode, H_2O_2 can be generated at membrane-electrode interface and transport into the membrane. Therefore, it is also important to study H_2O_2 formation at cathode due to hydrogen crossover. Figure 6.8 shows the effect of relative

humidity on H_2O_2 emission rates in cathode only MEA. Membrane cathode was operated at different humdities while anode was kept at 30 % humidity. Figure 8 shows that H_2O_2 emission rates from anode fluctuate under different relative humidities. Since they are only preliminary data, there may be some experimental difficulties here. Nevertheless, compared with H_2O_2 emission rates in anode only MEA, it is an order of magnitude lower here, which can explain why anode is the main location of H_2O_2 formation under this condition. However, H_2O_2 formation may be competitive at cathode and anode with the decrease of O_2 partial pressure.

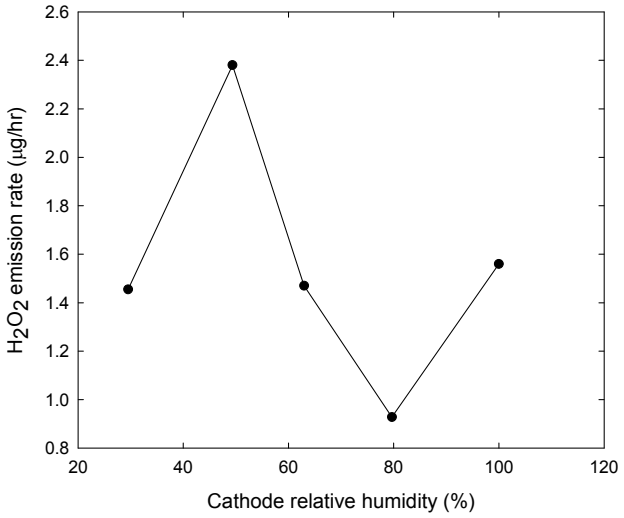

Figure 6.8. Effect of relative humidity on H_2O_2 emission rates in cathode only MEA. Operating conditions: H_2 // O_2, T_{cell} = 65 ^oC, Ambient Pressure, RH = 30 % at anode.

6.5 Summary

H_2O_2 formation under fuel-cell conditions was studied to help understand the mechanism of membrane degradation. Using a multilayer MEA, H_2O_2 concentrations in

Nafion® membrane were quantitatively measured by I_3^- method using UV-Visible spectrometer. Low humidity increase H_2O_2 concentration in the membrane and may accelerate membrane degradation. Multiple effects of membrane swelling, water content and gas partial pressure under different relative humidities give a linear relationship between H_2O_2 molar ratio in water and relative humidity. In general, H_2O_2 concentrations increase with increasing oxygen partial pressures, however, no significant change was found after switching from air to pure oxygen, which may indicate different H_2O_2 profile inside membrane or an artifact of this technique. Further study on different type of membrane indicates that H_2O_2 formation was depressed when increasing membrane thickness. In order to separately study H_2O_2 formation at anode and cathode, H_2O_2 emission rates were measured in anode and cathode only MEA. Low humidity and high oxygen partial pressure can increase H_2O_2 emission rate in anode only MEA. However, it was found the effect of humidity is not significant in cathode only MEA. In conclusion, H_2O_2 can be formed at the membrane-electrode interface of both anode and cathode due to gas crossover although the main product is water there; then H_2O_2 can diffuse through membrane and may cause membrane degradation. In the membrane, H_2O_2 can be decomposed by reaction with metal contaminants such as Fe^{2+}, Cu^{2+}. H_2O_2 concentration profile inside membrane can be further predicted by its formation at the electrodes, diffusion and decomposition in the membrane.

CHAPTER 7

MODELING OF H_2O_2 FORMATION IN PEMFCS

In Chapter 6, we developed a novel method to determine the H_2O_2 concentration in fuel cell; however, understanding of the mechanism is a key point to mitigate H_2O_2 formation and increase membrane durability. Here, we suggest the use of a complementary mathematical model to understand the mechanisms of H_2O_2 formation, transport and reaction in PEMFCs.

To date, such a model under fuel-cell conditions has not been reported; and only a few simulations based on RRDE (rotating ring disc electrode) experiments have been proposed. Dong et al. [94] observed phenomena, such as tails and humps in the polarization curves from RRDE experiments, that can be explained by the electrochemical reduction of peroxide and heterogeneous chemical decomposition reactions of peroxide. Several combinations of reactions were simulated to produce the polarization curves. These models were used to interpret experimental results by studying various reaction mechanisms including two-electron and four-electron oxygen reduction reactions as well as the electrochemical reduction of peroxide to water. However, the difference between the RRDE experiment and the fuel-cell test impedes the application of such experiments and models. Therefore, other mathematical models of the cathode electrode were proposed to predict the performance of the fuel-cell, but these treat only a direct four-electron oxygen reduction reaction.

The most generally accepted and successful model of the fuel-cell electrode is the agglomerate or flooded-agglomerate model, which assumes that the carbon support and platinum particles are packed into a small agglomerate and surrounded by electrolyte [95-98]. The agglomerate is approximated as spherical, porous catalyst particles that are separated by gas pores. The reaction inside the agglomerate can be modeled with an effectiveness factor. The reactants, such as oxygen, diffuse through the gas pores between agglomerates, dissolve into the electrolyte outside the agglomerate, and finally diffuse through the electrolyte inside the agglomerate to react on the surface of Pt catalyst.

Our objective is to use the agglomerate model to simulate the oxygen reduction reaction on Pt catalyst by considering a two-electron reduction reaction and study H_2O_2 formation under fuel-cell conditions. This will elucidate how material properties and operational conditions can mitigate membrane degradation. A model of oxygen permeation and H_2O_2 formation in PEMFCs is proposed, and the simulated results are compared with experimental data to validate this model. The profile of oxygen concentration and resulting H_2O_2 concentration distribution inside fuel cell are simulated. The average H_2O_2 concentration in the membrane is predicted under different operating conditions. Membrane properties, including membrane thickness, level of metal ion contaminants, oxygen diffusivity, were varied to evaluate their effects on H_2O_2 concentration in the membrane. Moreover, electrode properties such as thickness, catalyst activity, *etc*. are studied to minimize H_2O_2 formation in the fuel cell. Finally, some insights to reduce the formation of H_2O_2 and extend membrane lifetime are suggested.

7.1 Model Details

7.1.1 Model details

H_2O_2 formation in PEMFCs is depicted in Figure 7.1. First, oxygen is transported through the gas diffusion layer (GDL) and catalyst layer (CL) at cathode. Due to the permeability of oxygen in the ionomer, molecular oxygen can continue to diffuse through the membrane. At the anode, a possible H_2O_2 formation mechanism was described by LaConti *et al*. [99] based on the reaction between chemi-sorbed atomic hydrogen and an oxygen molecule that diffuses from the cathode. Decomposition of the formed peroxide is partially inhibited at the H_2-covered Pt electrode. An alternative H_2O_2 formation pathway is the two-electron oxygen reduction reaction (ORR) due to deactivation of direct four-electron ORR by adsorbed hydrogen [100]. On the other hand, we may assume these two pathways of H_2O_2 formation are similar at near zero potential (all potentials are referenced to a hydrogen electrode). We will demonstrate the similarity between them below. This is important since the kinetic rate constant of the reaction between a hydrogen atom and an oxygen molecule is difficult to obtain, whereas it's much easier establish the parameters of the oxygen reduction reaction. The generated H_2O_2 can be further reduced to H_2O via another two-electron reduction reaction. Given that the two-electron oxygen reduction reaction rate is inherently faster than the rate of peroxide reduction, one expects to observe peroxide formation in the cathodic consumption of oxygen [101]. Therefore, a small amount of H_2O_2 diffuses away from anode to enter either the gas phase or the ionomer membrane. H_2O_2 that gets into the membrane can continue to diffuse to the cathode, where it is completely decomposed due to the high potential of the cathode under open-circuit conditions.

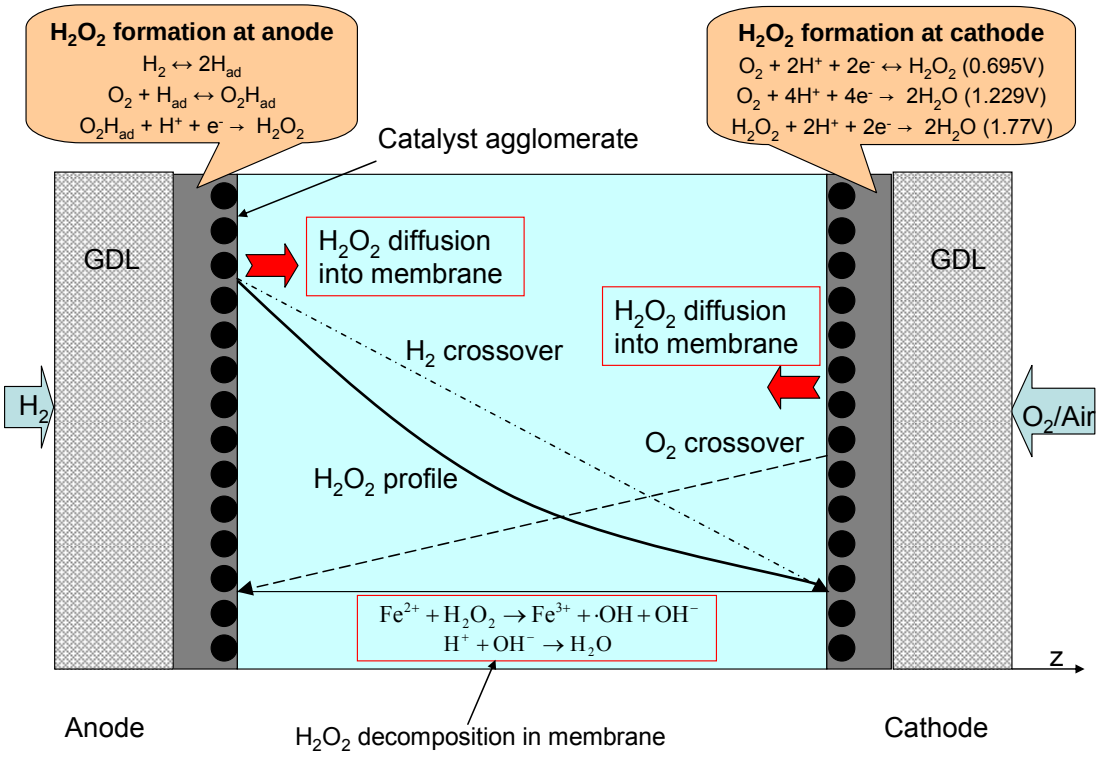

Figure 7.1. Schematic diagram of H_2O_2 formation under fuel-cell conditions.

In attempt to simulate the kinetics of H_2O_2 formation at the anode, the following possible reactions[1] are considered here [99]:

$$H_2 \underset{k_1'}{\overset{k_1}{\rightleftharpoons}} 2H_{ad} \qquad \text{(Reaction 7.1)}$$

$$O_2 + H_{ad} \underset{k_2'}{\overset{k_2}{\rightleftharpoons}} O_2H_{ad} \qquad \text{(Reaction 7.2)}$$

---

[1] Because of the low O_2 concentration at the anode, the reaction rate expression in equation (6) will stay the same even if O_2 adsorption on Pt is considered: $O_2 \rightleftharpoons O_{2,ad}$.

$$O_2H_{ad} + e^- + H^+ \xrightarrow{k_3} H_2O_2 \qquad \text{(Reaction 7.3)}$$

Assuming that reaction (2) is the rate-determining step (RDS) and neglecting the coverage of other species (-OH, -O_2H, -H_2O_2), the coverage of chemi-sorbed hydrogen atoms is calculated by Langmuir adsorption equation:

$$\theta_H = \frac{(K_{eq}c_{H2})^{1/2}}{(K_{eq}c_{H2})^{1/2}+1} \qquad \text{(Equation 7.1)}$$

Invoking the stationary-state assumption,

$$\frac{d\theta_{O2H}}{dt} = k_2\theta_H c_{O2} - k_2'\theta_{O2H} - k_3\theta_{O2H} = 0 \qquad \text{(Equation 7.2)}$$

$$R_{O2} = R_{H2O2}^{Formation} = k_3\theta_{O2H} = \frac{k_3k_2c_{O2}(K_{eq}c_{H2})^{1/2}}{(k_2'+k_3)((K_{eq}c_{H2})^{1/2}+1)} \simeq k_2c_{O2}\frac{(K_{eq}c_{H2})^{1/2}}{(K_{eq}c_{H2})^{1/2}+1}$$

(Equation 7.3)

As we can see, the rate of H_2O_2 formation is linear with O_2 concentration and depends on the concentration of H_2 at anode. An alternative expression of reactions (7.1) – (7.3) is the two-electron oxygen reduction reaction at cathode where the rate of H_2O_2 formation is also directly proportional to the O_2 concentration and dependent on the H_2 partial pressure [100].

$$O_2 + 2H^+ + 2e^- \rightarrow H_2O_2(0.695V)\,. \qquad \text{(Reaction 7.4)}$$

Let A_c be the specific surface area of Pt catalyst. For porous electrode, a macrohomogeneous reaction rate can be written as:

$$R_{O2} = \frac{i_{O2}}{2F * A_C * c_{O2,ref} * (1-\varepsilon_{CL})}\left(\frac{c_{H+}}{c_{H+,ref}}\right)^2 \exp\left(\frac{-\alpha_{O2}F(E_a - E_{O2})}{RT}\right)c_{O2}$$

(Equation 7.5)

For hydrogen electrode, the anode potential can be expressed by Nernst Equation:

$$E_a = E^0 - \frac{RT}{2F}\ln\left(\frac{P_{H2}}{a_{H+}{}^2}\right) \qquad \text{(Equation 7.6)}$$

Clearly, the anode potential deceases with increasing hydrogen partial pressure, resulting in faster oxygen reduction reaction in Equation (7.4), the same case as in Equation (7.3). As evident from RRDE test [100], H_2O_2 production is greatly enhanced in low potential region due to deactivation of adsorbed hydrogen. Let's consider an ideal case when adsorption sites are totally covered by hydrogen. Then oxygen reduction reaction only forms H_2O_2 so the two pathways should be exactly the same. Therefore, the kinetic parameters in equation could be obtained from the two analogous H_2O_2 formation pathways as shown in the appendix.

On the other hand, H_2O_2 is reduced on Pt when the potential is below 1.77 V via the following reaction:

$$H_2O_2 + 2H^+ + 2e^- \rightarrow 2H_2O(1.77V)\,. \qquad \text{(Reaction 7.7)}$$

In the membrane, H_2O_2 can be decomposed by trace amount of metal contaminants, such as Fe^{2+}, via Fenton's reaction:

$$Fe^{2+} + H_2O_2 \rightarrow Fe^{3+} + OH^- + \cdot OH\,, \qquad \text{(Reaction 7.8)}$$

$$H^+ + OH^- \rightarrow H_2O \qquad \text{(Reaction 7.9)}$$

Fe^{2+} or other metal cations can bind to the sulfonic acid moiety in ionomer side chain via ion exchange with protons. Only those in solution can freely react with H_2O_2, and the equilibrium can be represented as:

$$M^z(m) + zH^+(s) \leftrightarrow M^z(s) + zH^+(m)\,. \qquad \text{(Reaction 7.10)}$$

Normally, metal contaminant levels are less than 100 ng/g (ppb) in the water, so 20 ng/g Fe^{2+} was selected as the base case. However, due to the strong affinity of Fe^{2+} on

the ionomer [102], the concentration of Fe^{2+} in ionomer membrane (such as Nafion®) could be much higher, even at the μg/g (ppm) level. According to the NEDO report from Mitsuda the iron (II) concentration is likely to be on the order of 1 μg/g [103].

7.1.2 Oxygen permeation and H_2O_2 formation model

In order to simulate H_2O_2 formation under fuel-cell conditions, the concentration of O_2 in the electrode must be calculated first. Assuming steady state, a differential mass balance on species *i* (O_2 and H_2O_2) gives,

$$\nabla \cdot N_i - R_i = 0, \qquad \text{(Equation 7.11)}$$

where R_i is a macrohomogeneous reaction rate. At the anode, we use the agglomerate model to simulate the O_2 reduction reaction to generate H_2O_2. As shown in Figure 7.2, oxygen transport into the agglomerate can be divided into three steps. First, once oxygen reaches the surface of the agglomerate, it dissolves into the electrolyte phase. At the gas-electrolyte interface equilibrium is assumed:

$$c_{O2,g/m} = \frac{p_{O2}}{H_{O2,m}} = \frac{RT}{H_{O2,m}} c_{O2}, \qquad \text{(Equation 7.12)}$$

where $H_{O2,m}$ is the Henry's Law constant. After the oxygen has dissolved into the electrolyte, it diffuses through an electrolyte film surrounding the agglomerate. Within the film, the flux of oxygen in the radial direction is given by

$$N_{O2}{}' = D_{O2}^{M} \frac{dc_{O2}}{dr} = D_{O2}^{M} \frac{r_{agg}}{r_{agg} + \delta_{agg}} \frac{c_{O2,g/m} - c_{O2,m/s}}{\delta_{agg}}. \qquad \text{(Equation 7.13)}$$

Finally, oxygen diffuses into the agglomerate and reacts on the surface of Pt catalyst. Assuming the reaction of oxygen is first order, inside the agglomerate, we have:

$$D_{O2,eff}^{agg}\frac{1}{r^2}\frac{d}{dr}\left(r^2\frac{dc_{O2}}{dr}\right)=-k_C c_{O2}. \qquad \text{(Equation 7.14)}$$

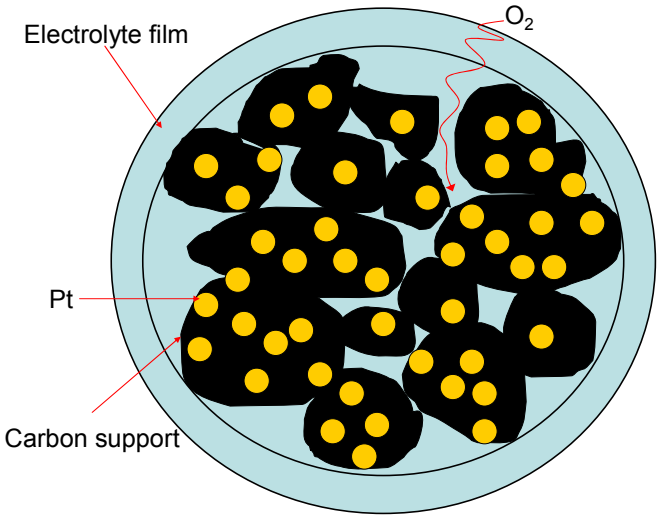

Figure 7.2 Catalyst agglomerate Model.

The effective diffusion coefficient inside the agglomerate is given by Bruggemann's relation [104]:

$$D_{O2,eff}^{agg}=D_{O2,m}\varepsilon_{agg}^{1.5}. \qquad \text{(Equation 7.15)}$$

H_2O_2 diffusion in the membrane and electrodes is different from O_2 for the following two reasons: first, within the ionomer H_2O_2 is primarily transported in the water channels and cannot diffuse through the polymer phase; second, the high saturation pressure of H_2O_2 in ionomer results in only minor vapor concentrations. Therefore, most of H_2O_2 diffuses through the water channels of the ionomer, whereas most of the O_2 diffuses through gas pores.

As well as accounting for mass transporting behavior, we treat both the generation and decomposition of H_2O_2 inside the agglomerate:

$$D_{H2O2,eff}^{agg} \frac{1}{r^2} \frac{d}{dr}\left(r^2 \frac{dc_{H2O2}}{dr} \right) = -k_{C,H2O2}^{Anode} c_{H2O2} + k_C c_{O2}. \quad \text{(Equation 7.16)}$$

In summary, the five major assumptions in this model are: (1) it is a one-dimensional model since the membrane and catalyst layer thicknesses are both much thinner than MEA in-plane dimensions (5 cm × 5 cm), although we use the convection and diffusion in gas channel as a boundary condition. Also, uniformity along the gas channel is assumed. (2) Phase separation model of proton-conducting ionomer electrolyte (such as Nafion®) is assumed, which basically contains a polymer (crystalline) domain and a hydrophilic domain filled, which encompasses water channels [105]. Therefore, in a further assumption, the gases such as O_2 can freely diffuse in both polymer and water phases; whereas H_2O_2 and water only diffuse through water channels in the electrolyte. (3) Under open-circuit voltage (OCV) conditions, due to high potential at cathode, we assume H_2O_2 is only formed at the anode and diffuses to the cathode through the membrane. (4) Only electrochemical reduction of H_2O_2 on Pt catalyst is considered here since it was reported that H_2O_2 decomposition catalyzed by Pt can be treated as two separated electrochemical reactions [106]. Also the electrochemical reduction of H_2O_2 can be much faster than catalytic decomposition. (5) Catalyst agglomerates are assumed to be uniformly distributed inside catalyst layer, and their sizes are the same. Although they are considered to be separated from each other, protons and electrons can still be transferred between these agglomerates. More details of this model can be found in the appendix.

7.2 Experimental validation

In order to validate the proposed model, the above governing differential equations with the appropriate boundary conditions are solved with Matlab to simulate the concentration of H_2O_2.

Figure 7.3 compares the average concentration of H_2O_2 in the membrane with simulation results at different levels of humidity. The modeling result roughly agrees with the experimental data when the gases are fully humidified. The trends in peroxide concentration with humidity are in the same direction, but the errors increase as the humidity is lowered. The positive error may be caused by the impurities in the membrane that could also oxidize I^- to form I_3^-. Although none was evident with an unused membrane, these can be generated during operation. At the same time, since the water content under low humidity is small, and the effective diffusion coefficient of metal contaminants is decreased, these impurities could be trapped in the membrane and accumulated to a high amount. For example, the Fe^{3+} generated from Fenton's reaction in the membrane is a strong oxidant, and possibly some peroxy radical intermediate is formed during membrane degradation as well. Also, some of the catalyst structural parameters that were assumed in the model may be not accurate. Finally, the experimental technique may have some systematic errors as mentioned in the earlier report [37]. The shape of the curve shows a larger slope at high humidity for the simulations, and a transition point occurs at about RH = 70%. This change in slope is largely determined by the shape of water-sorption isotherm of ionomer membrane [74]. The water content increases quickly above 70% RH; however, the decrease in H_2O_2

concentration in water is not that significant, which greatly enhances the total amount of H_2O_2 in water.

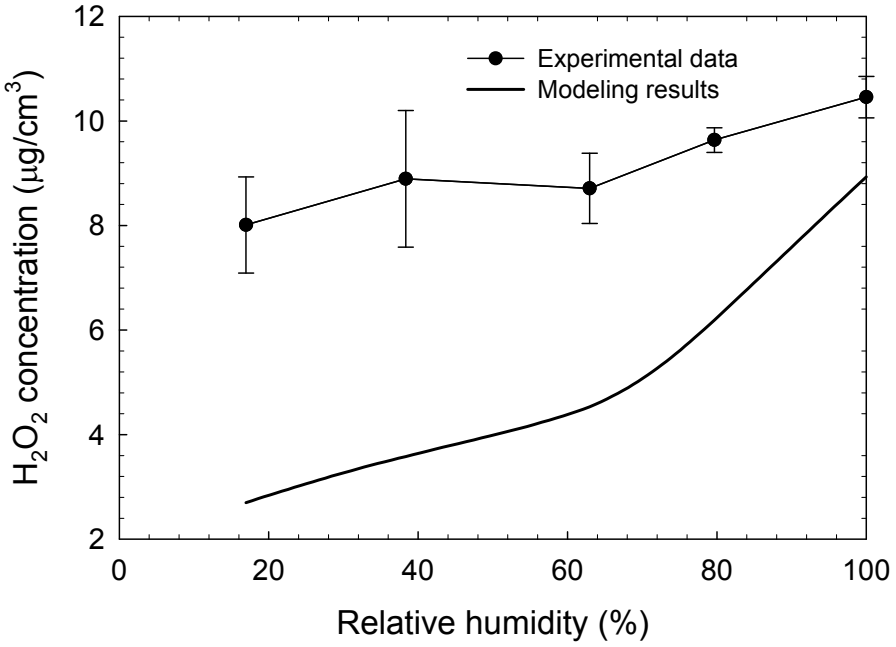

Figure 7.3. Comparison between experimental and simulated H_2O_2 concentrations under different relative humidities.

Operating conditions: H_2 // O_2, T_{cell} = 65 ^oC, Ambient Pressure.

These ionomers phase separate into a hydrophobic Teflon like phase and another with water channels and ionic clusters. The H_2O_2 concentration in Figure 3 is based on the combined volume of both phases. Since peroxide is confined to the hydrophilic phase, it is more appropriate to focus on the concentration in that single phase. When the concentration is converted to a water basis, it can increase significantly under low humidity, and the details will be discussed in Figure 7.8.

Figure 7.4 shows the comparison between experimental and simulated H_2O_2 concentrations under fully humidified conditions with different membrane thicknesses. We used thicker membrane here because at least three Nafion® membranes were needed to determine H_2O_2 concentration in membrane as described in the experimental procedure [37]. The simulation results are consistent with experimental data with respect to both value and trend. It can be noticed that the simulated result becomes higher than the experimental data with thicker membranes.

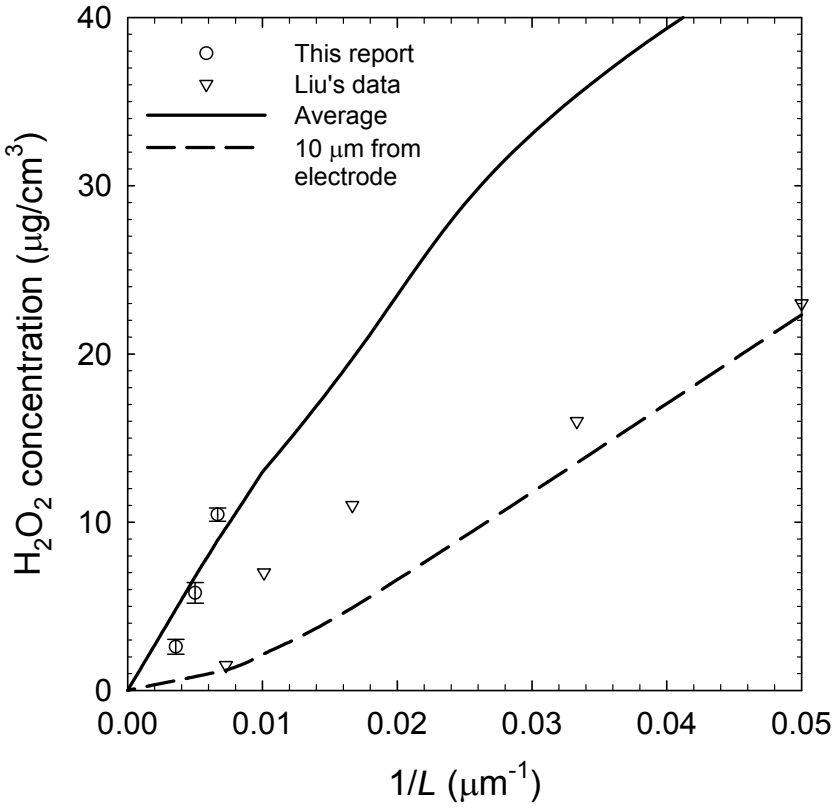

Figure 7.4. Comparison between experimental and simulated H_2O_2 concentrations with different membrane thickness.

One way to decrease membrane resistance is to make it thinner thereby enhancing fuel-cell performance; however, a drawback of using a thin membrane is the concomitant increase in oxygen permeation. Therefore, care must be taken here when using thin membranes, particularly below 50 μm. Since thinner membranes contain less material, the increased loss of fluoride ion and other degradation products can shorten membrane lifetime more significantly than with thick membranes. Also, thinner membranes have relatively weaker mechanical properties, which may result in faster mechanical degradation and accelerate chemical degradation as well.

At the same time, we calculated the H_2O_2 concentrations based on the experimental conditions described in the paper by Liu et al. [36], which are also shown in Figure 7.4. Compared with the H_2O_2 concentration data measured in their paper (Figure 16), it can be seen that the simulation results are of the same order of magnitude, especially at starting and ending points. Different from the average H_2O_2 concentration (solid line), the local H_2O_2 concentration 10 μm from cathode (dashed line) is also plotted, which corresponds to where the Pt microelectrode probe was located in their experiments.

In chapter 6, the H_2O_2 emission from anode only cell was studied under various humidities because it's more simple and reliable than the determination of H_2O_2 concentration in fuel-cell membrane. Figure 7.5 shows the comparison between modeling results and experimental data of H_2O_2 emission rate from an anode only cell. The simulation shows good agreement with the H_2O_2 emission data from experiment. Further, the H_2O_2 emission rate from anode only cell was determined to be 0.01 μmol h^{-1} cm^{-2}

under cell temperature 90 ^{o}C and RH 90 % by Mittal et al. [47], which has the same order of magnitude as our modeling result 0.0218 μmol h^{-1} cm^{-2}.

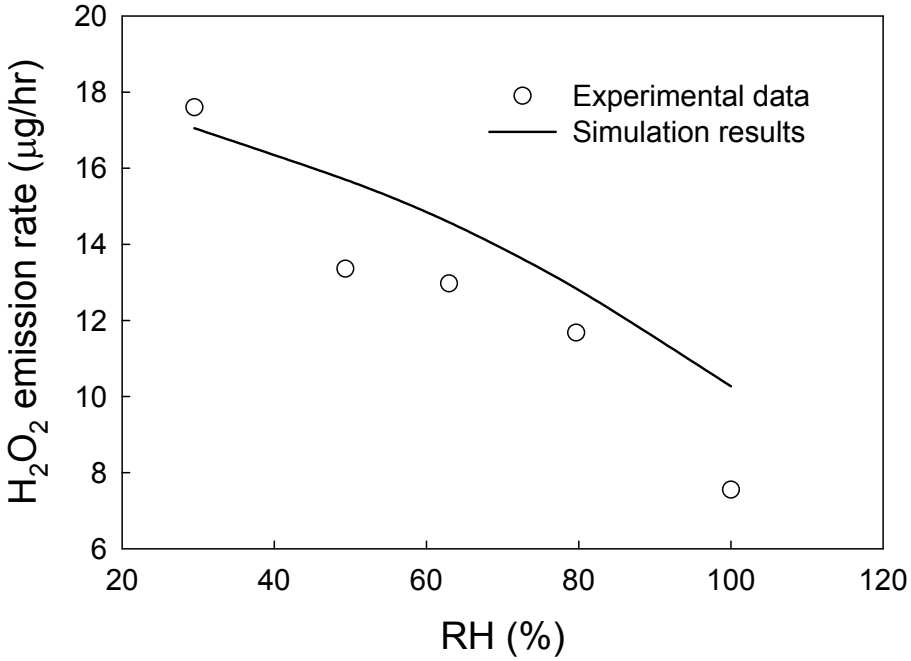

Figure 7.5. Comparison between experimental and simulated H_2O_2 emission rate from an anode only cell.

From the above comparisons, this model shows reasonable agreement with both localized and average H_2O_2 concentrations and is proved to be reliable and accurate both physically and mechanistically; therefore, further parameter studies based on this H_2O_2 formation model will be carried out in the following sections.

7.3 Parameter studies

Since the experimental determination of H_2O_2 concentration has so many limitations and some experimental parameters such as membrane and electrode properties are difficult to vary or maintain, parametric studies by simulation can guide better experimental designs and provide a deeper understanding of H_2O_2 formation mechanism by revealing the most important factors. The base-case conditions and physical properties for the simulation are specified in Table 7.1.

Table 7.1 Base-case conditions and physical properties

Parameters	Value	Denotation
K	7.375 M^{-1} s^{-1}	Pre-exponential factor of Fenton's reaction
E_a	39.5 kJ mol^{-1}	Activation energy of Fenton's reaction
$[Fe^{2+}]$	0.02 mg L^{-1}	Ferrous ion concentration in membrane
L_0	50 μm	Dry Membrane thickness
L_1	10 μm	Catalyst layer thickness
L_2	190 μm	Gas diffusion layer thickness
i_{O2}	1×10^{-1} A m^{-2}	Exchange current density of two-electron ORR
i_{H2O2}	1×10^{-13} A m^{-2}	Exchange current density of H_2O_2 reduction reaction
R	8.314 J K^{-1} mol^{-1}	Gas constant
F	96485 C mol^{-1}	Faraday constant
T	338.15 K	Fuel cell operation temperature
T_{ref}	298.15 K	Reference temperature
Ac	50 m^2 g^{-1}	Catalyst surface active area
c_{H+}	1 M	Proton concentration in ionomer

K_{eq}	70 m^3 mol^{-1}	The equilibrium constant of H_2 adsorption on Pt
r_{agg}	1 μm	Agglomerate size
δ_{agg}	80 nm	Film thickness
ε_{CL}	0.3	Porosity of catalyst layer
ε_{GDL}	0.5	Porosity of gas diffusion layer
α_{O2}	1	Cathodic transfer coefficient of two-electron ORR
α_{H2O2}	0.32	Cathodic transfer coefficient of H_2O_2 reduction reaction

7.3.1 O_2 and H_2O_2 concentration profile over whole MEA

Figure 7.6 shows the oxygen and hydrogen peroxide concentration profile across the MEA. Uniform membrane properties were assumed here. No reaction of oxygen occurs in the membrane so the oxygen concentration is linear across the membrane. Since the oxygen reduction rate is fast compared to the rate of diffusion in the anode, the oxygen concentration profile is mainly determined by its permeability in the membrane. Although the low potential at the anode could substantially increase the rate of oxygen reduction, oxygen diffusion into the agglomerate becomes the main barrier here, which results in extremely low effectiveness factor (~ $5x10^{-5}$). Since one of the assumptions in this model is that H_2O_2 is only generated at the anode, the concentration of H_2O_2 decreases quickly from anode side to cathode side in this figure. The high potential at the cathode completely oxidizes H_2O_2. At the anode, the concentration of H_2O_2 increases from the membrane-electrode interface, whereas the flux of H_2O_2 decreases because of the fast H_2O_2 reduction reaction to form water. In the membrane, H_2O_2 concentration is nearly linear with thickness because the metal ion concentration is low in this simulation.

H_2O_2 diffuses through the membrane without being consumed significantly via Fenton's reaction. However, if the metal ion concentration is increased, the H_2O_2 concentration profile will decrease and become nonlinear, especially under low humidity conditions, and membrane degradation will be much faster. Since the concentration profile of H_2O_2 in the membrane is all but linear with thickness, in the following discussions of this paper, the average H_2O_2 concentration in the membrane was used to represent the profile.

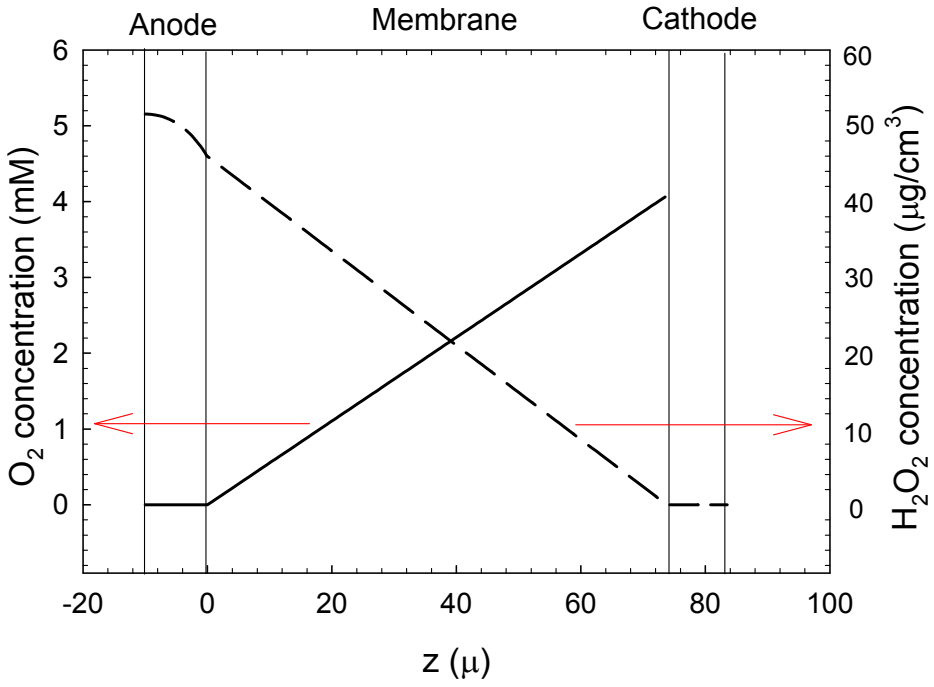

Figure 7.6. O_2 and H_2O_2 concentration profile over the whole MEA.

Operating conditions: H_2 // O_2, T_{cell} = 65 ^oC, RH = 100%, OCV, Ambient Pressure.

7.3.2 Effect of humidity on H_2O_2 concentration

Figure 7.7 shows the average H_2O_2 concentration inside the membrane under different levels of humidity. Since most proton exchange membranes have phase

separation structures, H_2O_2 can be dissolved in the water and transported through the water channels. H_2O_2 concentration based on the water present gives a more relevant concentration level with respect to membrane degradation. Clearly, the concentration of H_2O_2 in water increases at low humidity (dashed line, right ordinate). More free radicals are expected to be generated, and membrane degradation accelerated. Two reasons are proposed for the H_2O_2 concentration increase at low humidity: the water content decreases in the membrane and reactant gas partial pressure increases if the total pressure is held constant. For example, the saturated water partial pressure in the gas phase is 25 kPa at 65 °C [91], which makes H_2 and O_2 partial pressure of 75 kPa under this condition. However, the water partial pressure under 30 % RH is only 7.37 kPa at the same temperature, and it raises the H_2 and O_2 partial pressure to 93 kPa. The increase in gas partial pressure leads to higher gas crossover and accelerates H_2O_2 formation. Also, the total H_2O_2 content in membrane under different humidities is compared here by H_2O_2 concentration based on dry membrane. For example, the density of dry Nafion® is about 2 g/cm^3, whereas the water density is 1 g/cm^3. Using λ to represent the ratio between water and sulfonic groups in Nafion® and assuming the equivalent weight (EW) of Nafion® is 1100 g/mol, the wet membrane volume can be corrected as:

$$\frac{V}{V_0} = \frac{V_0 + V_{water}}{V_0} = 1 + \frac{18\lambda / 1}{1100 / 2} = 1 + 0.0336\lambda \qquad \text{(Equation 7.17)}$$

Based on the above formula, H_2O_2 concentration based on dry membrane can be easily calculated from its concentration in water. The H_2O_2 concentrations in the sections that follow are all based on dry membrane since the water remains the same under constant relative humidity. It is interesting that an increase in H_2O_2 concentration with relative humidity can be seen from the figure. It may be due to the dramatic increase of

water volume in membrane under high relative humidity. Therefore, the total membrane degradation rate (for example, fluoride ion emission rate) can be more complicated under different relative humidity. Although low humidity increases H_2O_2 concentration, the reaction volume is also becoming smaller due to less water in membrane. The final degradation rate will be dependent on both H_2O_2 concentration and membrane volume. In this simulation, since O_2 permeation coefficient doesn't change significantly with humidity [107], we neglect the effect of humidity on O_2 permeation here. However, this effect has to be included into future H_2O_2 formation model with more reliable experimental findings.

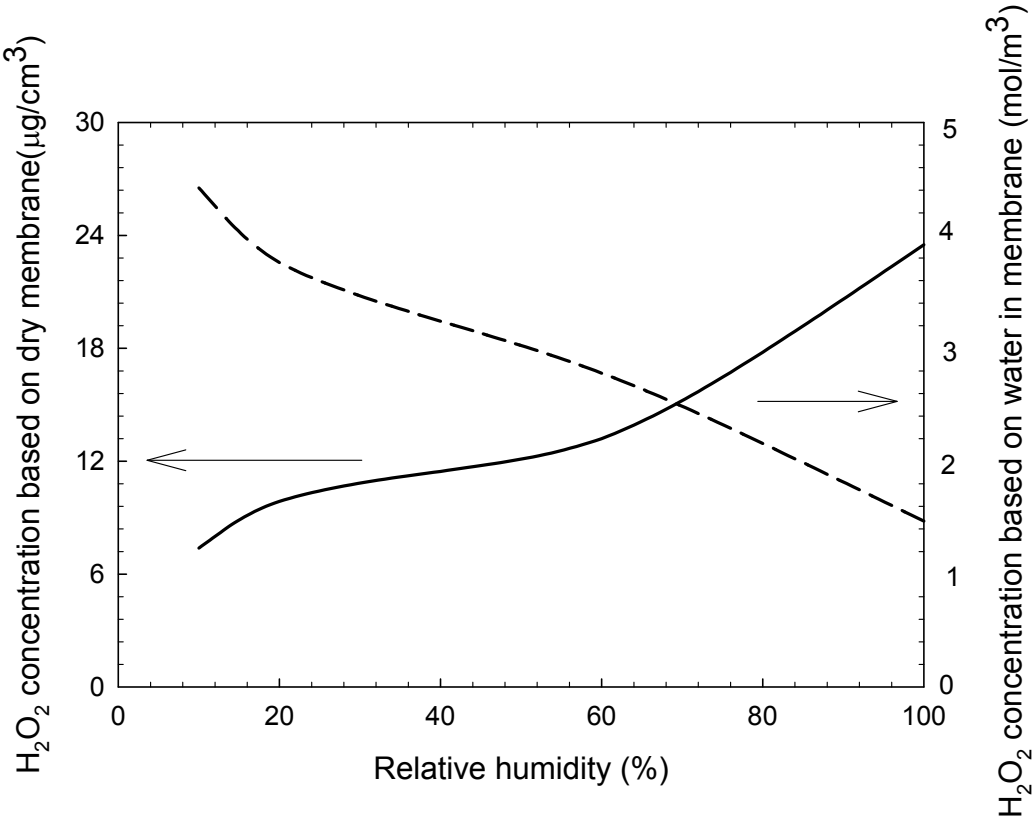

Figure 7.7. H_2O_2 concentrations under different relative humidities.

Operating conditions: H_2 // O_2, T_{cell} = 65 ^oC, OCV, Ambient Pressure.

7.3.3 Effect of temperature on H_2O_2 concentration

Figure 7.8 shows the H_2O_2 concentration inside the fuel-cell membrane under different temperatures with constant relative humidity and water vapor pressure. For the calculation with constant relative humidity, which was fixed as 100 %, the vapor pressure of water increases dramatically with temperature as shown in the inset. Since the total pressure is constant, increasing the water vapor pressure would decrease the oxygen partial pressure thereby reducing the rates of oxygen permeation and H_2O_2 generation. Therefore, two main factors that influence H_2O_2 formation with constant relative humidity under high temperature are the increase of reaction rate and the decrease of oxygen partial pressure. A maximum H_2O_2 concentration between 70 and 80 ^oC can be seen in the figure due to the dual effects of temperature with constant relative humidity. However, the free radical generation rate may also increase with temperature, so the temperature effect on membrane degradation with constant relative humidity is also complicated. Here the activation energy for both two-electron oxygen reduction reaction and H_2O_2 oxidation reaction was assumed to be 38 kJ/mol [108]. If the water vapor pressure is held constant, the concentration of H_2O_2 increases tremendously with temperature because H_2O_2 formation is greatly enhanced under high temperature. Therefore, from this point, we can see high temperature and low humidity could increase H_2O_2 concentration in the membrane and accelerate membrane degradation.

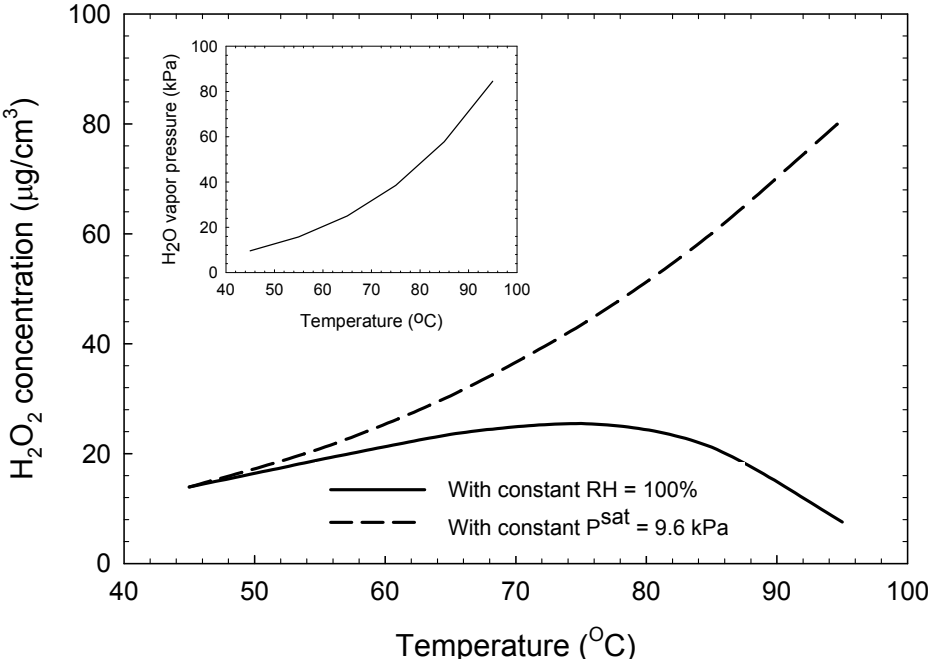

Figure 7.8. H_2O_2 concentrations under different temperatures.

Operating conditions: H_2 // O_2, OCV, Ambient Pressure.

7.3.4 Effect of oxygen partial pressure on H_2O_2 concentration

Since the partial pressure of oxygen has a significant impact on the rate of oxygen permeation through membrane, the effect of oxygen partial pressure on H_2O_2 formation was also studied here. The rate of oxygen permeation is directly proportional to its partial pressure at cathode, correspondingly the H_2O_2 concentration also has a linear relationship with oxygen partial pressure. If there's a load on the cell, the partial pressure of oxygen at the cathode could be reduced due to consumption during oxygen reduction reaction. Therefore, a fuel cell held at open-circuit is more susceptible to membrane degradation than one operating under load due to the decrease of oxygen permeation, which has been proved by experimental results [16].

7.3.5 Effect of hydrogen partial pressure on H_2O_2 concentration

According to Equation (6), the hydrogen partial pressure affects the coverage of reactive Pt sites due to the absorption of H_2 on Pt catalyst. Since H_2O_2 is mostly generated at the anode under OCV condition, the coverage of reactive Pt sites there will have significant impact on H_2O_2 formation and decomposition rate. The effect of hydrogen partial pressures on H_2O_2 concentration in the membrane is shown in Figure 7.9. It can be seen that reducing hydrogen partial pressure decreases the H_2O_2 concentration in the membrane, and this effect is enlarged especially in the low pressure region. The reason is that the decrease of reactive Pt sites under high H_2 partial pressure not only increases the decomposition rate of H_2O_2 but also decreases its formation rate by reducing the coverage of Pt-H moieties. This result is well consistent with the fluoride ion emission rate (FER) study by Liu et al. [46], who observed an increase in FER under high H_2 partial pressure.

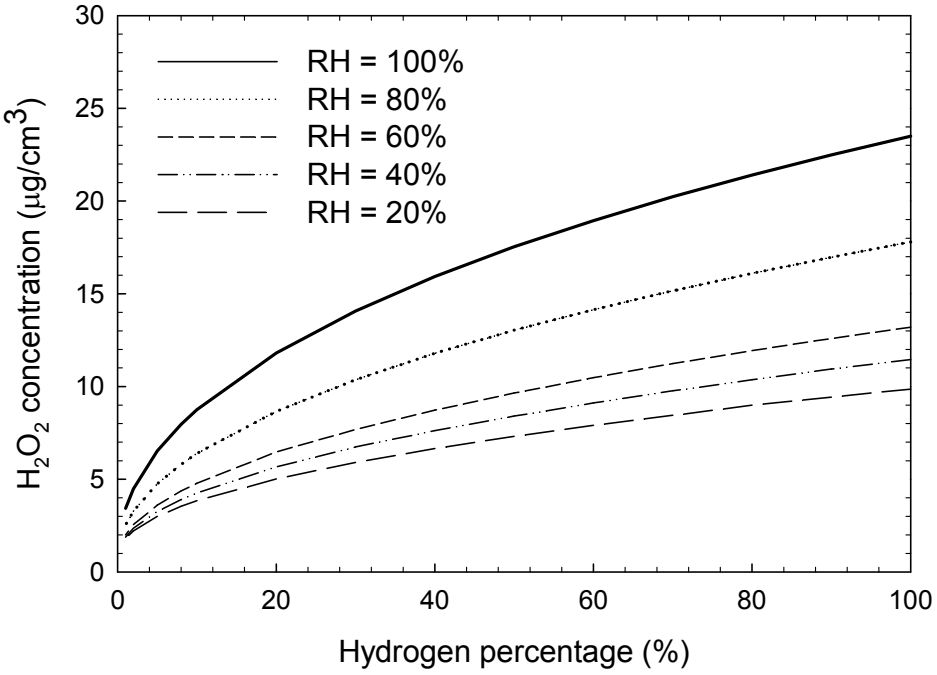

Figure 7.9. H_2O_2 concentrations under different hydrogen partial pressures. Hydrogen percentage is on a dry gas basis

Operating conditions: Cathode O_2, T_{cell} = 65 ^oC, OCV, Ambient Pressure.

7.3.6 Effect of metal contaminant levels on H_2O_2 concentration

In this model, the concentration of H_2O_2 in the membrane was controlled by its diffusion and reaction with metal ions such as Fe^{2+}. Therefore, the level of metal contaminants influences the level of H_2O_2 in the membrane. Here, in order to compare the effect of diffusion and reaction on the concentration of H_2O_2, a dimensionless ratio of reaction to molecular diffusion times is defined as:

$$\xi = \frac{k'[Fe^{2+}]}{D^M_{H2O2,eff}} l_2^{\,2}. \qquad \text{(Equation 7.18)}$$

When $[Fe^{2+}]$ is very small, ξ is also very small and diffusion is dominant in the membrane, therefore, $[Fe^{2+}]$ has a negligible impact on H_2O_2 in this region, As $[Fe^{2+}]$

increases, the reaction becomes dominant inside membrane, so the H_2O_2 concentration drops quickly due to fast decomposition reaction. Especially at low humidity, due to the increase of H_2O_2 concentration and effective diffusivity, the H_2O_2 decomposition reaction can be dominant in the earlier stage. However, increasing [Fe^{2+}] will increase the generation of hydroxyl free radical, which can attack weak groups in the polymer membrane and cause membrane degradation [4]. But this also suggests that a peroxide decomposition additive that doesn't have Fenton activity may be an effective way to reduce H_2O_2 formation in fuel cell [109].

7.3.7 Effect of O_2 diffusivity on H_2O_2 concentration

In the base case, oxygen diffusivity was related with temperature [110] by:

$$D_{O2}^{M} = 0.0438 \exp(-\frac{E_d}{RT}) . \qquad \text{(Equation 7.19)}$$

From the definition of permeation coefficient $P_{O2} = D_{O2} S_{O2}$, oxygen permeation is directly proportional to O_2 diffusivity and solubility in the membrane. The generation of H_2O_2 at anode is mainly determined by O_2 permeation from cathode. At the same time, the O_2 diffusivity also affects the rate of oxygen reduction reaction inside the agglomerate, but this effect is negligible compared to the change in gas permeation under our modeling conditions. Therefore, the H_2O_2 concentration increases linearly with oxygen diffusivity, which indicates that oxygen diffusivity is the most important membrane parameter to control H_2O_2 formation. Therefore, to design a new fuel cell membrane with low oxygen diffusivity and solubility will be the primary effort to enhance membrane durability.

7.3.8 Effect of anode thickness/catalyst loading on H_2O_2 concentration

Under open-circuit conditions, H_2O_2 is generated only at the anode, and the thickness and loading are important electrode parameters. Figure 7.10 shows the H_2O_2 concentration as a function of anode thicknesses for two cases. In the first case, the loading of platinum (mg Pt/cm^2) is held constant, but the thickness of the electrode varies. Whereas the total amount of H_2O_2 generation is unchanged, there is a competition between transport and decomposition of peroxide in the electrode. The thinner the electrode the greater the rate of H_2O_2 transport into the membrane before decomposing inside the anode. The result is an increasing concentration of H_2O_2 with decreasing electrode thickness. In the second case, the loading of platinum is proportional to the electrode thickness. For the same reasons as outlined above, the same trend in H_2O_2 concentration; with thickness is observed. The top abscissa in Figure 9 shows the variation of loading. Furthermore, the influence of thickness is more important in the second case. From the oxygen concentration profile shown in Figure 5, the amount of oxygen escaping from anode is extremely small. Therefore, nearly all the oxygen that permeated from cathode reacts with hydrogen atom to form hydrogen peroxide. In other words, H_2O_2 generation at anode is only dependent on oxygen permeation from cathode, but its decomposition via two-electron reduction reaction can be different. The change of anode thickness and Pt loading will not affect oxygen permeation, so H_2O_2 generation is constant here. However, the increase of Pt loading can greatly enhance the rate of H_2O_2 decomposition in the agglomerate and reduce the total H_2O_2 amount coming out from anode to the membrane. From this point, we can see Pt loading also has noteworthy impact on H_2O_2 concentration: high Pt loading can decrease H_2O_2 generation rate at

anode and reduce its concentration inside membrane. Therefore, care should be taken when reducing the Pt loading at the anode. Although the H_2 oxidation reaction may keep the anode polarization low even with less catalyst, this can reduce membrane durability.

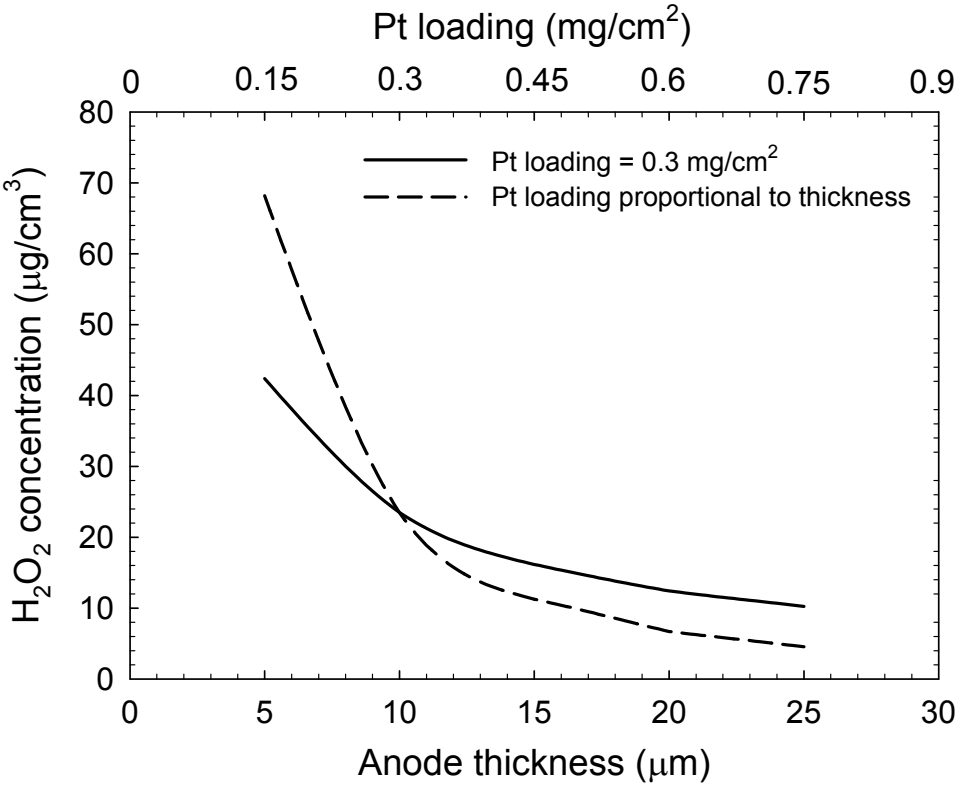

Figure 7.10. H_2O_2 concentrations under different anode thickness.

Operating conditions: H_2 // O_2, T_{cell} = 65 ^oC, RH = 100%, OCV, Ambient Pressure.

7.3.9 Effect of catalyst active area on the H_2O_2 concentration

Figure 7.11 shows the effect of the catalyst electrochemical active area (ECA) on the concentration of H_2O_2 in the membrane. It can be seen that the H_2O_2 concentration increases quickly as the area is reduced. Similar to the effect of Pt loading, low catalyst active area will reduce the H_2O_2 reduction reaction at anode and increase the H_2O_2

concentration in the membrane. As we know, Pt catalyst with high active area could boost four-electron oxygen reduction at cathode. One of the explanations can be that the enhancement of two-electron H_2O_2 reduction reaction, which converts more O_2 to H_2O not H_2O_2. During fuel-cell operation, catalyst active area is lost especially at cathode [20], and this may increase the concentration of H_2O_2 and exacerbate membrane degradation. However, at open-circuit, H_2O_2 is only formed at anode, and catalyst degradation is negligible there. Therefore, the membrane degradation rate is expected to be stable with time [45, 111], and this phenomenon has already been verified by our experiment [26].

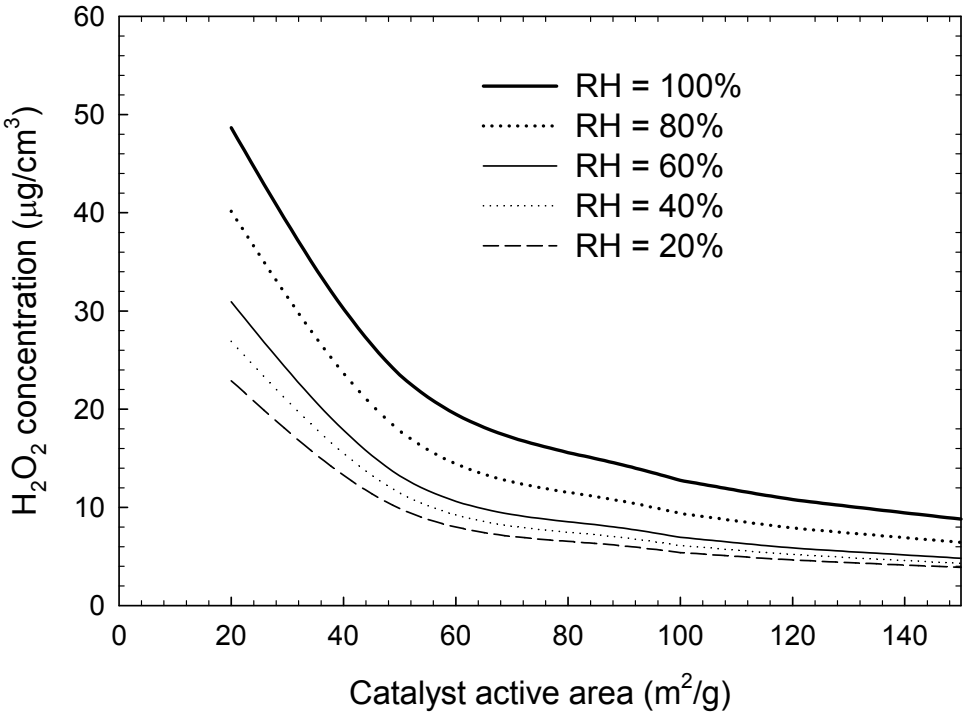

Figure 7.11. H_2O_2 concentrations under different catalyst activity.

Operating conditions: H_2 // O_2, T_{cell} = 65 ^oC, OCV, Ambient Pressure.

7.3.10 Effect of current density on H_2O_2 concentration

All the above results were obtained under open-circuit voltage conditions (zero current), but the electrical load is required for a practical fuel-cell operation such as in a fuel-cell vehicle. Figure 7.12 shows H_2O_2 concentration under different cell potentials that correspond to various current densities depending on the performance of a certain fuel cell. It can be seen that the H_2O_2 concentration remains nearly constant above 0.6 V and increases quickly after further lowering the potential. This is because the two-electron oxygen reduction reaction has a standard potential of 0.695 V, and H_2O_2 starts to form at the cathode below that potential. This result is also consistent with Ramaswamy *et al.'s* RRDE study of H_2O_2 formation, where the rate of peroxide generation increased significantly when the potential was below 0.6 V versus RHE [58]. Since fuel cell is normally operated at 0.6 ~ 0.8 V, the H_2O_2 concentration doesn't increase significantly in that region. However, it has been reported that the membrane degradation rate (FER) is decreasing with the increase of current density [16]. There could be some other reasons reducing the rate of formation of H_2O_2 under high current densities such as consumption of reactant gases, which decreases the gas permeation, flooding problems that block gas transport or the change of H_2O_2 diffusion properties with existence of proton flux in the membrane. Therefore, the effect of current density on H_2O_2 formation is more complicated than open-circuit condition, which needs further experiments to explore more detailed mechanisms.

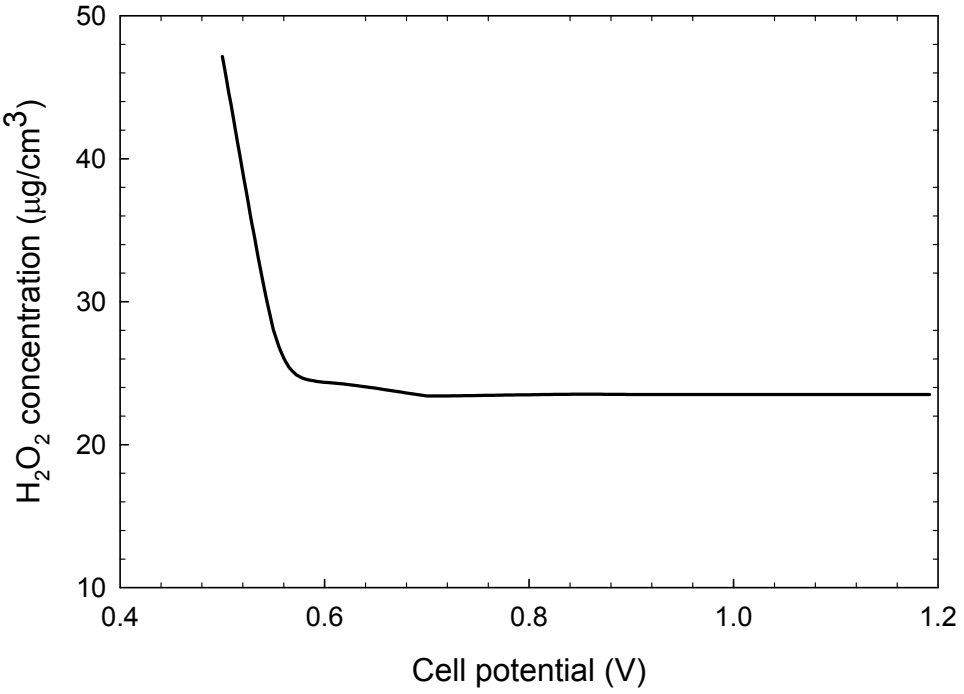

Figure 7.12. H_2O_2 concentrations under different cell potentials.

Operating conditions: H_2 // O_2, T_{cell} = 65 ^oC, RH = 100%, Ambient Pressure.

7.4 Discussions on H_2O_2 mitigation in fuel cell

Since H_2O_2 is an undesired byproduct during fuel-cell operation and may be responsible for membrane degradation, the ultimate goal of this study is to investigate H_2O_2 formation in fuel cell and minimize H_2O_2 concentration in the membrane by optimizing different parameters. The parameters studied in this paper can be classified into three categories: operational conditions such as relative humidity, temperature, oxygen/hydrogen partial pressures and current density; membrane properties such as membrane thickness, metal ion contaminant level, oxygen diffusivity; electrode properties such as electrode thickness and surface active activity.

With respect to operation conditions, oxygen partial pressure is difficult to change since air and pure H_2 will be used as cathode and anode gases respectively for fuel cell vehicle. What we could change probably would be relative humidity and temperature. From the above analysis, high humidity and low temperature can reduce H_2O_2 formation in the membrane, but our target is to operate the fuel cell under low humidity and high temperature to facilitate water and heat management [17]. Therefore, it seems difficult to mitigate H_2O_2 formation solely by adjusting operation conditions.

New membrane development is another option here. Increasing membrane thickness would not be a good idea since we don't want to sacrifice the performance. Decreasing oxygen solubility and diffusivity will be the primary effort to design more durable membrane such as hydrocarbon membrane [112].

Electrode properties are much easier to change than membrane properties so it looks more promising to optimize electrode properties for H_2O_2 mitigation. However, one of the challenges we have here might be how to satisfy all the requirements including catalyst cost, performance and stability. Optimization must be performed to achieve the best catalyst design. But for membrane durability only, the MEA should have thick electrode, high catalyst loading and active area.

CHAPTER 8

THE EFFECT OF HUMIDITY ON THE DEGRADATION OF NAFION® MEMBRANE

In chapter 4, we presented experimental results of membrane degradation in Fenton's test analyzed by FTIR and XPS; however, the difference between the *ex-situ* Fenton's test and *in-situ* fuel-cell tests may limit the application of these results [35]. A direct analysis of Nafion® membrane separated from a MEA is the best way to study degradation mechanisms. Unfortunately, no such systematic and comprehensive analysis has been reported previously, which is in large part because of the difficulty in separating membrane samples from the Pt catalyst. In this chapter, the catalyst was coated on gas diffusion layer (GDL) instead of membrane surface to make it possible to remove the catalyst layers from membrane surface. The objective of this study is to examine the chemical and physical structural change of Nafion® membrane after accelerated fuel-cell tests via different spectroscopic techniques, and thereby provide insight on the effect of humidity on the mechanism of membrane degradation. The emission rates of different degradation products were monitored by collecting vent water during the tests. The membrane conductivities and mechanical properties were measured before and after fuel-cell tests by *ex-situ* high-throughput instruments [59]. The ion exchange capacity of membrane samples was determined by Inductively Coupled Plasma (ICP) Emission Spectrometer. Fourier Transform Infrared Spectroscopy (FTIR) was applied to study both the formation of new groups and the relative abundance of existing groups in the degraded membrane. The thermal stability of degraded membranes was determined by

Thermogravimetric Analysis. The cross section of a degraded MEA sample was imaged with scanning electron microscope (SEM) to investigate the mechanical structure change. Simulation results from a simple degradation model are compared with experimental data. Finally, the effects of humidity on membrane degradation were illustrated by two different degradation schemes.

8.1 Degradation products identification from ion chromatography

Figure 8.1 shows the ion chromatogram of cathode exhaust water collected from durability test 3, the lowest humidity and most aggressive conditions. A sharp and strong peak of fluoride ion can be observed at 3.1 minutes, which corresponds to the major degradation product hydrogen fluoride (HF). Other anions observed in the chromatogram include Cl^- and CO_3^{2-}. Since the content of these two anions are close to the level found in de-ionized water (Cl^- ~ 0.01 PPM, CO_3^{2-} ~ 1 PPM, which matches the calculation from the CO_2 solubility), they can be considered as contaminants. The most interesting peak exists at 9 minutes, which could be attributed to CF_3COO^- from the degradation product TFA. This observation is consistent with an earlier degradation study [57] that used model compounds. The sulfate ion peak at 6.8 minutes is negligible, indicating that the cleavage of C-S bond in Nafion® structure is insignificant during membrane degradation.

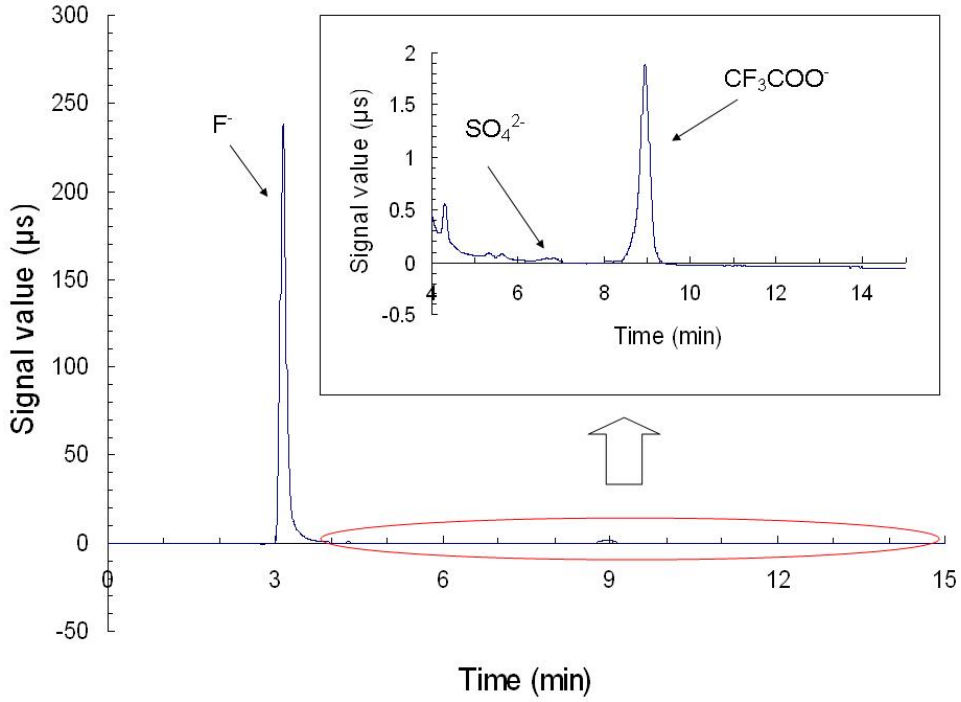

Figure 8.1. Ion chromatogram of cathode water from fuel-cell test.

8.2 Degradation products analysis

Figure 8.2 (a) shows the FERs during three different durability tests under various relative humidities (82 %, 55 % and 36 %) at 90 ^{o}C. A significant increase in the FER under low humidity can be clearly observed from the experiment, especially when the relative humidity is below 50 %. On the other hand, the sulfate ion emission rates in Figure 8.2 (b) show scattered data points, which were close to the impurity level in de-ionized water. The most interesting finding here is that the TFA emission rates in Figure 8.2 (c) show the same trend as fluoride ion with respect to both humidity and time (The TFA concentration from the test with RH = 82 % is not shown here since it's almost below the detection limit.). This suggests that TFA is also an important degradation product and has a strong relation with HF formation. Therefore, the molar ratio between

HF and TFA during each test was compared in Figure 8.2 (d) to investigate this relationship. The data show a higher ratio at RH = 55 % than 36 %, indicating the side chain degradation becomes more and more important under low humidity. Considering the chemical structure of Nafion® membrane, TFA is most likely formed from the side chain where a CF_3 group is attached to an ether linkage. Therefore, the degradation product TFA could be considered as an indicator of side chain degradation, whereas HF emission rates represent the backbone degradation since 90 % of the fluorine exists in the PTFE backbone. Side chain degradation will cause chain scission and generate more vulnerable groups such as –COOH, which could further accelerate membrane degradation [72]. This conclusion is consistent with the experimental data where a simultaneous increase of both HF and TFA emission was observed, whilst the concentration of sulfate ion is negligible.

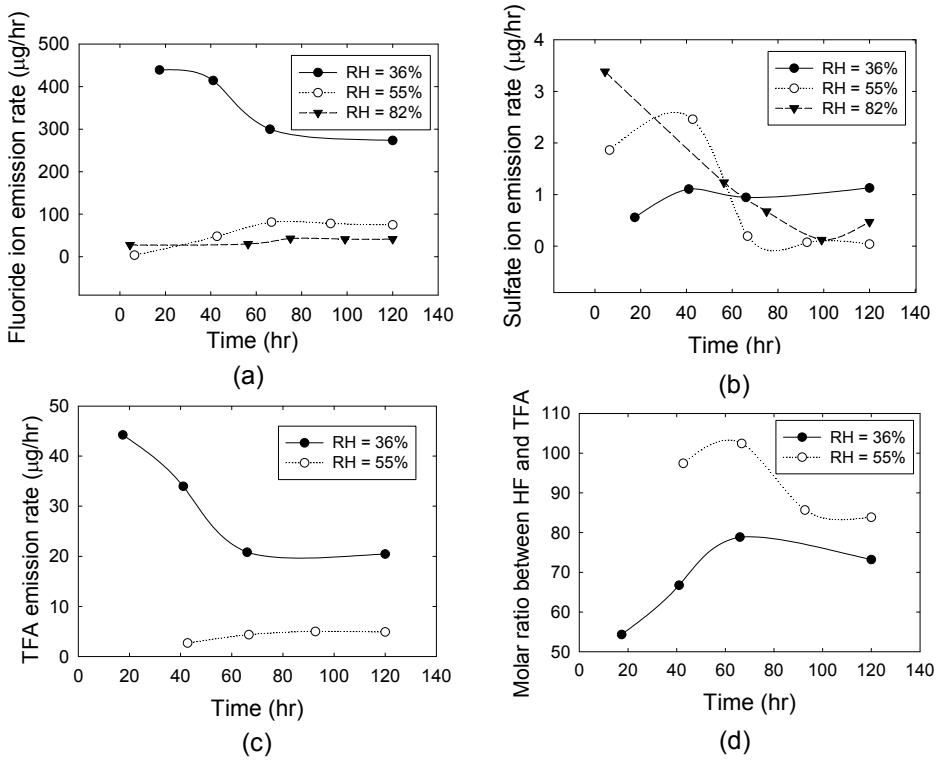

Figure 8.2. Fluoride ion emission rate (a); sulfate ion emission rate (b); TFA emission rate (c); Molar ratio between HF and TFA (d) under various relative humidities. Operating conditions: H_2 // O_2, T_{cell} = 90 ^oC, OCV, Ambient Pressure.

8.3 Conductivity, IEC and mechanical tests

Figure 8.3 shows the decrease in conductivity of Nafion® membranes after durability tests, which is a major factor in the associated performance decay. The possible reasons that could contribute to the decrease of conductivity are: loss of sulfonic acid groups, and replacement of proton due to contamination or S-O-S cross-linking that is found in the following FTIR spectra. The conductivities were also measured after treatment with 0.5 M sulfuric acid at 80 ^oC for 1 hr to remove any metal contaminants. Treatment with sulfuric acid increased the conductivity of the degraded samples by about 50 %, close to the values of virgin Nafion®, indicating that the replacement of protons might be the main reason for conductivity decrease. This makes sense because the degradation mode of backbone unzipping will decompose the polymer chain as the whole repeat unit. Although sulfonic acid groups were lost as well, the decrease in membrane thickness was directly proportional to the loss, and this is further supported by the following FTIR spectra and SEM images. However, the conductivity of the sample tested at RH = 36 % still shows about a 10 % drop compared to virgin Nafion® even after treatment. This is mainly ascribed to the loss of sulfonic acid groups from a side chain scission process, which would decrease membrane conductivity.

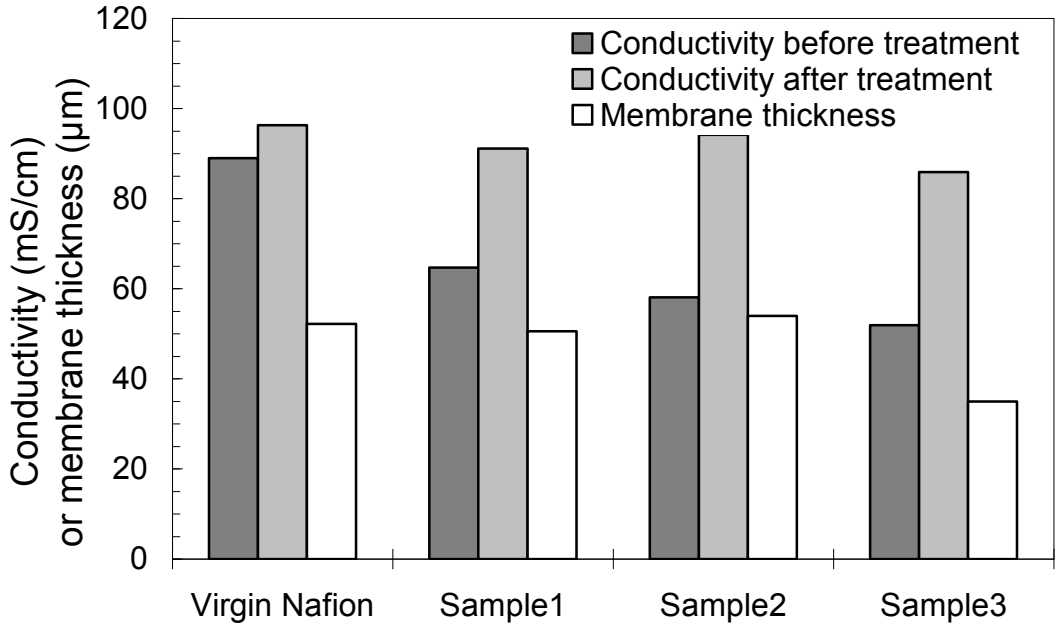

Figure 8.3. The electrical conductivity of degraded membrane before and after treatment with sulfuric acid.

In order to further distinguish the effects between cation contamination and S-O-S cross-linking, the membrane samples were completely ion-exchanged by soaking in 0.1 N KOH solution at room temperature for 24 hrs and analyzed by XPS (X-ray Photoelectron Spectroscopy). The atomic ratio between potassium and sulfur was calculated by integrating the area under the K 2s (Binding Energy = 398 EV) and S 2p (Binding Energy = 166 EV) peaks. The results are listed in Table 1. For samples tested under the conditions of higher humidity (82 % and 55 %), the ratios between potassium and sulfur are close to one, indicating almost all of the protons in the sulfonic acid groups were exchanged to the K^+ form. Therefore, the decrease of conductivities in these two samples may be mainly attributed to contamination by other cations. However, the ratio

dropped to 0.73 for the sample at RH = 36 %, which may be mainly due to the S-O-S cross-linking resulting in reduction of the available ion exchange sites and further the decrease in membrane conductivity.

Table 8.1 XPS results and mechanical properties of membrane samples.

Humidity of gases	K:S	IEC (meq/g)	Max Force (N)	Young's Modulus (MPa)	Ultimate Tensile Strength (MPa)	Breaking Strength (MPa)
Nafion® (as received)	1	0.96	6.8	89.5	16.9	4.69
82 %	1.08	0.99	5.7	109.4	14.7	3.94
55 %	0.97	0.98	5.5	122.7	13.9	3.68
36 %	0.73	0.88	0.88	113.8	8.3	0.63

Table 8.1 also shows the ion exchange capacity (IEC) of membrane samples after fuel-cell tests. It can be seen that IEC remains constant for the samples under the conditions of higher humidity (82 % and 55 %) compared to virgin Nafion®, which is consistent with the TER data (a total of 1.8 % loss of side groups for sample at RH = 55 %). In contrast, for the sample tested at RH = 36 % a loss of 8.3 % in IEC was observed, mainly due to membrane degradation especially the side chain degradation. This value also fits well with the 13.4 % loss in sulfonic acid groups calculated from TFA emission and a 10 % drop in membrane conductivity after treatment, providing strong evidence of side chain degradation.

The mechanical properties of degraded membrane samples were evaluated using HTMECH testing system [60] and are listed in Table 8.1. A significant decrease in mechanical properties can be observed due to polymer loss from chemical degradation in the sample tested at RH = 36 %, which is the most brittle sample. The maximum force, ultimate tensile strength, and breaking strength decreased with humidity, showing the strong relation between chemical and mechanical degradation. The Young's modulus, which is the initial slope of the stress strain curves, was also determined. Young's modulus is a property that is measured for small deformations, i.e., in the elastic regime. Membrane samples after durability tests resulted in an increase of Young's modulus, suggesting the decrease of ductility due to membrane degradation.

8.4 FTIR studies after degradation

In order to investigate the formation of new groups and the relative abundance of existing groups, ATR-FTIR was applied here to study membrane chemical structure change after durability tests. Compared with FTIR under transmission mode, the water absorption is suppressed, and the characteristic bands in the region between 1400 and 1000 cm^{-1} are well separated due to the low signal intensity collected under the ATR mode. Figure 8.4 shows the ATR-FTIR spectra of degraded membranes. The spectra under different humidities are very similar with respect to both shapes and peak positions, suggesting minimal changes in the polymer structure during degradation. However, after enlarging the high wave number region, a small peak around 2900 cm^{-1} emerges for the membrane tested under conditions of low humidity. This peak is attributed to the OH group in the –COOH structure [113]. The amount of this group in the degraded

membrane is low, which can be explained by fast backbone unzipping and a relatively slow side chain scission process. The evolution of S-O-S was observed at 1450 cm^{-1}, which contributes to the decline in conductivity and further evolves to –COOH group and accelerates degradation [27, 34, 114].

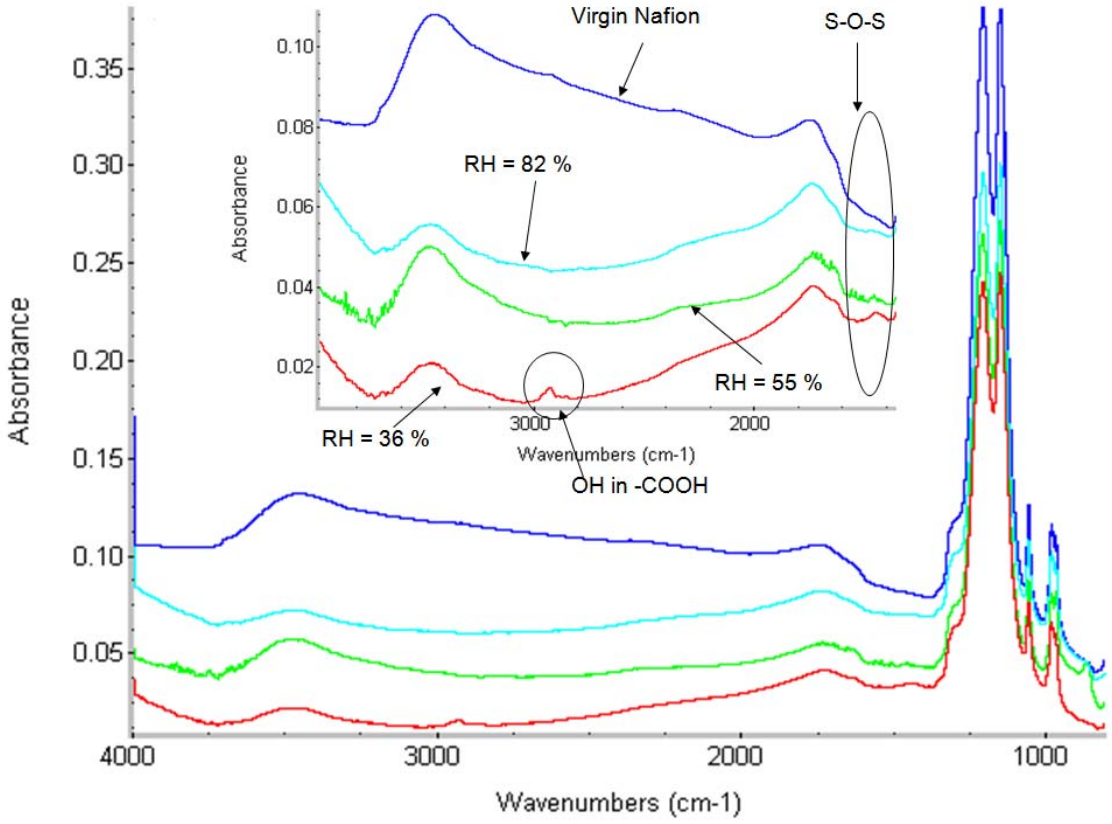

Figure 8.4. ATR-FTIR spectra of degraded membranes.

What's more, the relative abundance of chemical groups can be quantified from the areas of the absorption peaks. The ratio between these areas can reflect changes in the chemical structure of degraded membranes. Since some of the peaks overlapped in the spectra, the curve fitting function of OPUS software (Bruker Optics) was used to

integrate each peak separately. The assignments of different bands in Figure 8.5 were consistent with the observation by Ramasewamy *et al.* [58] For example, the two bands at 984 and 969 cm^{-1} can be attributed to two ether linkages (-C-O-C-) in Nafion® membrane. The high frequency band (at 984 cm^{-1}) can be assigned to the ether linkage directly connected to the carbon backbone (C-O-C (B)), whereas the other low frequency band (at 969 cm^{-1}) is attributed to the ether linkage in the middle of side chain (C-O-C (A)) [115].

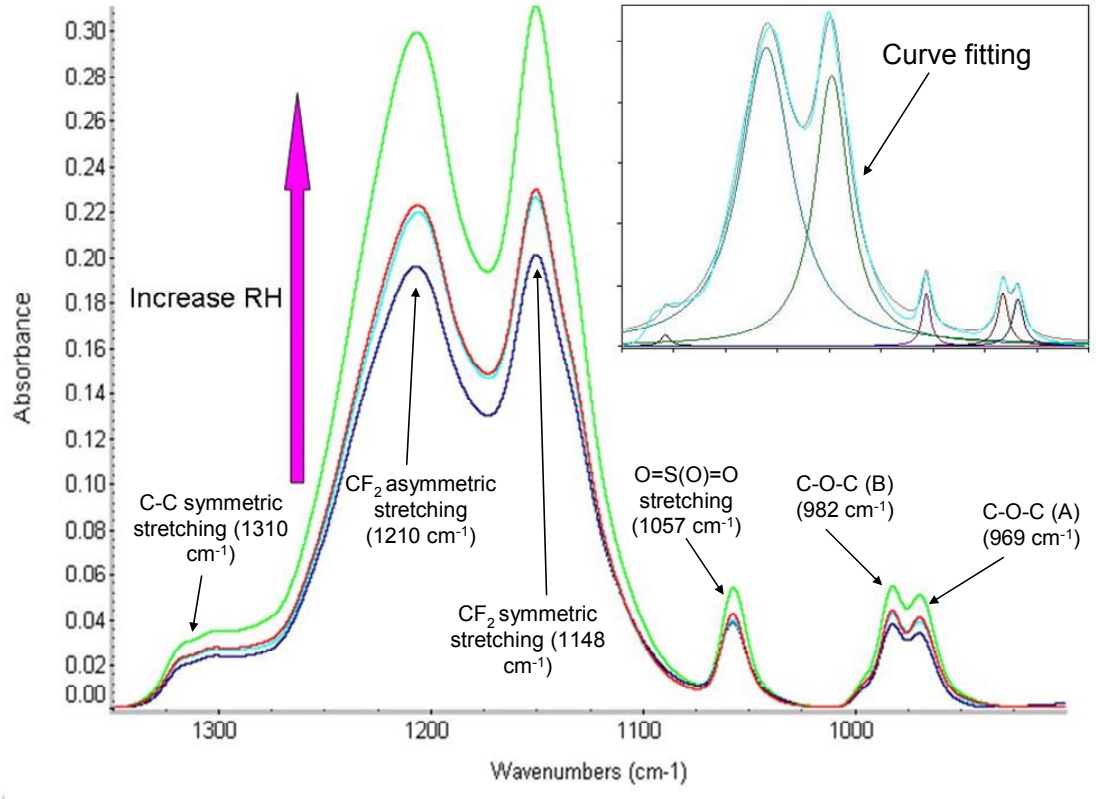

Figure 8.5. ATR-FTIR spectra of degraded membranes in 1350 cm^{-1} ~ 900 cm^{-1} short range.

It can be seen in Figure 8.5 that the areas of almost all groups decrease with humidity, which further confirms that the membrane degradation is accelerated under low humidities. The change in chemical structure can be studied by comparing the ratio between different groups as shown in Figure 8.6. The ratio between C-O-C (A) and C-O-C (B) groups, which is one given the assumed structure shown earlier, stays nearly constant in samples under the conditions of higher humidity (82 % and 55 %), indicating insignificant side chain decomposition. This observation is consistent with the TFA emission data – only about 1.8 % side chain loss if one TFA is counted as one C-O-C (A) structure. For the sample tested at the lowest humidity, the ratio decreases, showing that the C-O-C (A) group is decomposed from the 13.4 % loss of side chains as determined by TFA emissions, and similar observations were also reported using a cathode-side degradation test [58]. It is interesting to note the increase in the ratio between SO_3 and C-F groups in the same sample as well. From calculations, the total fluorine loss is about 26.4 % in the durability test at the lowest humidity, approximately twice that of side chain loss, which agrees with the ratio increase. Currently two mechanisms are proposed to explain membrane degradation under fuel-cell conditions: main chain unzipping [4] and chain scission from the side group [116]. Generally speaking, main chain unzipping starts from a weak end group (such as -COOH) and continues along the main chain. The net effect is that the entire repeat unit structure (n) is lost. Therefore, the ratio between SO_3 and C-F group remains constant in this degradation scheme. Although, chain scission from the side group could create two –COOH end groups from the ether linkage between side chain and backbone and increase the ratio. Therefore, the degradation from chain

scission should be the dominant mechanism of degradation that is accelerated under conditions of low humidity.

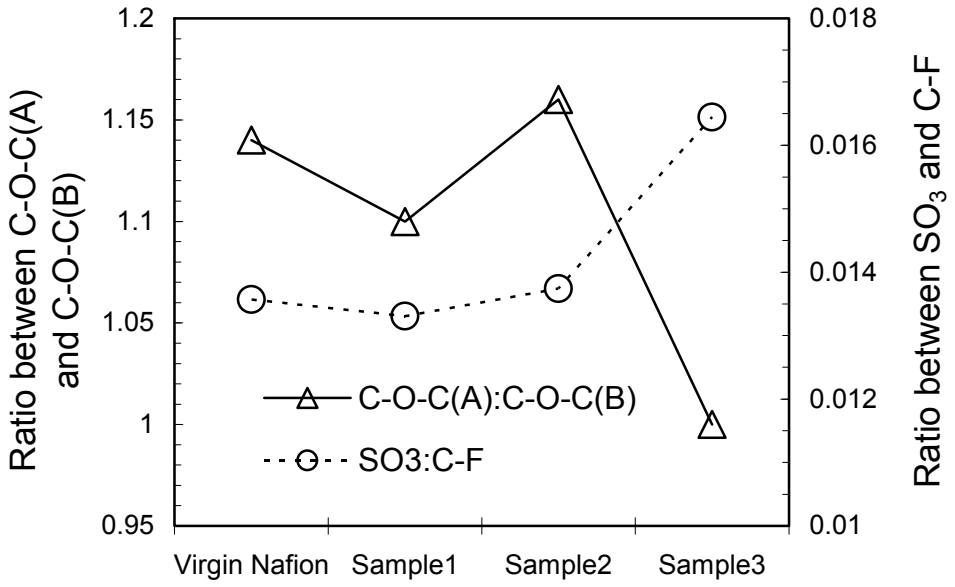

Figure 8.6. Relative abundance of functional groups obtained from curve fitting.

8.5 TGA studies of degraded membrane

The thermal stability of degraded Nafion® membrane was analyzed by TGA and is shown in Figure 8.7. As expected, the degraded membranes from high humidity show very similar TGA profile as virgin Nafion® membrane, which again confirms that no significant structural change occurred during degradation. In contrast, the sample from the lowest humidity test shows poor thermal stability and starts to decompose under relatively low temperature (less than 200 ^{o}C). When plotting derivative thermogravimetric analysis (DTA) results for each sample, a new peak is observed in the sample tested under RH = 36 %, indicating the formation of new moieties during

degradation. The TGA results are also listed in Table 2. The initial weight loss of Nafion® is the loss of water molecules that were combined with sulfonic acid groups. A decrease of equilibrium water content in the same sample is seen, which is consistent with the loss of conductive groups in membrane. Moreover, the lower the humidity the lower the maxima temperature of the first stage, showing the decrease of thermal stability after fuel cell testing.

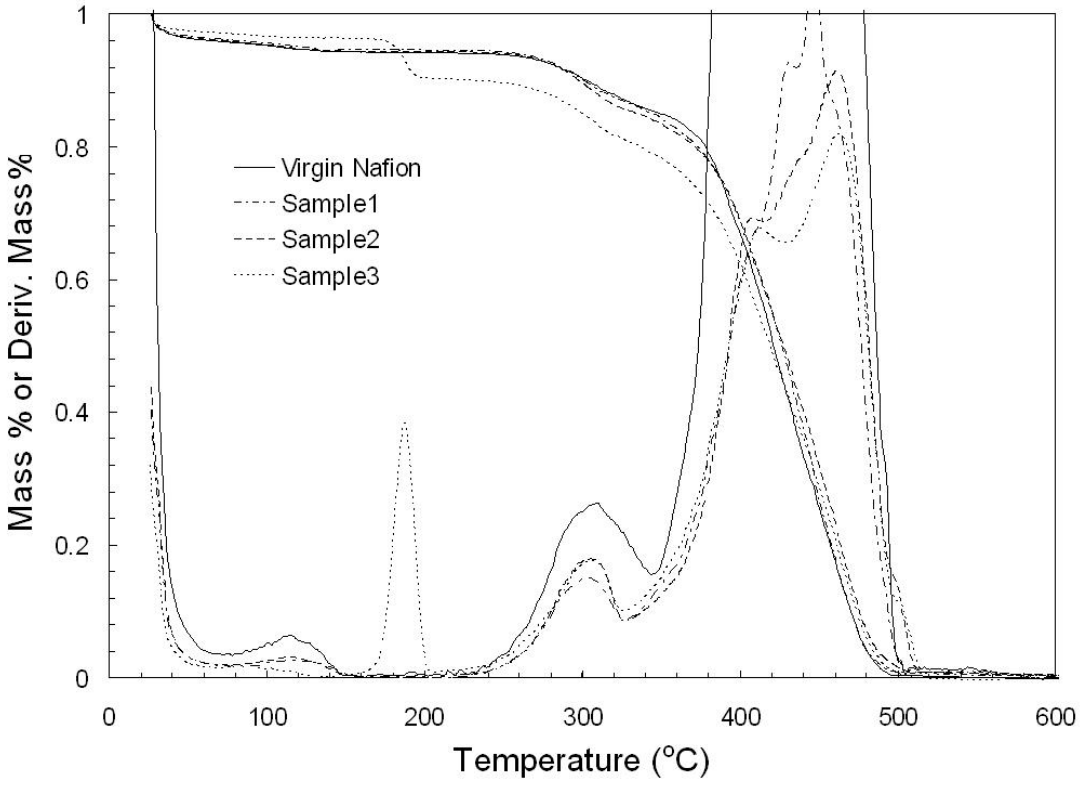

Figure 8.7. TGA and DTA curves of degraded membranes.

TGA conditions: scan rate 2 ^{o}C min^{-1}, resolution 1, nitrogen atmosphere.

8.6 SEM studies of degraded membrane

The cross sections of the degraded MEAs were observed with SEM (Figures 8.8 and 8.9). In Figure 8.8, without resin preparation, the SEM images of both samples from the higher humidity (82 % and 55 %) tests look very flat and defect-free. Some pinholes and delaminations were observed in the sample tested at RH = 36 % and most of them were concentrated near the anode side and close to the center. This observation is consistent with the result reported by LaConti *et al.* [117] They compared the location of blisters from a PEMELC (proton exchange membrane water electrolyzer) and a PEMFC and found that the defects were located at the center of membrane in both cases when there was no net electrochemical transfer of water, such as during OCV conditions. A closer look at a pinhole is shown in Figure 8.8 (d), and the size is measured to be around 400 nm. After resin preparation and surface polishing, the MEA thickness can be measured as shown in Figure 8.9: both samples tested at RH = 82 % and 55 % had a thickness of 43 μm; in contrast the membrane thickness decreased significantly to 24 μm in the sample tested at RH = 36 %. The thickness here can be considered as a dry basis since SEM was conducted in a high vacuum environment. The thickness increase of Nafion® 112 membrane from a dry state to water soaked at room temperature, where the conductivity measurement was carried out, is about 21% [118]. The thicknesses of water-soaked samples following tests at RH = 82 % and 55 % are calculated to be 52 μm, which is very close to the values measured by the high-throughput conductivity instrument in Figure 8.3. For the sample tested at RH = 36 %, the calculated result is only 29 μm compared to the measured 35 μm in Figure 8.3, indicating the morphology or structure change caused by both chemical and mechanical degradation. Figures 8.9 (c) and (d) are the images from different locations in same degraded membrane. Figure 8.9 (c) shows the

membrane detached from the cathode due to significant membrane shrinkage after degradation. In contrast, a crack was formed close to the anode side in Figure 8.9 (d), which was developed from the delaminations observed in Figure 8.8 (c). EDS analysis was performed on the sample tested at RH = 36 % to study Pt dissolution into the membrane since it has been reported that Pt band formation is responsible for membrane degradation [119]. The Pt concentration inside membrane is very low in Figure 8.10, indicating that no significant Pt band formation under open circuit conditions. However, any Pt particles that penetrate into the membrane may act as a catalyst for OH free radical direct generation without the H_2O_2 intermediate and cause membrane degradation [92]. Moreover, the non-uniformity of membrane-electrode interface while assembling the MEA, and the serpentine flow channels may induce local pressure difference and degradation. There is also the possibility of carbon fibers from the GDL penetrating through the membrane.

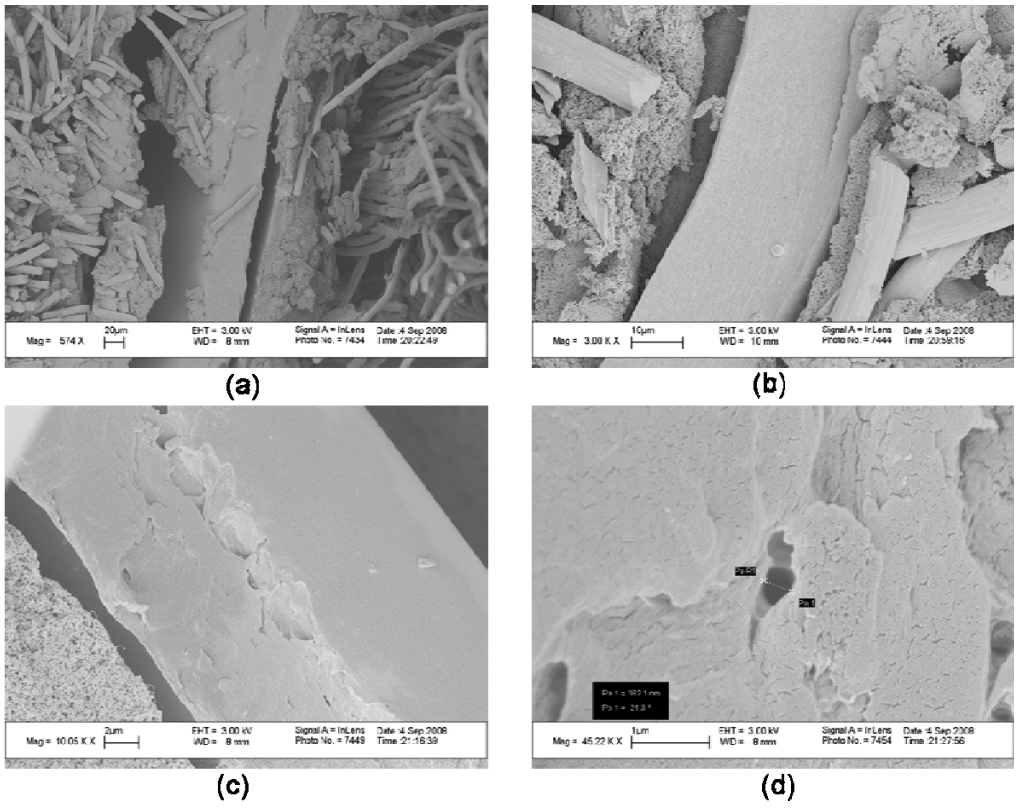

Figure 8.8. SEM images of membrane samples without resin preparation. (anode on the left)

(a) RH = 82 %; (b) RH = 55 %; (c) RH = 36 %; (d) a pinhole in figure (c).

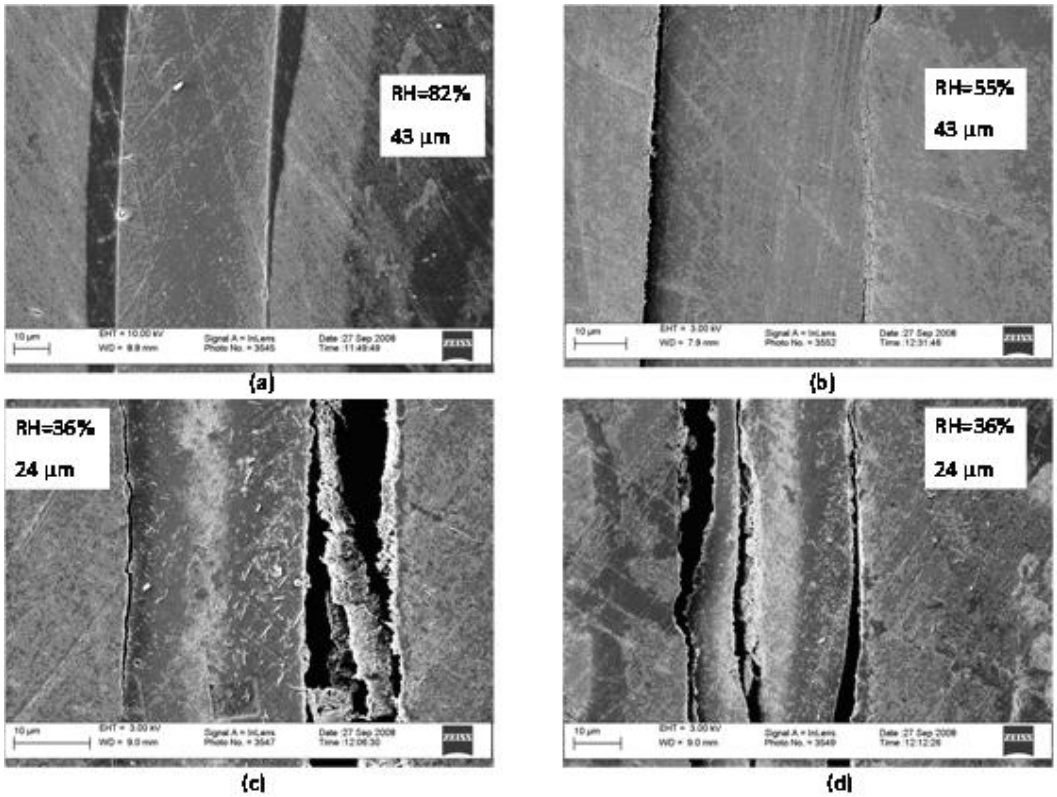

Figure 8.9. SEM images of different membrane samples in the resin. (anode on the left)

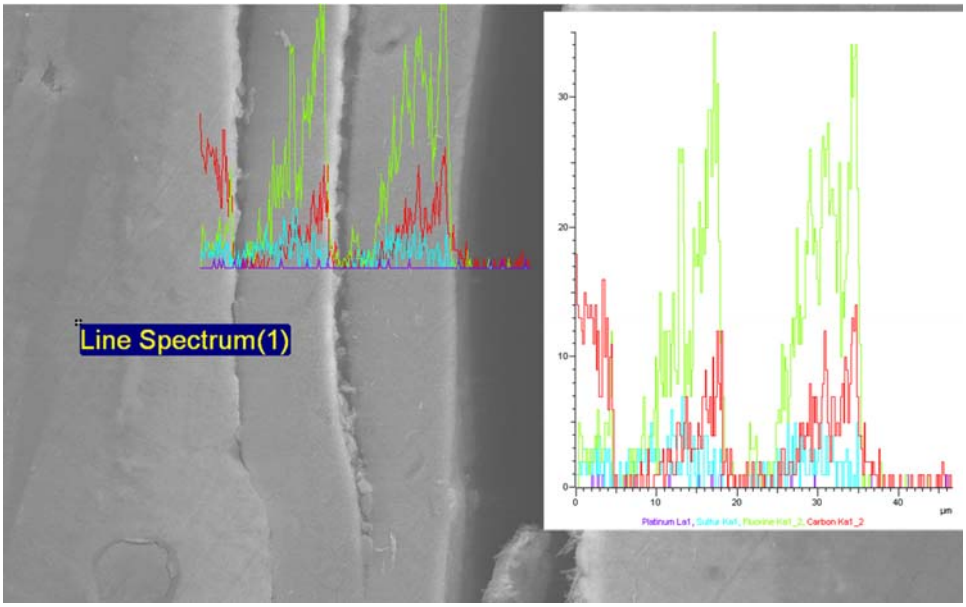

Figure 8.10. EDS line scan analysis over cross section of the sample at RH = 36 % (anode on the left).

(Platinum: Purple; Sulfur: blue; Fluorine: green; Carbon: red)

8.7 Membrane degradation model

Using our model for H_2O_2 formation in PEM fuel cells along with a few simplifications [24], the fluoride ion emission rates under different humidities can be calculated from the mechanism proposed by Curtin *et al*. [4]

$$M^{2+} + H_2O_2 \xrightarrow{k_1} M^{3+} + \cdot OH + OH^- \qquad \text{(Reaction 8.1)}$$

$$Rf - CF_2COOH + \cdot OH \xrightarrow{k_2} Rf - CF_2 \cdot + CO_2 + H_2O \qquad \text{(Reaction 8.2)}$$

$$Rf - CF_2 \cdot + \cdot OH \xrightarrow{k_3} Rf - CF_2OH \xrightarrow{-HF} Rf - COF \underset{-HF}{\overset{+H_2O}{\longrightarrow}} Rf - COOH$$

(Reaction 8.3)

The existence of terminal carboxylic acid groups and their role in degradation mechanism has been reported from DuPont [4], but concentrations of the terminal groups have not been provided and are treated as proprietary quantities, so there are no data available. Since Curtin's publication, manufacturers including DuPont have introduced more durable ionomers where an additional fluorination treatment has been done to lower these carboxylic acid groups, but again no data are available on the specific levels.

Assuming the content of carboxylic acid group in the membrane is constant, when fuel-cell operation achieves steady state and applying the stationary-state assumption:

$$\frac{d[Rf - CF_2\cdot]}{dt} = k_2[Rf - CF_2COOH][\cdot OH] - k_3[Rf - CF_2\cdot][\cdot OH] = 0$$

(Equation 8.4)

$$\frac{d[\cdot OH]}{dt} = k_1[M^{2+}][H_2O_2] - k_2[Rf - CF_2COOH][\cdot OH] - k_3[Rf - CF_2\cdot][\cdot OH] = 0$$

(Equation 8.5)

Finally, the rate of HF formation is given by:

$$\frac{d[HF]}{dt} = 2k_3[Rf - CF_2\cdot][\cdot OH] = k_1[M^{2+}][H_2O_2] \qquad \text{(Equation 8.6)}$$

In this approach, the rate limiting step in degradation is the formation of hydroxyl radicals. Here k_1 is the rate constant of Fenton's reaction. The only unknown in Equation (6) is the metal ion concentration (Fe^{2+}). Another assumption is that the [Fe^{2+}] remains constant under various humidities. Therefore, according to the experimental FER data at RH = 82 %, we were able to estimate the [Fe^{2+}], which was subsequently used to calculate the FERs under the low humidity conditions because no significant side chain degradation occurs under high humidity. The comparison between simulation results and average FER data from experiment as well as the calculated average H_2O_2 concentration in water phase of Nafion® membrane is shown in Figure 8.11. It can be seen that the simulation results fit well with experimental data under moderate humidities, which is also consistent with the H_2O_2 concentration in the membrane. However, the model seriously underpredicts FERs when the relative humidity is reduced to 36 %. This discrepancy suggests a possible change in the mechanism of degradation at lower water contents. It is hypothesized that the degradation is dominated by main chain unzipping process at high humidity where the rate of weak group formation is slow. The degradation rate is mostly determined by the H_2O_2 concentration inside membrane. As the humidity is lowered the side-chain scission process is accelerated, and more end

groups are created, which could significantly increase degradation rate and change rate determining step in degradation process.

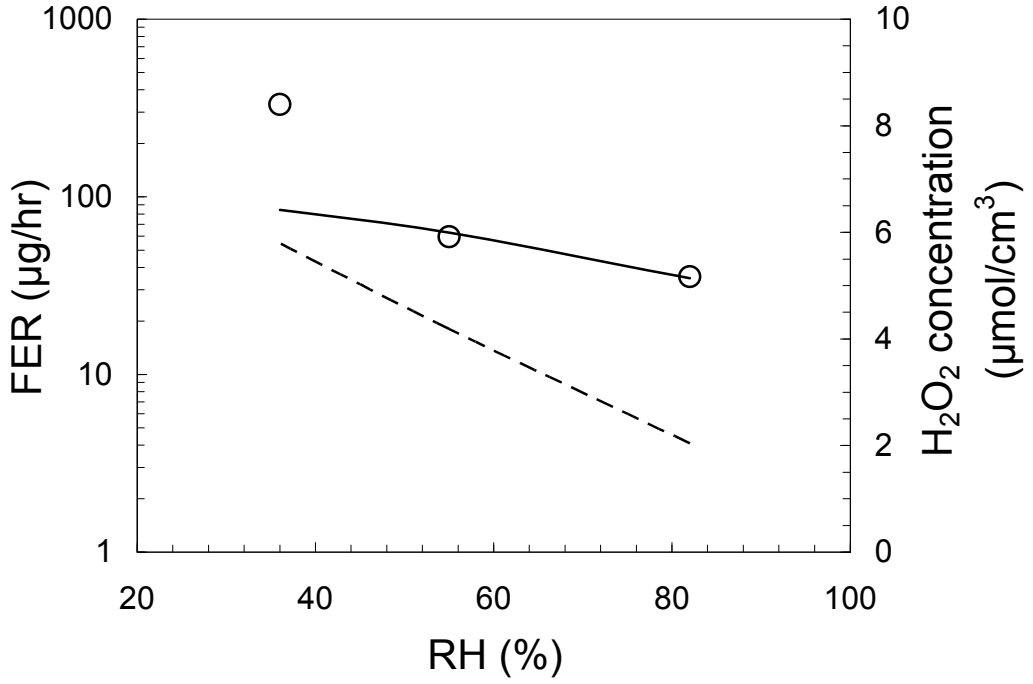

Figure 8.11. Comparison between simulation results and average fluoride ion emission rate data from experiment.

(○ Experimental data; —— Simulation results; ----- H_2O_2 concentration in water.)

8.8 Degradation reaction pathways

In summary, membrane degradation in proton exchange membrane fuel cells under various relative humidities can be considered as two schemes: main chain unzipping process and side chain scission process. It is difficult to determine the transition point where the dominant scheme changes because the side chain scission process is dependent on humidity and gradually enhanced with a decrease in humidity.

The following degradation pathway shows the main chain unzipping process with –COOH end group according to the mechanism proposed by Curtin *et al.* [4] and finally generates degradation product A [39, 57]:

Scheme 1. Main Chain Unzipping Process

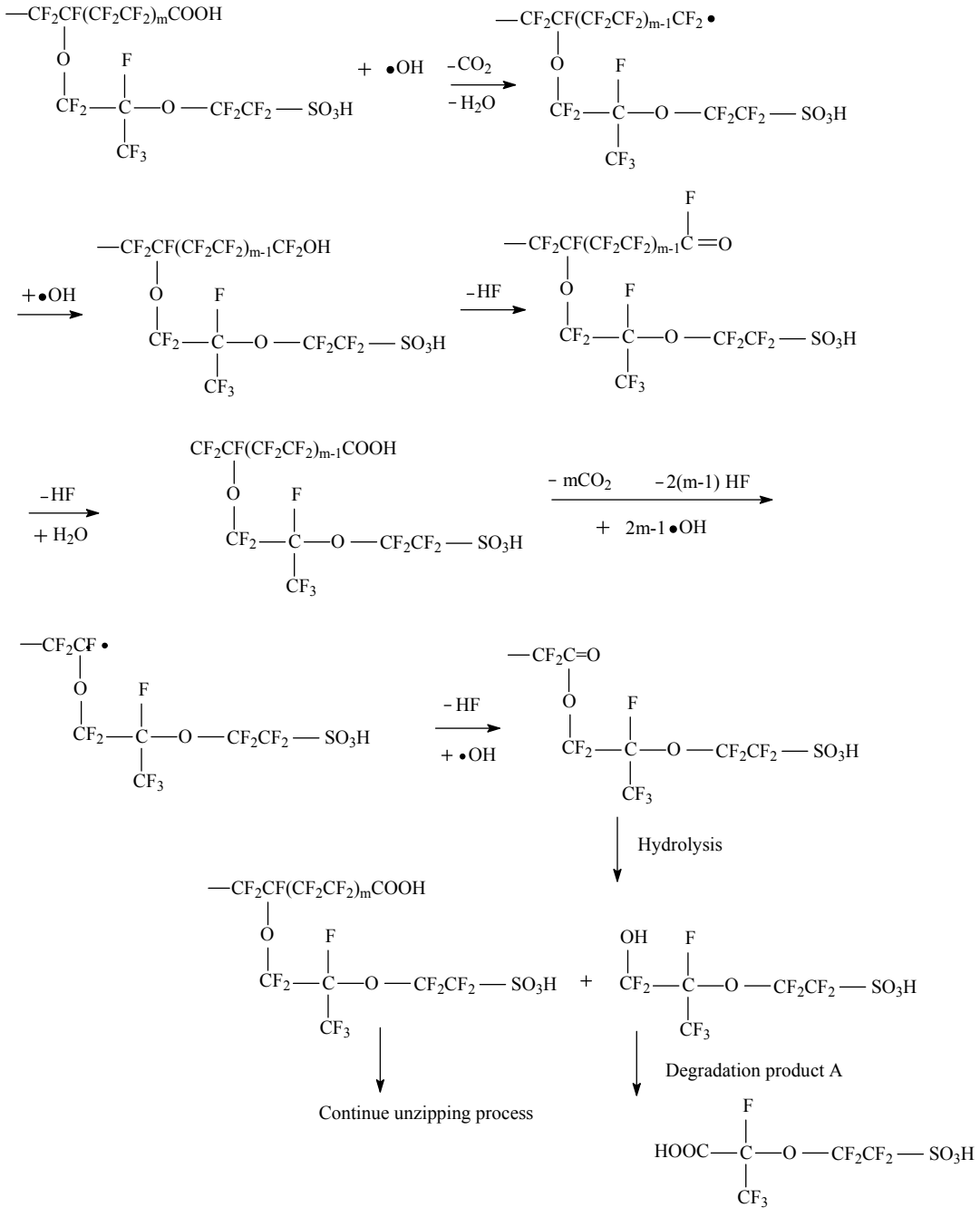

The side chain scission process is more complicated, since the reaction is slow and only noticeable after long-term operations. For the decomposition of C-O-C (A) group, there are could be several possible radical substitution reactions as long as a reasonably stable radical can be formed. Under low humidity conditions, the increased free radical concentration could attack the C-O-C (A) group [56, 57] by generating reasonably stable radical $\bullet CF_2R$ in the following degradation mechanism:

Scheme 2. Side Chain Scission Process

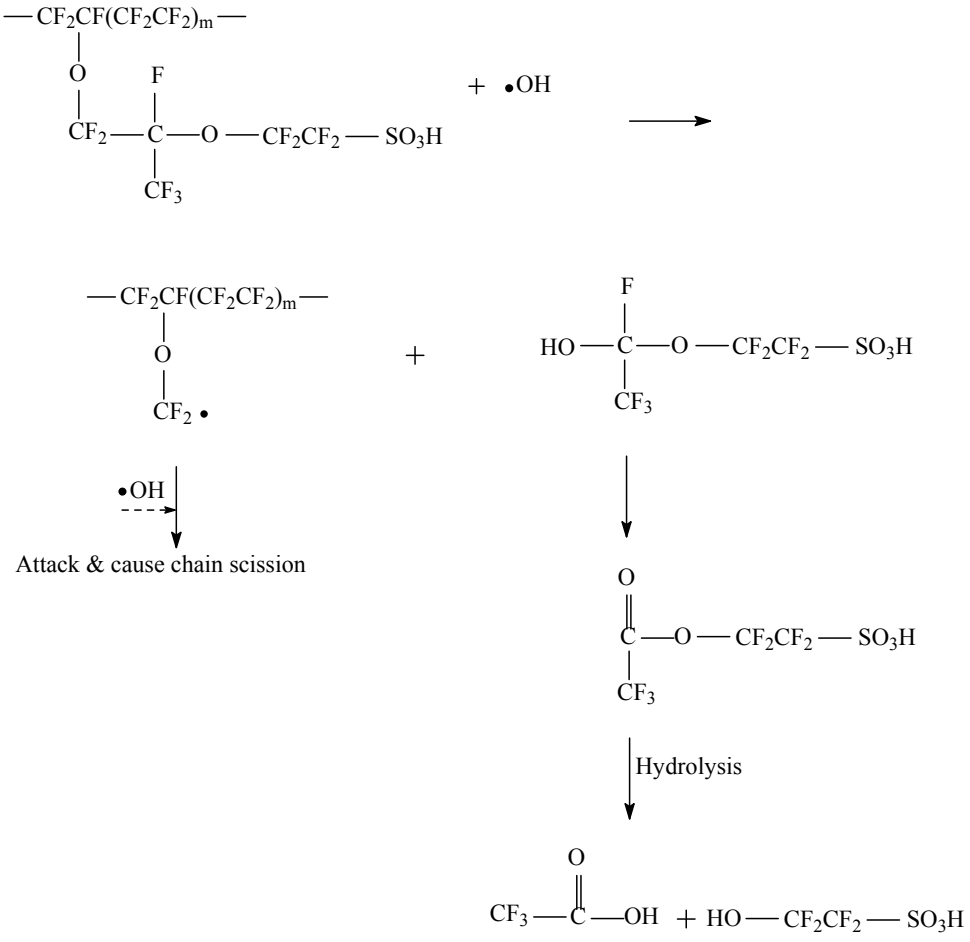

8.9 Summary

Analysis of exhaust water from the fuel cell demonstrates the existence of HF, SO_4^{2-} and TFA as degradation products. The rate of TFA emission shows a strong relationship with the FER, whereas the rate of sulfate ion emission was small indicating the direct C-S cleavage is insignificant in membrane degradation. The conductivity decreases as the level of humidity is reduced, mostly due to the loss of sulfonic acid groups or the replacement of proton during fuel-cell operation. After treatment with sulfuric acid, the conductivity of membrane samples tested under conditions of higher humidity recovers, which indicates that the decrease in conductivity was mainly caused by cation contamination. IEC measurements show a 8.3% decrease in capacity for the sample tested at the lowest humidity, which is consistent with the TER and conductivity data and provides strong evidence of side chain degradation. Furthermore investigations with FTIR show the loss of C-O-C (A) structure, corresponding well with the detection of TFA product. Based on TGA analysis, the thermal stability is lowered as the level of humidity is reduced. A new peak in DTA curve at around 200 ^{o}C of the sample tested at the lowest humidity indicates the formation of new weak group. Near the center of the degraded membrane SEM images revealed some pinholes and small signs of delamination consistent with severe membrane degradation. At the same time, EDS analysis confirmed that a Pt band did not form in the membrane. A model of membrane degradation based on main chain unzipping process was proposed, and the calculations show good agreement with experimental data under conditions of high humidity. The simulations show that the main chain unzipping process is dominant under high humidity. Whereas, a decrease in humidity enhances side chain scission process, creating a large amount of weak end groups and accelerating degradation. Finally, the representative

reaction pathways in each degradation scheme were speculated in order to explain the experimental findings.

CHAPTER 9

THE EFFECT OF TEMPERATURE ON THE DEGRADATION OF NAFION® MEMBRANE

In chapter 4, the experimental result highlights the potential for the application of XPS in membrane degradation under fuel-cell conditions, particularly for the elucidation of local effects since XPS is a strong surface analytical technique. In this chapter, the fuel cell was operated under various temperatures to investigate the degradation mechanism. Table 9.1 lists the operation conditions for corresponding durability tests and membrane samples. XPS spectra were collected from both anode and cathode sides of fuel-cell membrane to compare the effect of temperature on each side. Atomic analysis was performed to study the impact of temperature on both backbone decomposition and side group degradation. A multilayer MEA was used to study the effects of location and thickness on membrane degradation.

Table 9.1 Durability test conditions for membrane samples.

Sample/Test #	T_{Cell}	RH	Duration	Gas type	Membrane type
1	-	-	-	-	Virgin Nafion® 112
2	90 °C	36%	120 hrs	$H_2//O_2$	One Nafion® 112
3	70 °C	36%	120 hrs	$H_2//O_2$	One Nafion® 112
4	50 °C	36%	120 hrs	$H_2//O_2$	One Nafion® 112
5	90 °C	36%	120 hrs	$H_2//O_2$	Two Nafion® 112

9.1 Temperature and membrane thickness effects on FER

Figure 9.1 shows the effect of temperature and membrane thickness on the FERs. Clearly, high temperature increases membrane degradation due to the accelerated reaction kinetics. However, the apparent activation energy is calculated to be 139.4 kJ mol^{-1}, much higher than the 75 kJ mol^{-1} of Fenton's test reported by LaConti *et al.* [23]. This nearly double activation energy implies that a different degradation mechanism may exist between the *ex-situ* Fenton's test and the *in-situ* fuel-cell experiment. Using the model we have previous developed [26], the activation energy based on main chain zipping mechanism is calculated to be 63.4 kJ/mol, which is still much lower than experimental value. It is also interesting to note that the FER vs. time curves show similar pattern trend for test 2 and 5 with the same temperature and humidity. Figure 9.2 shows the molar ratio of FER/TER, and it can be seen that test 3 with lower temperature shows a slightly higher ratio, whereas the ratio of tests 2 and 5 with the same temperature and humidity are very close during entire run, indicating the degradation mechanism is largely dependent on the operation conditions.

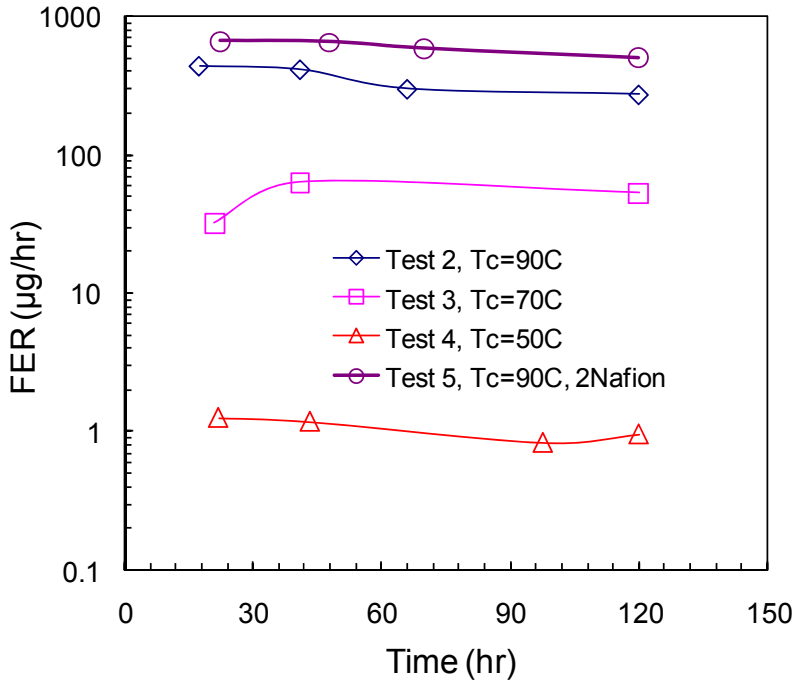

Figure 9.1. FER with different temperatures and membrane thickness.

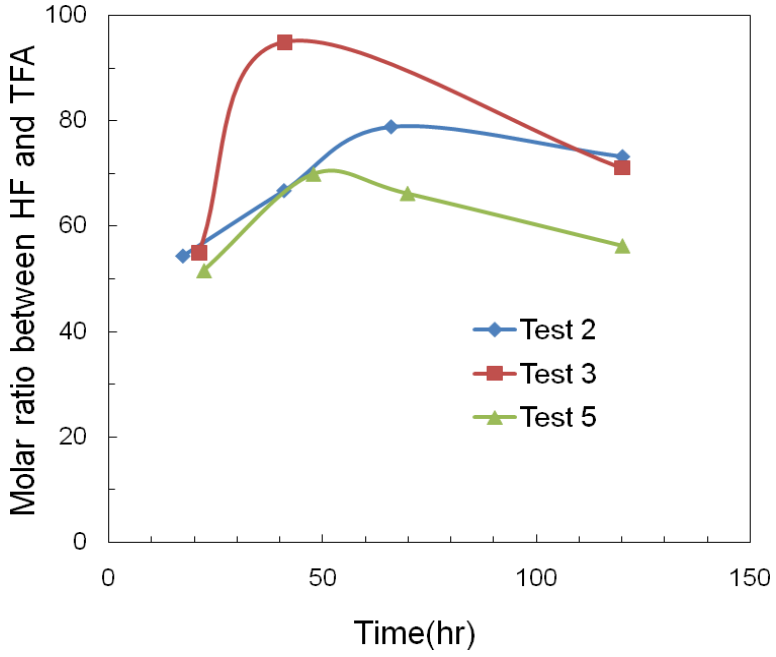

Figure 9.2. Molar ratio between HF and TFA from different tests.

9.2 Effect of temperature on membrane degradation

Both anode and cathode sides of degraded membrane samples were analyzed by XPS and the spectra are shown in Figure 9.3. For a given sample, the spectra from both the anode and cathode show similar patterns. With an increase of temperature, the whole spectra shift to higher binding energy, which means the sample becomes less conductive. This result indicates membrane degradation under high temperature could increase the interfacial resistance and cause fuel-cell performance decay.

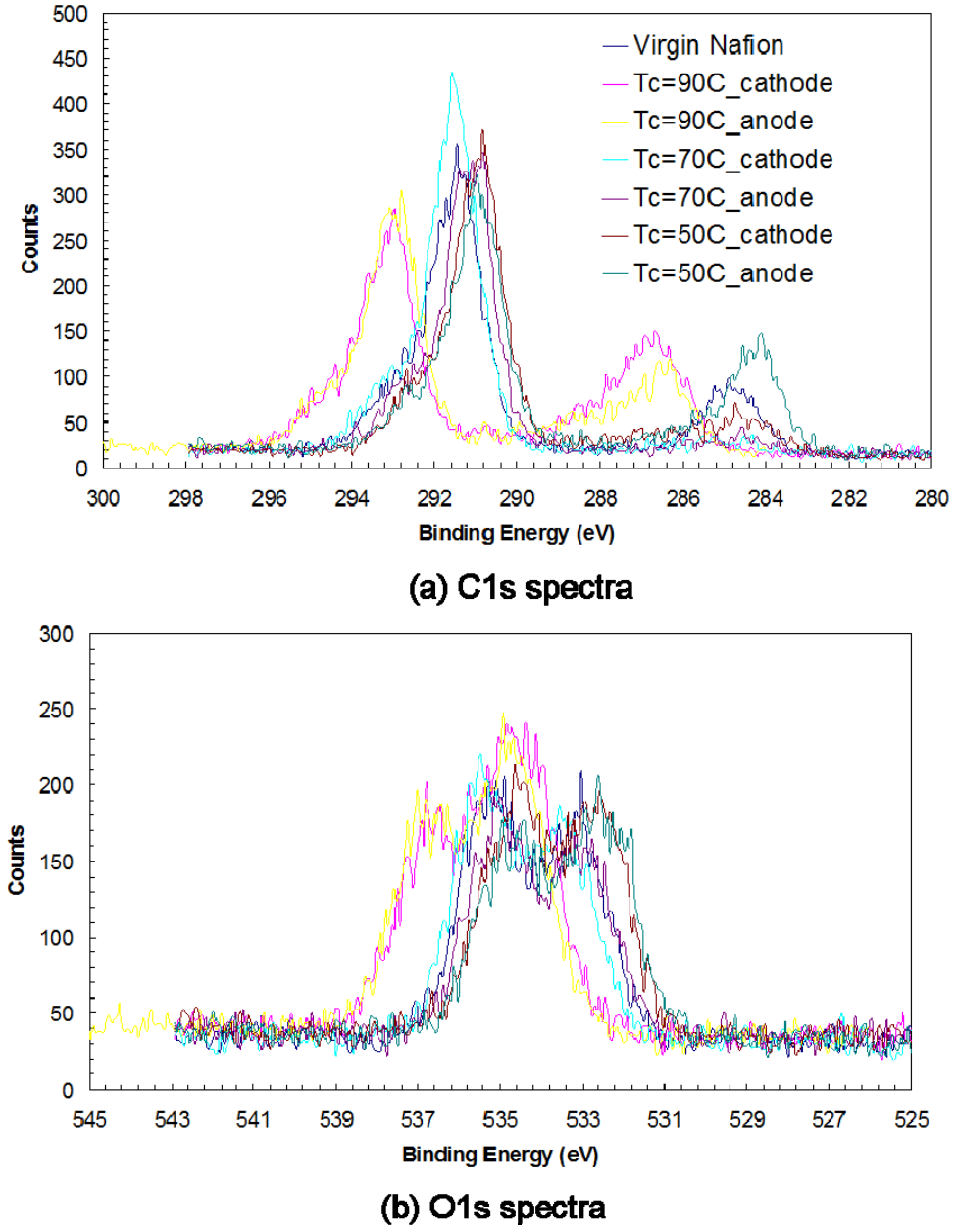

Figure 9.3. XPS spectra under different temperatures.

Figure 9.3 (a) shows the C1s spectra of various membrane samples. For carbon in the CF_2 configuration, the binding energy (Eb) is 291 eV (highest binding energy peak). The XPS peak at Eb = 284.2 eV can be related to the carbon in C–CF or C–C configuration. It can be seen that the intensity of peak at 291 eV decreases with the

increase of operating temperature, indicating the decomposition of carbon backbone. Compared to virgin Nafion® membrane, the intensity of the peak at 284 eV increases for some membrane samples after fuel-cell testing. This can be attributed to the carbon fiber that has penetrated into the membrane surface during fuel-cell test [26] or membrane-sample preparation.

Figure 9.3 (b) shows the O1s spectra of various membrane samples. Oxygen in Nafion® membrane has two different binding states: three oxygen atoms are bound in each sulfonic acid group, indicated by Eb = 535.7 eV (highest binding energy peak). Two of the oxygen atoms in the polymer chain are in ether configurations with Eb = 533 eV (lower binding energy peak). We can observe the increase of peak intensity at low binding energy, indicating the loss of sulfonic acid groups or the increase of ether linkage by adding more oxygen atoms to polymer chain.

Table 9.2 gives the quantitative (peak fitting) XPS results. Again, the increase in graphitic carbon can be seen in some samples especially under high temperature such as 90 ^{o}C, close to the glass transition temperature of Nafion® membrane (~ 110 ^{o}C). The percentage of oxygen atoms increases in sample 2, which may be due to the loss of fluorine atoms and an increase of oxygen-rich moieties from degradation. The ratio between fluorine atoms and $(CF_2)_n$ can give us important information on polymer degradation schemes since this ratio is higher for the side chain than for the carbon backbone. Decomposition of the polymer backbone can increase this ratio [64], which represents the main chain unzipping process. On the other hand, the side chain degradation decreases this ratio, which can be treated as an indicator for the side chain scission process. Figure 4 shows the ratio between fluorine atoms and CF_2 structure in

different membrane samples. Under low temperature conditions, such as test 4 (50 ^{o}C), membrane degradation is so slow that neither changes in the carbon backbone nor the side chain can be observed; therefore, the ratio remains the same as virgin Nafion® membrane. This is also proved by the FER data (less than 0.1 % total F loss). With the temperature increase in test 3 (70 ^{o}C), the rate of membrane degradation increases but the decomposition of the side chain slows (~ 2 % side group loss). Therefore, what we observed is an increase in the ratio of fluorine atoms and $(CF_2)_n$ at both the anode and cathode. The cathode has even higher ratio than the anode, signifying the decomposition of carbon backbone also occurs at cathode; however, the side chain degradation is higher at the anode, which slightly decreases the ratio at the anode side. This is different from H_2O_2 induced degradation mechanism since H_2O_2 concentration is low at cathode [24]. Hence, these results illustrate the existence of other degradation mechanisms either not involved with H_2O_2 attack or controlled by different rate determining step. For the highest temperature (test 2 at 90 ^{o}C), the ratio decreases significantly especially at anode, showing that the free radical generated H_2O_2 catalytic decomposition at anode could decompose the polymer side chain. For example, the OH radical can attack the C-O-C structure in the middle of side chain with the formation of TFA as one of the degradation products [26]. It is also interesting to note that side chain degradation is observed at cathode side under this condition, which may be caused by the free radical directly formed on Pt catalyst under potential above 0.5 V [33, 35].

Table 9.2 XPS results for different samples

Sample #		Carbon			Oxygen			Fluorine	Sulfur
		Total	$(CF_2)_n$	Graphite	Total	C-O	SO_3H		
1		29.98	26.767	3.213	8.937	4.239	4.698	59.233	1.851
2	Cathode	38.076	23.241	14.835	11.141	7.45	3.691	49.282	1.501
	Anode	38.096	25.937	12.159	10.111	5.816	4.295	50.729	1.046
3	Cathode	28.502	25.789	2.713	8.387	4.069	4.318	61.144	1.968
	Anode	28.842	26.296	2.546	8.24	3.886	4.354	60.816	2.102
4	Cathode	31.993	25.805	6.188	8.856	3.811	5.045	57.642	1.509
	Anode	35.381	24.507	10.874	8.798	4.077	4.721	54.406	1.415
5	Cathode	32.032	25.86	6.172	8.393	3.827	4.566	57.886	1.69
	Middle	33.249	23.18	10.069	7.265	2.985	4.28	57.953	1.553
	Anode	33.33	26.979	6.351	8.766	4.49	4.276	56.077	1.827

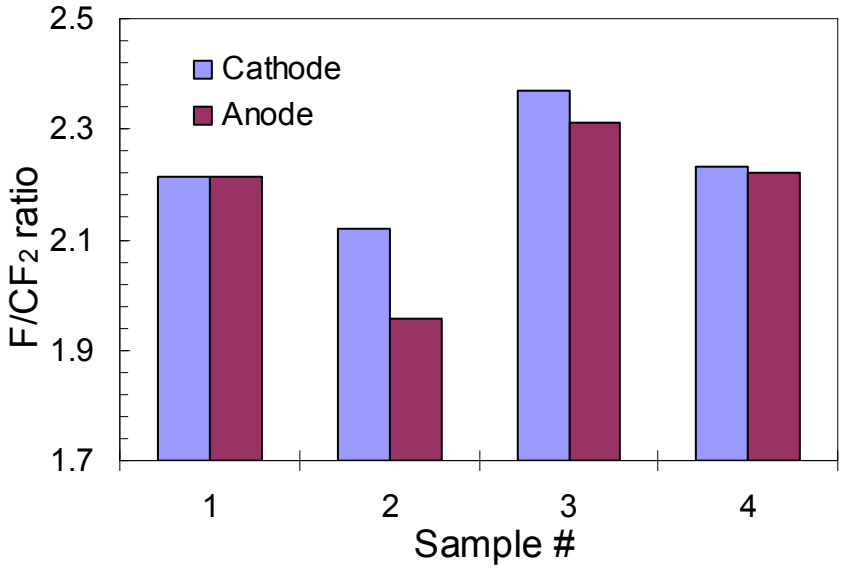

Figure 9.4. F/CF_2 ratio with various temperatures.

Furthermore, the decomposition of the side chain can be studied by comparing the ratio of oxygen atoms in $-SO_3H$ and ether structure. However, it may be difficult to compare the ratio at the cathode due to the interference of carbon fibers that may have been oxidized during fuel-cell operation. Figure 5 shows the change of this ratio at the anode under different temperatures. For virgin Nafion® membrane, this ratio is only slightly above 1 and less than 3:2, which is calculated from its starting chemical structure. Since no pretreatment procedure was conducted, this low value could be explained by inadequate sulfonic acid group moving from bulk to the surface [64]. From Figure 9.5 we can see the ratios of sample 3 and 4 are close to that of the virgin Nafion® membrane, indicating insignificant side chain decomposition under low temperature. Conversely, sample 2 shows significant decrease in the ratio due to the loss of sulfonic acid group, which is consistent with the previous analysis in Figure 9.4. Since emission of SO_4^{2-} is very low in all the tests, we assume the side chain cleavage occurs at the second ether

linkage close to sulfonic acid group. Then the percentage of side group degradation can be calculated to be 50 % at anode in sample 2 and this value will be higher if the scission process occurs at the same time and the whole side chain is lost. This value is much higher than the average side group loss of 13.4 % from TER calculation, indicating side group degradation mainly occurs at anode side under this condition.

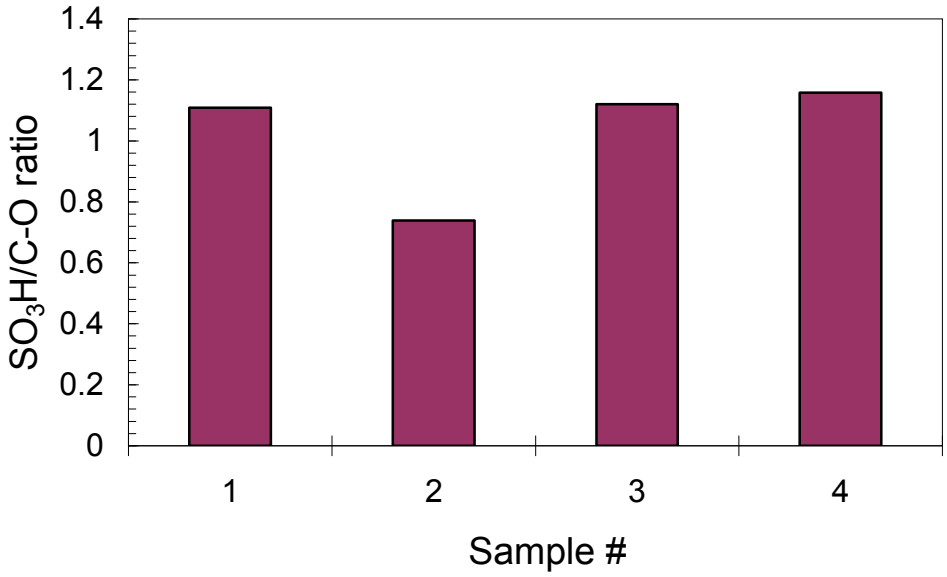

Figure 9.5. SO_3H/C-O ratio of anode side.

9.3 Effect of location on membrane degradation.

We have already investigated the degradation at both anode and cathode in the above discussions. Nevertheless, what happens in the bulk membrane compared to both sides is still unclear. One way to obtain the depth profile is to use ion etching, but it can change the polymer structure since it's destructive [64]. Therefore, a better way to take a look at membrane inside is to use a multilayer MEA that we have developed [37]. The

XPS spectra of Nafion® membrane at different locations (cathode, middle, and anode) are shown in Figure 9.6. It can be observed that the binding energies of the whole spectra follow this order: anode > cathode > middle. As we discussed before, the shift to higher binding energy indicates higher surface resistance. This result shows that the resistance at electrode-membrane interface increases after fuel-cell operation compared to bulk membrane. Also, the membrane sample at the anode shows further shift to higher binding energy. This may be due to the large loss of conductive groups there.

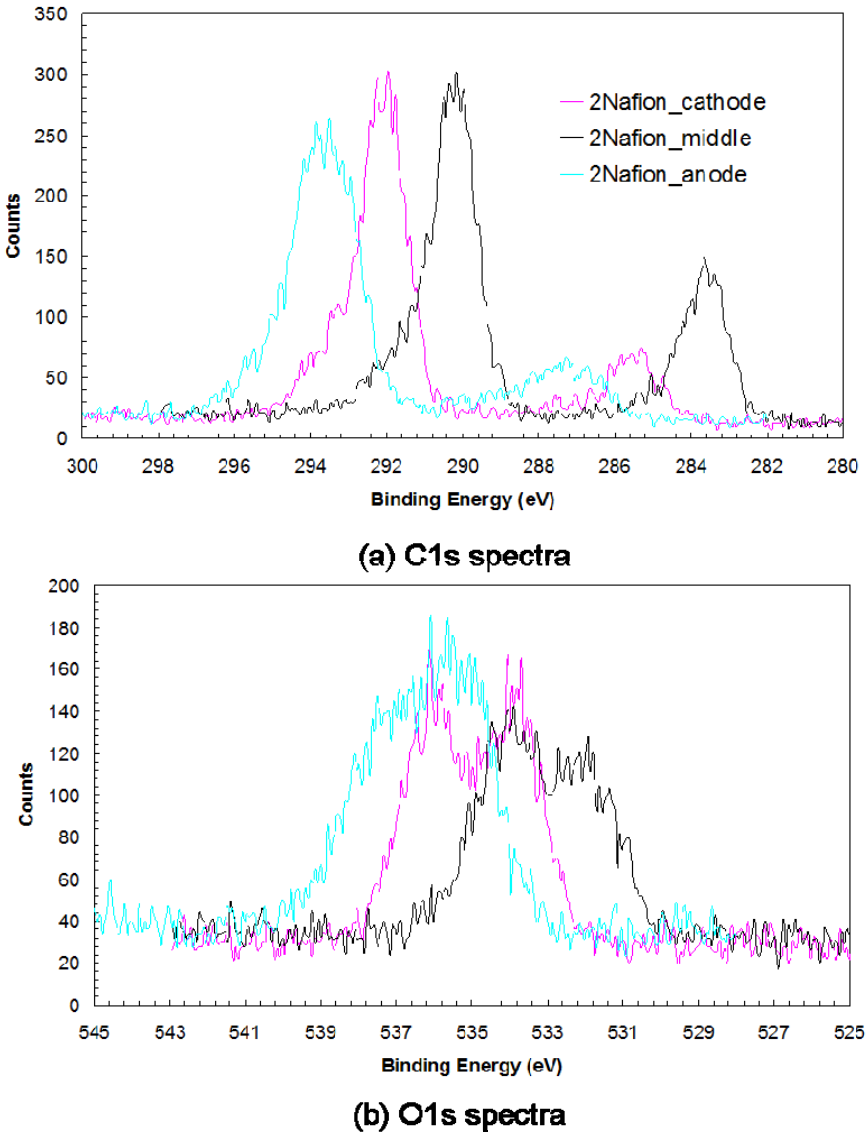

Figure 9.6. XPS spectra from a multilayer MEA.

Figure 9.6 (a) shows C1s spectra of membrane samples from different locations in the same membrane. An obvious increase in intensity of the C1s peak at low binding energy can be seen in the sample from the middle. This can be ascribed to the decomposition of the carbon backbone. Figure 9.6 (b) shows O1 spectra of different samples. We can clearly see that the ratio between high binding energy ($-SO_3H$) and low

binding energy (C-O) peaks becomes smaller as the whole spectra shift to higher binding energy. The decrease in this ratio can be considered as an indicator of conductive group loss, which corresponds well with the previous conclusion that surface resistance increases at the electrode-membrane interface.

An analysis of the atomic percentages is shown in Table 9.2 and Figure 9.7. It can be seen in Figure 9.7 that the ratio between fluorine atoms and $(CF_2)_n$ groups as well as -SO_3H/C-O ratio at cathode are the same as in virgin Nafion® membrane. This indicates that the cathode side has little or negligible degradation. However, the cathode side of sample 2, which has half the membrane thickness, shows slightly side group degradation. The difference here is mainly caused by the low gas permeation in sample 5. At the anode, both F/CF_2 and $–SO_3H$/C-O ratios decrease, which indicates significant side chain degradation occurs there. However, the two ratios are both higher than for sample 2 and closer to the value of virgin Nafion® membrane, which again confirms that an increase in membrane thickness could decelerate membrane degradation.

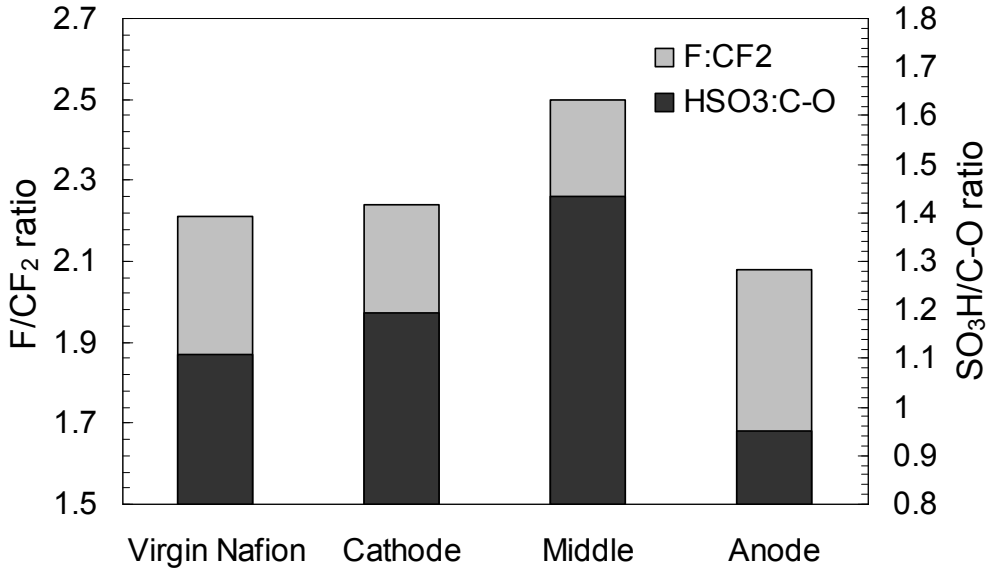

Figure 9.7. Atomic analysis on different locations in the same sample.

The F/CF_2 ratio in the middle of sample 6 increases after fuel-cell test, showing the decomposition of carbon backbone. At the same time the ratio between $–SO_3H$ and C-O structure also increases compared to virgin Nafion® membrane, which again can be explained by the different state of sulfonic group in surface and bulk. The H_2O_2 concentration in the bulk membrane is lower than at the anode side [36], and the side chain degradation is slow, which can be observed from the $–SO_3H$/C-O ratio. On the other hand, the increase in the F/CF_2 ratio shows significant main chain degradation, which implies that other chemical species may also be able to accelerate main chain degradation. The possible other reactive oxygen species could be the oxygen molecule itself. Polymer degradation involved with O_2 is common for most hydrocarbon polymers. For example, the degradation of hydrocarbon fuel-cell membrane containing aromatic rings can be initiated by OH radical and propagated by O_2 molecule [120]. Investigation

of perfluoroperoxy radicals reaction by kinetic EPR spectroscopy shows the existence of the following reactions under low temperature [121]:

$$Rf - CF_2 \cdot + O_2 \xrightarrow{k_4} Rf - CF_2OO \cdot \qquad \text{(Reaction 9.1)}$$

$$2Rf - CF_2OO \cdot \xrightarrow{k_5} 2Rf - CF_2O \cdot + O_2 \qquad \text{(Reaction 9.2)}$$

$$Rf - CF_2O \cdot \xrightarrow{k_6} Rf - CF_2 \cdot + CF_2O \qquad \text{(Reaction 9.3)}$$

Once the Rf-CF_2· radical is formed from weak endgroups [4], it could be further attacked by an oxygen molecule. The oxygen concentration in the bulk membrane is higher than at the anode side; therefore, the backbone decomposition rate could be high although side chain degradation is low. On the other hand, at the cathode side, although oxygen concentration is high, the radical concentration available to initiate degradation is low, which results in both slow side chain degradation and main chain unzipping.

9.4 A kinetic model of membrane degradation

In our previous report, a simple degradation model was built based on Dupont's proposed mechanism; however, it significantly underpredicts FERs at conditions of extremely low humidity. The reason is that the impact of side group degradation on FER wasn't considered in that model. Moreover, recent study shows a linear relationship and non-zero intercept when plotting fluoride generation rates vs. carboxylic acid content in Nafion® [28]. This suggests that the degradation cannot be just the simple OH radical attack. From the above experimental results, the degradation reactions (1) - (3) involved with molecular oxygen can be considered as an alternative main chain unzipping process.

Further, the XPS investigation has already validated the side chain degradation, although the details of degradation are still unclear. Here we use the following reaction to represent the overall side chain scission process [29]:

$$Rf - CF_2SO_3H + X \xrightarrow{k_8} 2Rf - CF_2COOH \qquad \text{(Reaction 9.4)}$$

Therefore, similar to ordinary polymer degradation by oxidation, three steps could be proposed here.

First, the degradation is initiated by the free radicals generated from Fenton's reaction:

$$Fe^{2+} + H_2O_2 \xrightarrow{k_1} Fe^{3+} + \cdot OH + OH^- \qquad \text{(Reaction 9.5)}$$

$$Rf - CF_2COOH + \cdot OH \xrightarrow{k_2} Rf - CF_2 \cdot + H_2O + CO_2 \uparrow \qquad \text{(Reaction 9.6)}$$

The next propagation step includes reaction (1) – (3) and the main chain unzipping caused by ·OH radical itself:

$$Rf - CF_2 \cdot + \cdot OH \xrightarrow{k_3} Rf - CF_2OH \rightarrow Rf - COF \rightarrow Rf - CF_2COOH$$

(Reaction 9.7)

Slow termination could occur due to the interaction between long chain radicals and this process could increase polymer chain length. This may be the reason why Young's modulus increased after significant membrane degradation [26].

$$2Rf - CF_2 \cdot \xrightarrow{k_7} Rf - CF_2CF_2 - Rf \qquad \text{(Reaction 9.8)}$$

After applying the stationary state assumption as shown in the appendix, we could derive a HF formation rate expression:

$$\frac{d[HF]}{dt} = k_1[Fe^{2+}][H_2O_2] + \frac{4k_7k_2}{k_4}[Rf - CF_2COOH][O_2] \qquad \text{(Equation 9.1)}$$

Clearly we can see here the HF emission rate has linear relationship with the carboxylic acid group content and a non-zero intercept can be observed due to the contribution from Fenton' reaction.

Since new –COOH group can be regenerated during main chain unzipping process; in total, this process doesn't affect the –COOH concentration. Only side chain scission can increase the amount of –COOH group and the termination reaction (8) could reduce its concentration by coupling two perfluorinated radicals:

$$\frac{d[Rf-CF_2COOH]}{dt} = 2k_8[Rf-CF_2SO_3H][X] - 2k_7[Rf-CF_2\cdot]^2$$

(Equation 9.2)

Once the degradation process achieves pseudo steady state and the fluoride ion emission rate becomes stable, we could assume the concentration of –COOH is constant and this concentration can be calculated as shown in the appendix. If the $–SO_3H$ group concentration changes with time due to side chain scission process, the HF formation rate can be derived as:

$$\frac{d[HF]}{dt} = k_1[Fe^{2+}][H_2O_2] + A(\frac{[Rf-CF_2SO_3H]}{[Rf-CF_2SO_3H]_0})^{1/2} = B + A(\frac{[Rf-CF_2SO_3H]}{[Rf-CF_2SO_3H]_0})^{1/2}$$

(Equation 9.3)

Here, we define A and B are the contributions from side group degradation and Fenton's reaction, respectively. They depend on the polymer material properties and operational conditions, such as humidity, temperature, gas partial pressures etc. Based on this equation, the FER data in Figure 1 can be well explained. Under lowest temperature such as test 4, FER decreases with time due to the consumption of –COOH group in degradation process, whereas the free radical concentration is too low to decompose the

side group. In contrast, FER from test 3 shows increase at the beginning due to the formation of –COOH groups from side chain scission process. However, the rate of this process is low, so the time to reach steady state is relatively long in this test. The most interesting FER results are from test 2 and 5, and both of them show the same trend in FER vs. time since the operational conditions are the same. The FER data are constant initially but decrease at the end of the tests because significant decomposition of side groups decreases $-SO_3H$ group concentration in Equation 10.

However, the above explanation is only qualitative and further quantitative analysis is needed to further validate the proposed mechanism. In our previous report, the contribution from Fenton's test can be calculated from high humidity conditions, which fits well with experimental data. We assume Fe^{2+} concentration is constant under certain temperature and it was calculated to be 0.1 mg/L. However, under low humidity and high temperature, the simulation value is much smaller than experimental result. That's because in that model we didn't consider the contribution from side group degradation, which becomes more and more significant with decreasing humidity and increasing temperature. After obtaining A and B value, a further dynamic model can be built to quantitatively explain the experimental data.

Since Nafion® is a random polymer, statistically, the loss fraction for the side chain and fluorine should equal [29]:

$$\frac{[Rf-CF_2SO_3H]}{[Rf-CF_2SO_3H]_0}=\frac{[F]}{[F]_0} \qquad \text{(Equation 9.4)}$$

Therefore, we could integrate Equation (9.3) with time:

$$\Delta F=[F]_0-[F]=Bt+\int_0^t A(1-\frac{\Delta F}{[F]_0})^{1/2}dt \qquad \text{(Equation 9.5)}$$

Finally a rate expression could be obtained:

$$(1-\frac{\Delta F}{[F]_0})^{1/2} = \frac{\exp(-\frac{A}{2[F]_0 t})(A+B)-B}{A} \qquad \text{(Equation 9.6)}$$

The membrane volume change caused by loss of HF was not included in previous calculation, and the membrane shrinkage becomes more important after long time operation [26]. Here we assume the change of membrane volume is linear with fluorine content:

$$\frac{V}{V_0} = \frac{[F]}{[F]_0} \qquad \text{(Equation 9.7)}$$

So we can have an improved rate expression with considering volume change:

$$(1-\frac{\Delta F}{[F]_0})^{1/2} = \frac{B}{\exp(\frac{B}{2[F]_0 t})(A+B)-A} \qquad \text{(Equation 9.8)}$$

Figure 9.8 shows the comparison between experimental data from test 2 and simulation results based on different models. As we can see, the simple model based on constant FER has a large deviation from experimental data after 50 hrs operation. The two models with membrane volume change and side group degradation based on Equation (14) match the data better, whereas the model from Equation (16) has the best prediction of experimental data. Therefore, this result again clearly implies the significance of side group degradation under high temperature. However, more details about side group degradation need to be explored in order to provide a prediction of membrane degradation and lifetime corresponding to certain operation conditions and MEA properties.

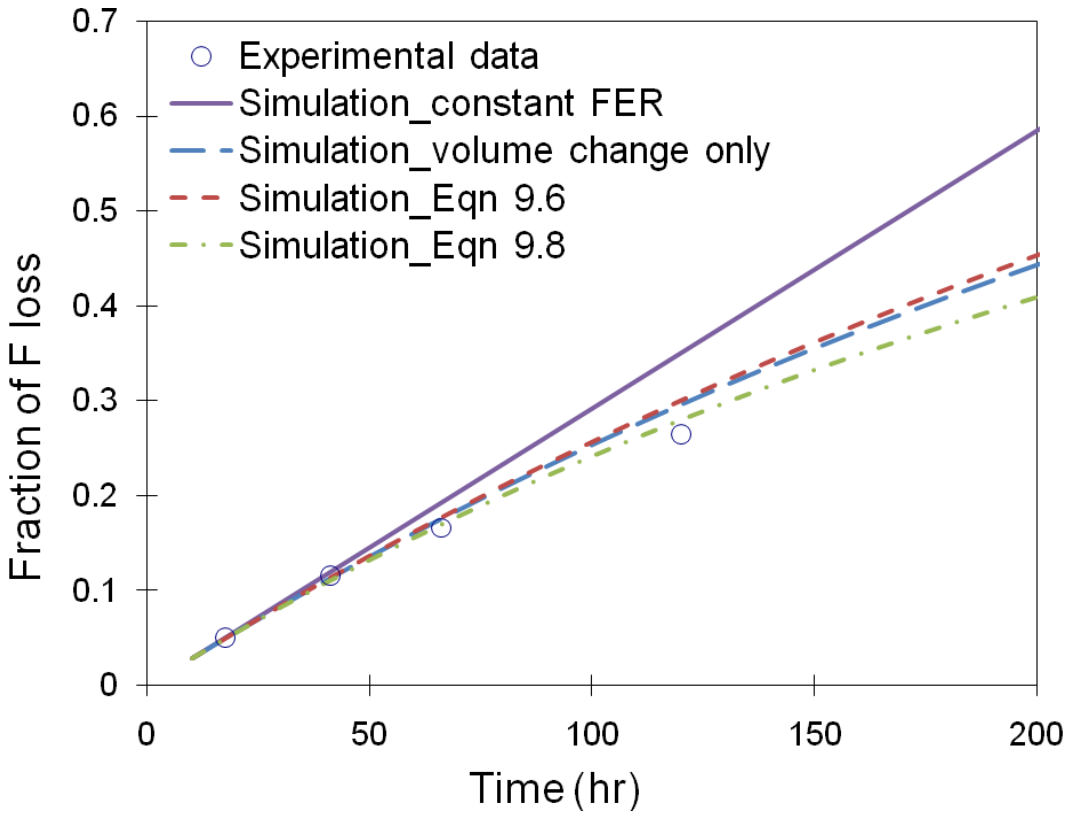

Figure 9.8. Comparison of experimental data from test 2 and various modeling results.

9.5 Summary

The effect of temperature on membrane degradation was studied in this paper and FERs were measured by collecting the fuel-cell water. The apparent activation energy was calculated to be 139.4 kJ mol^{-1}, which is much higher than either Fenton's test or simulation value from our previous model. Further HF/TFA ratio analysis indicated degradation mechanism is largely dependent on the operating conditions. XPS analysis of membrane samples under different temperatures clearly shows both main chain and side groups suffer degradation under fuel-cell conditions and the degradation is accelerated by high temperature. In the same membrane, anode side shows more significant degradation

than cathode side and this is mainly attributed to the high H_2O_2 and radical concentration at anode. It is interesting to notice that the side groups at cathode side also degrade which may be caused by the direct radical formation on Pt catalyst. Membrane degradation at bulk membrane was studied using a multi-layer MEA and the results indicate significant backbone decomposition occurs there whereas the side group degradation rate is slow. All these experimental results show that besides OH radical, other oxidative species such as O_2 molecule in the membrane could also attack carbon backbone by interacting with long chain radicals. The membrane degradation process is proposed to include four steps: initiation, propagation, termination and side group degradation. A kinetic model was built based on this mechanism which explains the experimental data very well.

CHAPTER 10

PEROXIDE DECOMPOSITION REAGENT STUDY

In the previous chapters 6 and 7, the concentration of H_2O_2 was determined and its formation was modeled under fuel-cell conditions. The modeling result suggested that adding a peroxide decomposition reagent that doesn't have Fenton activity could improve membrane durability. Therefore, in this chapter, an attempt to extend membrane lifetime by peroxide decomposition reagent was performed and some initial data were obtained.

Here we use TEMPO (2,2,6,6-Tetramethylpiperidine-1-oxyl) radical as peroxide decomposition reagent because it is a stable radical, and its cation form could penetrate into polymer membrane electrolyte and decompose the generated H_2O_2. The study here were conducted with 4-Acetamido-TEMPO, also called 4-Acetamido-2,2,6,6-tetramethyl-1-piperidinyloxy, which was purchased from Tokyo Chemical Industry (TCI). Figure 10.1 shows the structure of itself and other forms at different oxidation state.

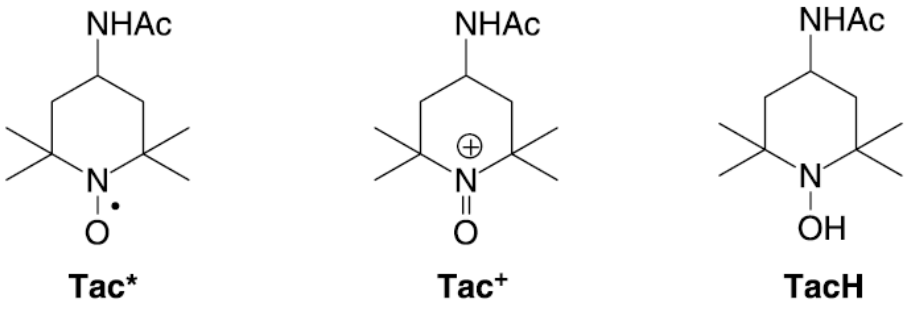

Figure 10.1. Structure of 4-Acetamido-TEMPO at different oxidation state [122].

The cation form of this radical, Tac^+, has the ability to decompose H_2O_2 rapidly over a broad pH range via the following reaction:

$$2Tac^+ + H_2O_2 \rightarrow 2Tac^* + O_2 + 2H^+ \qquad \text{(Reaction 10.1)}$$

More importantly, the neutral Tac* can be oxidized by hydroxyl and hydroperoxyl radicals and further reduce the amount of hydroxyl radical in the membrane [123].

$$Tac^* + \cdot OH + H^+ \rightarrow Tac^+ + H_2O \qquad \text{(Reaction 10.2)}$$

$$Tac^* + \cdot O_2H + H^+ \rightarrow Tac^+ + H_2O_2 \qquad \text{(Reaction 10.3)}$$

Since the oxidizing potential for Tac* is about 0.7 V (NHE), it is expected to be oxidized at the fuel-cell cathode under open-circuit or low current conditions and then diffuse back into the membrane:

$$Tac^* \rightarrow Tac^+ + e^- \qquad \text{(Reaction 10.4)}$$

Therefore, the fuel-cell test was conducted with special MEA composed of two GDEs (gas diffusion electrodes) and one Nafion® 112 membrane as show in Figure 10.2. The purpose of using GDE here is to easily disperse Tac* at the interface between cathode electrode and membrane. In this experiment, 1 ml 4-Acetamido-TEMPO solution (concentration ~ 1%) was doped at cathode side as shown in Figure 10.2. After applying H_2 and O_2 to the fuel cell, the potential at cathode was raised up to more than 0.9 V (as shown in later OCV data), Tac* will be oxidized into Tac^+ and diffuse into the Nafion® membrane due to its ion exchange ability.

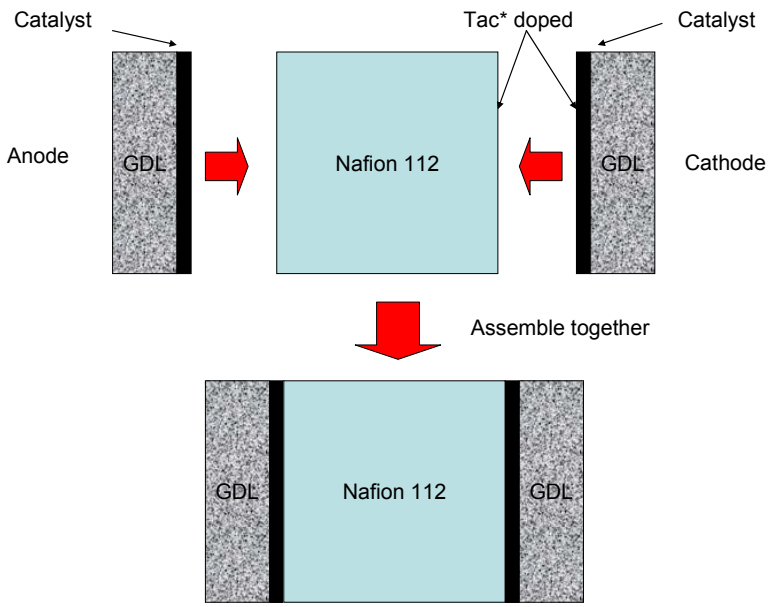

Figure 10.2. Cell design for peroxide decomposition experiment.

10.1 OCV curve

Figure 10.3 shows the OCV change during fuel cell tests without Tac* (test 1) and with Tac* (test 2). The initial OCV from test 1 is lower than test 2 probably due to the mixed potential from the Tac* oxidation reaction. For test 1 without Tac*, the OCV decreases very rapidly in the first 24 hrs whereas the OCV decay is much slower for test 2. During the whole operation time, the OCV from test 2 is always higher than test one except the first 2 hrs. The boost of OCV is mainly due to the ability of TEMPO radical to decompose H_2O_2 in the membrane and avoid the H_2O_2 decomposition reaction at the cathode, which could decrease cathode potential. Although polarization curve was not tested, it can be expected that the fuel-cell performance can be improved by adding peroxide decomposition additives.

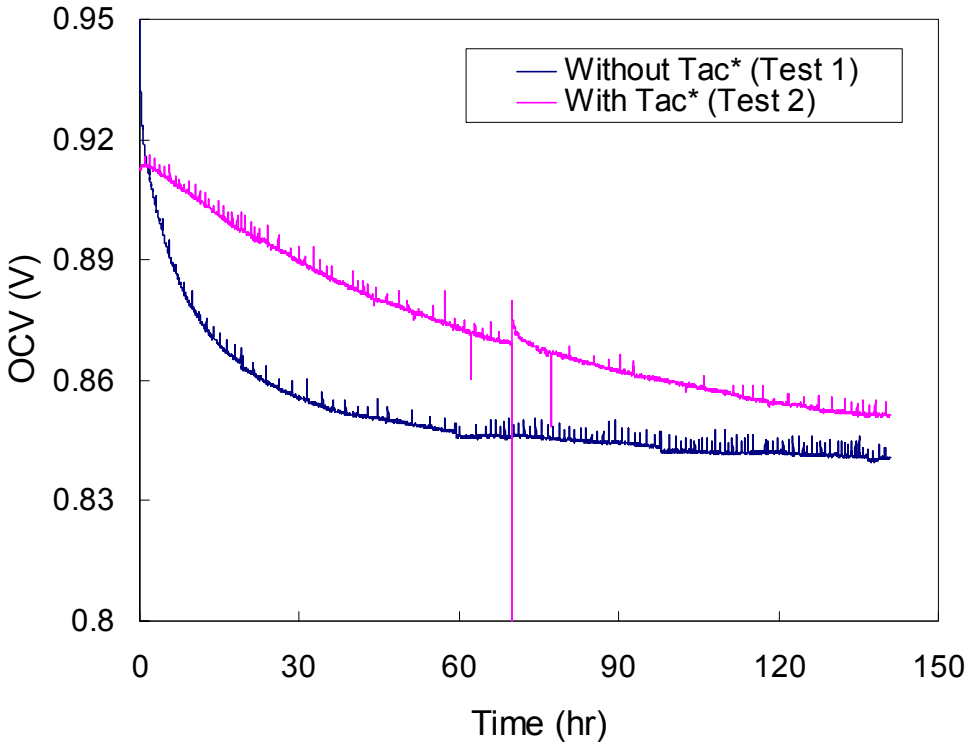

Figure 10.3. OCV curve during two tests.

10.2. FER study

Figure 10.4 shows the fluoride ion emission rate during two tests. In test 1 without Tac*, FER remained at a very high level over the whole test. However, for test 2 by addition of Tac* at cathode, the initial FER drops significantly to about one fifth compared to test 1. It indicates the decomposition of H_2O_2 and other radicals indeed helped to reduce fluoride ion emissions and mitigate membrane degradation. On the other hand, we confirmed that H_2O_2 formation and subsequent free radical formation can initiate and cause membrane degradation since we have the evidence that membrane degradation can be slowed down by decomposing H_2O_2 in the membrane. But the FER kept increasing after first 24 hrs and finally achieved the same level as test 1. The reason

may be due to the loss of Tac* or Tac^+ from the exhaust water. From UV measurement of exhaust water, trace amounts of Tac* were found but the concentration is extremely low. Since the initial amount added at cathode is also small, the loss can be significant after long time operation. Therefore, finding a way to constrain these additives inside the membrane is important in future peroxide decomposition additive studies. At the end of test 2, we tried to refill the same amount of Tac* at cathode side to see if we could reactivate the effect of peroxide decomposition reagent. However, the FER kept increasing and achieved almost the highest value in test 1. We call this phenomena "memory effect" in membrane degradation, which was also reported by Liu et al. with changing experimental sequence of gas partial pressures [46]. Two conclusions can be made based on this result: first, there is a process of generating weak structures during degradation that may have some relation with free radical attack; second, some oxidative species other than H_2O_2 and free radicals could also decompose membrane such as O_2 molecule that we have discussed in chapter 9.

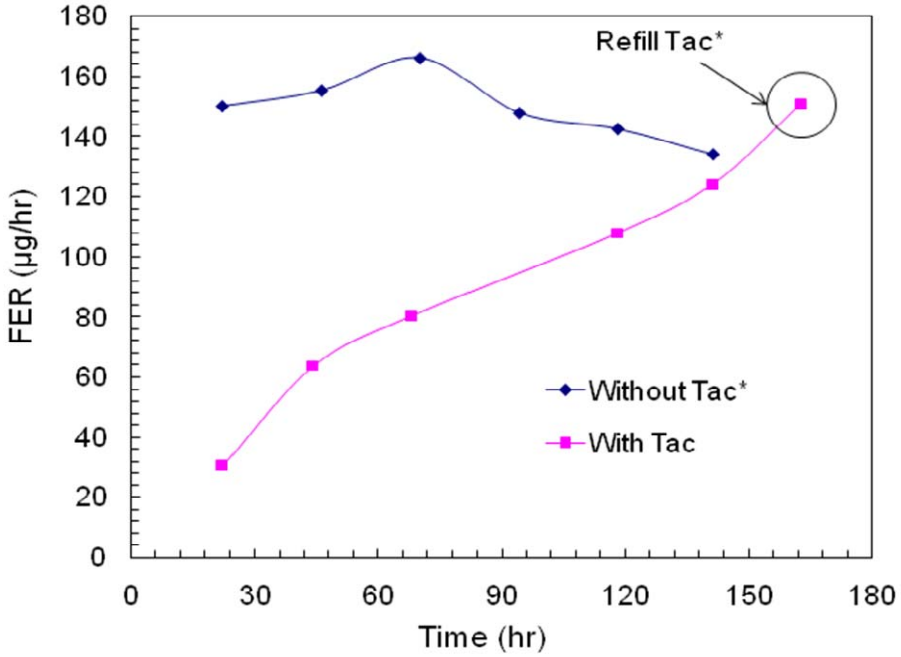

Figure 10.4. Comparison of FER during two tests.

10.3 TFA emission study

Figure 10.5 shows TFA emission rate from both anode and cathode during two tests. Both anode and cathode TERs show profiles similar to the fluoride ion emission rates. Since the TER can be considered as an indicator of side chain degradation, this results again confirms the strong relation between backbone decomposition and side chain degradation. A higher emission rate was observed from anode, indicating more severe membrane degradation there.

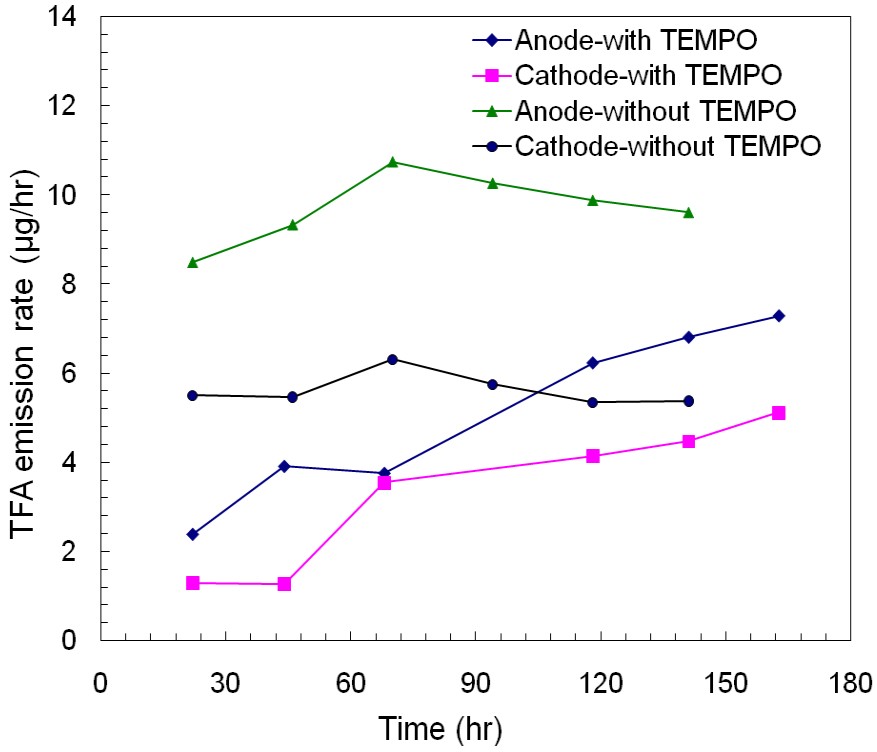

Figure 10.5. Comparison of TFA emission rate during two tests.

The molar ratio between generated HF and TFA was calculated to study the degradation mechanism with the addition of peroxide decomposition reagent. The ratio in test 2 is clearly higher than test 1, which means the addition of Tac* slows down the rate of side chain degradation and mitigates membrane degradation. It protects the side groups by decomposing some harmful oxidative species such as H_2O_2 and free radicals thereby less weak groups (such as -COOH) will be formed in the polymer. However, at the same time, other oxidative species such as O_2 molecule cannot be eliminated by Tac*. These species are only involved with main chain unzipping process and cannot attack the side chain. Since Tac* is lost with time during fuel-cell operation, the ratio decreases and the

amount of weak groups accumulates; finally, FER still increases even though Tac* was replenished.

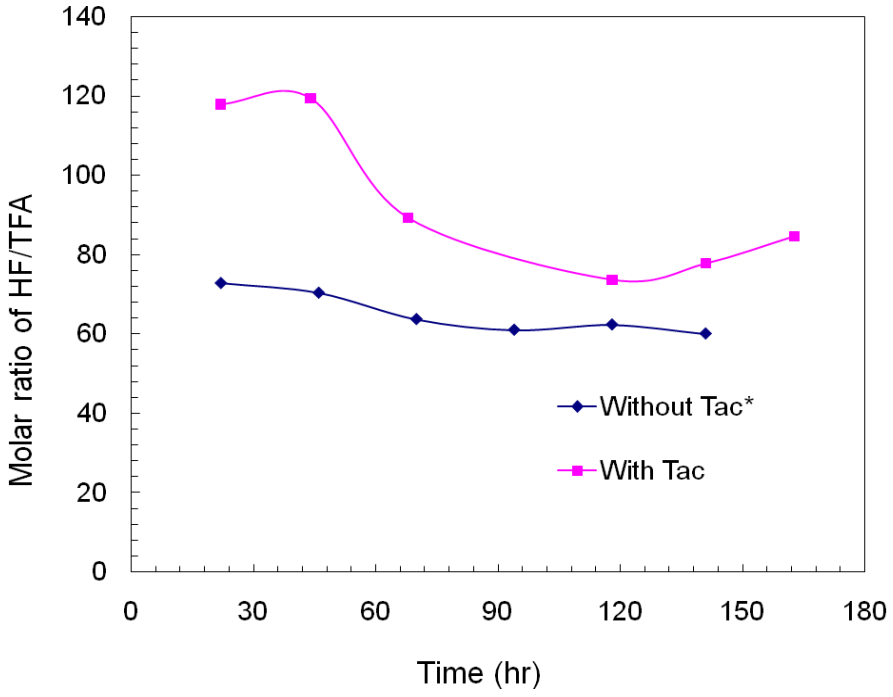

Figure 10.6. Molar ratio of HF/TFA during two tests.

10.4 Summary

TEMPO radical was used as peroxide decomposition reagent in this study. An increase in the OCV and a decrease in FERs were found after adding TEMPO radical at the cathode side. Nonetheless, the FER kept increasing during the test even after refill TEMPO radical and reached the same level as the test without peroxide decomposition reagent. This is mainly due to the loss of this additive with effluent water. Therefore, the primary effort that we could make is to find a better way to confine these additives in membrane under fuel-cell operation conditions. For example, we can ion-exchange Tac^+

into Nafion® membrane before test instead of doping at cathode; or we may be able to link such structure onto the polymer chain or make a composite membrane by blending peroxide decomposition reagent with polymer membrane.

CHAPTER 11

CONCLUSIONS AND RECOMMENDATIONS

11.1 Conclusions

Insufficient durability of the membrane electrolyte is a major impediment to the commercialization of PEMFC systems. Understanding its degradation mechanism is extremely important in developing more durably membrane materials. In this dissertation, a combination of experimental and simulation studies on membrane degradation mechanism is presented.

Fenton's test was first introduced as an initial screening method. After treatment in different Fenton's reagents, chemical changes in Nafion® membranes were analyzed by XPS and clear evidence of polymer degradation was observed. Exposure of the membrane to 2 hours of X-ray radiation did not affect the chemical structure of the membrane. However, treatment with various Fenton's reagents indicated that the $(CF_2)_n$ polymer backbone had decomposed. The increase in oxygen atom concentration suggests that oxygen-rich moieties formed in the membrane. These results indicated that in addition to degradation of the polymer side chain, chemical attack of the CF_2 backbone may be the primary reason for extensive fluorine loss and hydrogen crossover in membranes after long-term operation. FTIR spectra showed the formation of C=O and S-O-S in the degraded membrane. Two degradation schemes consistent with the results observed have been proposed. No detectable changes in XPS spectra were found between a fresh MEA and an MEA after long-term operation. These results suggest that

degradation occurred mainly within the membrane or at the membrane-electrode interface.

In-situ fuel-cell tests were conducted to study the effect of operating conditions such as relative humidity, oxygen partial pressure and temperature on membrane degradation by measuring FER from exhaust water. It was found that low relative humidity, high oxygen partial pressure and high temperature accelerated membrane degradation. By varying humidity at both the anode and cathode, it was determined that water transport can impact degradation and further that the anode side is more sensitive to changes in humidity than the cathode.

Since H_2O_2 was found to be at the root of membrane degradation, we designed a novel spectrophotometric method to quantitatively determine the H_2O_2 concentration in fuel cell by using a multilayer MEA. The effects of relative humidity and oxygen partial pressure on H_2O_2 concentration are discussed. H_2O_2 formation was found to be dependent on membrane thickness. H_2O_2 emission rates were measured in anode and cathode only MEAs to separately study H_2O_2 formation at each electrode. In addition, a model for H_2O_2 formation, transport, and reaction in PEMFCs is established for the first time to validate experimental data and study formation mechanism.

Profiles of oxygen and H_2O_2 concentration inside the fuel cell are simulated using the agglomerate model for the electrode. The predicted concentrations and emission rates of H_2O_2 show good agreement with experimental data. Low humidity, high temperature, and high oxygen/hydrogen partial pressures were found to increase the concentration of H_2O_2. An increase in membrane thickness or metal ion contaminant level reduces the concentration of H_2O_2 in the membrane. Lowering the oxygen permeability in the

ionomer is the most important and effective method to reduce the formation of H_2O_2. The simulation results also show little change in H_2O_2 concentration when operating the fuel cell above 0.6 V. Anodes designed with considerable thickness, high catalyst loadings and active areas can also help to suppress H_2O_2 formation. Recommendations are made to mitigate the effects of H_2O_2 and prolong membrane lifetimes.

Reactant humidity is critical to fuel-cell system design and also strongly affects the useable life of membrane separators. Accelerated fuel-cell durability tests were conducted under different levels of humidity. The emission rates of various degradation products such as HF, SO_4^{2-} and TFA were determined as a function of reactant humidity. Again, membrane degradation is accelerated at low humidity. The membranes become less conductive, more brittle and rigid after fuel-cell tests. An ATR-FTIR investigation showed that the decomposition of the ether group in the middle of side chain corresponds well with the detection of a TFA product. Thermogravimetric analysis demonstrated a decrease in thermal stability with lower humidity. Crack formation in degraded membrane was observed from SEM under low humidity. A membrane degradation model based on main chain unzipping process indicates that the degradation mechanism changes with humidity. Finally, the representative reaction pathway in each degradation scheme was postulated.

Furthermore, the fuel cell was operated under various temperatures to investigate the degradation mechanism. Degraded membranes were removed after each test for XPS analysis. Both the anode and cathode sides of degraded membranes were analyzed by XPS, and the results show that degradation was accelerated by high temperature and the decomposition of both sulfonic acid side chains and the PTFE backbone occurred. The

degradation was more severe on the anode side, showing that at least half of side groups were decomposed there. A multilayer MEA was also used to study degradation at different locations especially in the bulk membrane, which shows the degradation also occurs there, but is slower than at the anode side. This result also indicates that the rate of membrane degradation slows with thicker membrane. An improved kinetic model of membrane degradation was proposed to explain the experimental results.

Finally, TEMPO radicals were used as peroxide decomposition reagent to mitigate membrane degradation. An increase in OCV and a decrease in FER were found after adding the TEMPO radical at cathode side. However, FERs kept increasing during the test even after refill TEMPO radical and reached the same level as the test without peroxide decomposition reagent. Finding a better way to confine these additives into membrane under fuel-cell operation conditions will be a primary effort in developing these peroxide decomposition reagents.

11.2 Recommendations for future work

This dissertation addresses important fundamental understandings on membrane degradation in PEMFCs. A great deal of experimental data was obtained and degradation model was built based on experimental findings. However, as with all scientific research, additional questions are raised after one question was answered, and this project is no exception. Here, we recommend the following work for future study on membrane degradation.

In this study, almost all experiments were conducted under OCV condition and it would be interesting to study the effect of current density on membrane degradation since

fuel cell is operated with current loading in actual vehicular applications. Although it has been reported that FER decreases with the increase of current density [16], the detailed mechanism is still unclear and our modeling results show the current density has insignificant impact on H_2O_2 formation when cathode potential is above 0.6 V. In addition, proton transport electro-osmotically drags water from the anode [76], lowering the water content at the anode, and the degradation should be exacerbated under high current loadings.

Another important influence factor on membrane degradation is Pt^{2+} or even Pt band formed in Pt dissolution process. Especially the effect of Pt band is still under debate now. On one side, the existence of Pt may help to decompose H_2O_2 and mitigate degradation; on the other side, direct formation of reactive radical may occur on Pt catalyst and cause more severe degradation. However, it was found that the addition of Pt into the membrane could extend membrane life time in the reverse process of a fuel cell – a water electrolysis cell.

Some insight into the detail mechanism of side chain degradation needs to be explored, which could help to improve the kinetic model of membrane degradation proposed in this study and give a better prediction of degradation rate with known operation conditions and material properties. Also, the transient model of membrane degradation can be developed based on a better understanding of side chain degradation mechanism, for example, the –COOH group formation mechanism.

Micro FTIR and Raman spectroscopy are recommended for further development of spectroscopic techniques to study membrane degradation mechanism since *in-situ* degradation data of chemical structural change can be obtained. Combined with FER

data, a better understanding of membrane degradation can be achieved. Also, the water distribution and transport can be studied with these two techniques.

The degradation products in the exhaust water were analyzed as indicators of membrane degradation in this study. As indicated from degradation mechanism proposed by Dupont [4], another important product is CO_2, and it would be very helpful to study the generation of CO_2 to see if it matches the FER results. That being said, one difficulty is the interference from carbon corrosion process, where CO_2 is also produced. Here we suggest using Pt catalyst without carbon support to eliminate carbon corrosion and collect CO_2 emission data with a nondispersive infrared (NDIR) analyzer or gas chromatography (GC) combined with mass spectrometer (MS). Especially GC-MS is advantageous in this approach, because the detection limit is low for MS and the degradation mechanism can be studied by an isotope method, for example, using $^{18}O_2$ as cathode oxidant.

Also, the experimental and simulation methods developed in this dissertation can be used to study degradation mechanism of other fuel-cell membranes. For example, the H_2O_2 formation model is also applicable for fuel cell with other type of membranes. Since the details of membrane degradation mechanism are available for some hydrocarbon membranes [54, 124], the kinetic model of such membrane degradation process can be built to predict the lifetime and design better control strategies to mitigate degradation.

11.3 Recommendation for new membrane development

(1) Improve PFSA membrane structure

During our study, we found that the ether linkage in the middle of side chain of PFSA membranes such as Nafion® is vulnerable. Therefore, one way to improve the chemical stability of PFSA membranes is to eliminate this ether linkage and keep the other one such as 3M and Dow PFSA membranes [3]. However, another suggestion is to keep long side chain and add some CF_3 groups before the other C-O structure to mitigate free radical attack from water phase. Moreover, since some certain organic compound was found to be effective in decomposing H_2O_2 and free radicals, adding this kind of structure to PFSA polymer chain as a scavenger can greatly extend membrane lifetime. Compared with ion exchange or direct mixing method, this method can be much more effective by immobilizing these chemical compounds inside membrane.

(2) Composite membrane

Instead of changing the chemical structure of PFSA membranes, which can be troublesome in replacing existing manufacturing process, a composite membrane made by blending PFSA ionomers with other materials can be a better approach. A good example is Gore-select® membrane, developed by W. L. Gore [125]. They use a porous PTFE matrix which is filled with PFSA solution to achieve better chemical and mechanical stability induced by this PTFE matrix. For example, some hydrocarbon membranes have low O_2 permeability; however, their chemical and mechanical stabilities are not as good as PFSA membrane. Therefore, as shown in Figure 11.1, we could make a composite membrane by dissolving these two types of membranes together in the solvent and create a concentration gradient between them, and then evaporating the solvent out. The hydrocarbon membrane side will be used at cathode because it's a better

O_2 barrier. The PFSA membrane side will be used at anode since the H_2O_2 and free radicals are formed there and it has better chemical stability. The transition region can alleviate the incompatibility of two different materials. We could obtain the merits of both materials by doing this.

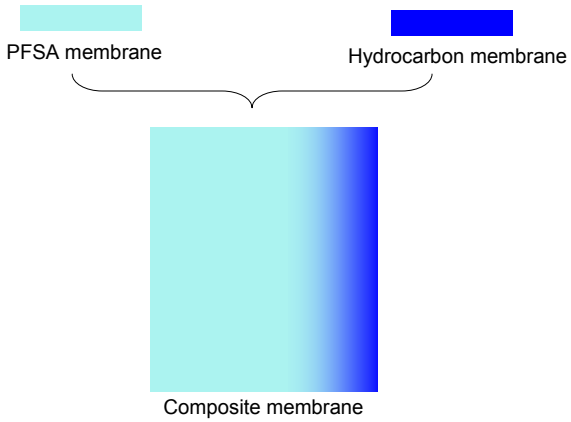

Figure 11.1. A composite membrane.

(3) New hydrocarbon membrane

New hydrocarbon membrane can be another option. As mentioned in chapter 7, decrease in O_2 diffusivity and solubility will be the best way to go. Adding more aromatic groups can decrease O_2 diffusivity such as BPSH [75]. However, compared with Nafion membrane, no significant decrease in the solubility of BPSH can be obtained. It is reported that the O_2 solubility in both PFSA and hydrocarbon membranes decrease under high humidity [75] and this is mainly due to the low solubility of O_2 in water. This is because water is highly polar but O_2 is a nonpolar molecule. Therefore, we could create some polar structures in the polymer chain such as –OH and -NH_2 groups to decrease O_2 solubility in the polymer. Another interesting finding in this work is that more straight

water channel in the polymer could help reduce H_2O_2 concentration in the membrane. Therefore, a rigid backbone by inserting more benzene rings and cross-linking is also recommended to enhance both chemical and thermal stability.

APPENDIX A

OXYGEN PERMEATION AND H_2O_2 FORMATION MODEL

A.1 Oxygen permeation model

For an ideal case when adsorption sites are totally covered by hydrogen, Equation (6) and (8) will be exactly the same. Under high hydrogen partial pressure, Equation (6) becomes:

$$R_{O2} = R_{H2O2}^{Formation} \simeq k_2 c_{O2} \frac{(K_{eq} c_{H2})^{1/2}}{(K_{eq} c_{H2})^{1/2} + 1} \approx k_2 c_{O2} \tag{A1}$$

$$k_2 = \frac{i_{O2}}{2F * A_C * c_{O2,ref} * (1 - \varepsilon_{CL})} (\frac{c_{H+}}{c_{H+,ref}})^2 \exp(\frac{-\alpha_{O2} F (E_a - E_{O2})}{RT}) \tag{A2}$$

Finally, the rate constant of O_2 reduction can be obtained:

$$k_C = \frac{i_{O2}}{2F * A_C * c_{O2,ref} * (1 - \varepsilon_{CL})} (\frac{c_{H+}}{c_{H+,ref}})^2 \exp(\frac{-\alpha_{O2} F (E_a - E_{O2})}{RT}) \frac{(K_{eq} c_{H2})^{1/2}}{(K_{eq} c_{H2})^{1/2} + 1} \tag{A3}$$

Here, we use agglomerate model to simulate O_2 reduction reaction inside anode. Followed the model description in the section 2.2, this process can be described by:

$$D_{O2,eff}^{agg} \frac{1}{r^2} \frac{d}{dr} \left(r^2 \frac{dc_{O2}}{dr} \right) = -k_C c_{O2} \tag{A4}$$

The effective diffusion coefficient inside the agglomerate is given by Bruggemann's relation [104]:

$$D_{O2,eff}^{agg} = D_{O2}^{M} \varepsilon_{agg}^{1.5} \tag{A5}$$

Equation 7.12 and symmetry provide boundary conditions, and the analytical solution of Equation 7.14 yields an effectiveness factor, E_r, for the reaction inside the agglomerate such that the oxygen reaction in catalyst layer is

$$R_{O2}^{agg} = -E_r k_C c_{O2,m/s} \tag{A6}$$

$$E_r = \frac{1}{\varphi_L}\left(\frac{1}{\tanh(3\varphi_L)} - \frac{1}{3\varphi_L}\right) \tag{A7}$$

$$\phi_L = \frac{r_{agg}}{3}\sqrt{\frac{k_C}{D_{O2,eff}^{agg}}} \tag{A8}$$

The mass balance of oxygen inside the agglomerate at steady state gives

$$\nabla \cdot N_{O2} - R_{O2}^{agg} = 0 \tag{A9}$$

The rate of reaction throughout the agglomerate is equal to the rate of diffusion through the surface of the agglomerates, *i.e.,*

$$\alpha_{agg} N_{O2}{}' = -R_{O2}^{agg} \tag{A10}$$

Where α_{agg} is effective agglomerate surface area (we use $3/r_{agg}$ here)

Then we can easily derive

$$E_r k_C c_{O2,m/s} = D_{O2}^{M} \frac{\alpha_{agg} r_{agg}}{r_{agg} + \delta_{agg}} \frac{c_{O2,g/m} - c_{O2,m/s}}{\delta_{agg}} \tag{A11}$$

Let $D_{O2}^{M} \dfrac{\alpha_{agg} r_{agg}}{\delta_{agg}(r_{agg} + \delta_{agg})} = X, E_r k_C = Y$

$$R_{O2} = -(1-\varepsilon_{CL}) E_r k_C \frac{X}{X+Y} c_{O2,g/m} \tag{A12}$$

$$k_{O2} = (1-\varepsilon_{CL}) E_r k_C \frac{X}{X+Y} \frac{RT}{H_{O2,m}} \tag{A13}$$

Finally, oxygen concentration profile can be expressed as:

$$\text{In GDL, } c_{O2} = B_1 z + B_2 \tag{A14}$$

$$N_{O2} = -D_{O2,\,eff}^{GDL} \frac{dc_{O2}}{dz} = -D_{O2,\,eff}^{GDL} B_1 \tag{A15}$$

In anode electrode, $c_{O2} = B_3 \sinh(z\sqrt{k_{O2} / D_{O2,eff}^{CL}}) + B_4 \cosh(z\sqrt{k_{O2} / D_{O2,eff}^{CL}})$ (A16)

$$N_{O2} = -D_{O2,eff}^{CL} \frac{dc_{O2}}{dz} = -\sqrt{k_{O2} D_{O2,eff}^{CL}} (B_3 \cosh(z\sqrt{k_{O2} / D_{O2,eff}^{CL}}) + B_4 \sinh(z\sqrt{k_{O2} / D_{O2,eff}^{CL}}))$$

(A17)

In membrane, $c_{O2} = B_5 z + B_6$ (A18)

$$N_{O2} = -D_{O2,\,eff}^{M} \frac{dc_{O2}}{dz} = -D_{O2,\,eff}^{M} B_5 \quad \text{(A19)}$$

H_2O_2 formation model

The ratio between effective H_2O_2 diffusion coefficient in ionomer membrane and in water can be related by Prager's model [126, 127]:

$$\frac{D_{H2O2}^{L} \varepsilon_{H2O}}{D_{H2O2,eff}^{M}} = \frac{2(1-\varepsilon_{H2O}) + 2\varepsilon_{H2O} \ln \varepsilon_{H2O} - 0.5\varepsilon_{H2O} (\ln \varepsilon_{H2O})^2}{\varepsilon_{H2O}(1-\varepsilon_{H2O}) + \varepsilon_{H2O}{}^2 \ln \varepsilon_{H2O}} \quad \text{(A20)}$$

where $\varepsilon_{H2O} = \dfrac{0.0336 * \lambda}{1 + 0.0336 * \lambda}$

Similarly, H_2O_2 production and decomposition inside electrode can be also described by agglomerate model:

$$D_{H2O2,eff}^{agg} \frac{1}{r^2} \frac{d}{dr} \left(r^2 \frac{dc_{H2O2}}{dr} \right) = -k_{C,H2O2}^{Anode} c_{H2O2} + k_C c_{O2} \quad \text{(A21)}$$

Combine with Equation A7:

$$D_{H2O2,eff}^{agg} \frac{1}{r^2} \frac{d}{dr} \left(r^2 \frac{d(c_{H2O2} + \theta c_{O2})}{dr} \right) = -k_{C,H2O2}^{Anode} (c_{H2O2} + \theta c_{O2}) \quad \text{(A22)}$$

where $\theta = \dfrac{k_C}{\dfrac{D_{H2O2,eff}^{agg}}{D_{O2,eff}^{agg}} k_C - k_{C,H2O2}^{Anode}}$

Therefore, we have

$$-D_{H2O2,eff}^{agg}\frac{d(c_{H2O2}+\theta c_{O2})}{dr}\alpha_{agg}=-E_{r,H2O2}k_{C,H2O2}^{Anode}(c_{H2O2}+\theta c_{O2}) \tag{A23}$$

$$R_{H2O2}^{agg}=-E_{r,H2O2}k_{C,H2O2}^{Anode}c_{H2O2}+\theta(\frac{D_{H2O2,eff}^{agg}E_r k_C}{D_{O2,eff}^{agg}}-E_{r,H2O2}k_{C,H2O2}^{Anode})c_{O2} \tag{A24}$$

$$\text{Assume } k_{O2}{}' =\theta(\frac{D_{H2O2,eff}^{agg}E_r k_C}{D_{O2,eff}^{agg}}-E_{r,H2O2}k_{C,H2O2}^{Anode})*(1-\varepsilon_{CL}) \tag{A25}$$

$$\text{Then } R_{H2O2}^{agg}=-E_{r,H2O2}k_{C,H2O2}^{Anode}c_{H2O2}+\frac{k_{O2}{}'}{1-\varepsilon_{CL}}c_{O2} \tag{A26}$$

Using porous electrode model, since H_2O_2 can transport through both ionomer and gas pore regions, the total flux will be:

$$N_{H2O2}=\varepsilon_{CL}N_{H2O2}^{Pore}+f_m*(1-\varepsilon_{CL})N_{H2O2}^{Polymer} \tag{A27}$$

The effective diffusion coefficient in catalyst layer is

$$D_{H2O2,eff}^{CL}=D_{H2O2}^{G}\varepsilon_{CL}^{1.5}K_{H2O2}+f_m*(1-\varepsilon_{CL})D_{H2O2,eff}^{M} \tag{A28}$$

Similarly, the H_2O_2 concentration profile inside MEA can be calculated as:

At anode,

$$c_{H2O2}=C_3\sinh(z\sqrt{k_1/D_{H2O2,\,eff}^{CL}})+C_4\cosh(z\sqrt{k_1/D_{H2O2,\,eff}^{CL}})+\frac{K_{O2}^{Anode}B_3}{(k_1-D_{H2O2,\,eff}^{CL}k_{O2}/D_{O2,eff}^{CL})}\sinh(z\sqrt{k_{O2}/D_{O2,eff}^{CL}})+\frac{K_{O2}^{Anode}B_4}{(k_1-D_{H2O2,\,eff}^{CL}k_{O2}/D_{O2,eff}^{CL})}\cosh(z\sqrt{k_{O2}/D_{O2,eff}^{CL}}) \tag{A29}$$

$$N_{H2O2}=-D_{H2O2,\,eff}^{CL}\frac{dc_{H2O2}}{dz}=-\sqrt{k_1D_{H2O2,\,eff}^{CL}}(C_3\cosh(z\sqrt{k_1/D_{H2O2,\,eff}^{CL}})+C_4\sinh(z\sqrt{k_1/D_{H2O2,\,eff}^{CL}}))$$
$$-D_{H2O2,\,eff}^{CL}\sqrt{k_{O2}/D_{O2,eff}^{CL}}[\frac{K_{O2}^{Anode}B_3}{(k_1-D_{H2O2,\,eff}^{CL}k_{O2}/D_{O2,eff}^{CL})}\cosh(z\sqrt{k_{O2}/D_{O2,eff}^{CL}})+\frac{K_{O2}^{Anode}B_4}{(k_1-D_{H2O2,\,eff}^{CL}k_{O2}/D_{O2,eff}^{CL})}\sinh(z\sqrt{k_{O2}/D_{O2,eff}^{CL}})]$$

(A30)

In the membrane,

$$c_{H2O2} = C_5 \sinh(z\sqrt{k_2 / D^M_{H2O2,eff}}) + C_6 \cosh(z\sqrt{k_2 / D^M_{H2O2,eff}}) \quad \text{(A31)}$$

$$N_{H2O2} = -D^M_{H2O2,eff} \frac{dc_{H2O2}}{dz} = -\sqrt{k_2 D^M_{H2O2,eff}} (C_5 \cosh(z\sqrt{k_2 / D^M_{H2O2,eff}}) + C_6 \sinh(z\sqrt{k_2 / D^M_{H2O2,eff}})) \quad \text{(A32)}$$

At cathode,

$$c_{H2O2} = C_7 \sinh[(z - l_2)\sqrt{k_3 / D^{CL}_{H2O2,\,eff}}] + C_8 \cosh[(z - l_2)\sqrt{k_3 / D^{CL}_{H2O2,\,eff}}] \quad \text{(A33)}$$

$$N_{H2O2} = -D^{CL}_{H2O2,\,eff} \frac{dc_{H2O2}}{dz} = -\sqrt{k_3 D^{CL}_{H2O2,\,eff}} (C_7 \cosh((z - l_2)\sqrt{k_3 / D^{CL}_{H2O2,\,eff}}) + C_8 \sinh((z - l_2)\sqrt{k_3 / D^{CL}_{H2O2,\,eff}})) \quad \text{(A34)}$$

Boundary conditions

At interface between different layers, equal mass fluxes and concentrations or Henry's Law was applied to establish boundary conditions.

At interface between GDL and gas flow channel, an average mass transfer coefficient was used to relate the bulk flow and mass transport on the surface of GDL.

Boundary conditions at the interface between GDL and gas channel:

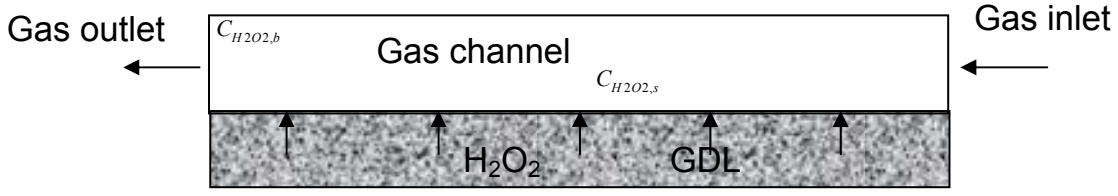

Figure A.1. Boundary conditions at the interface between GDL and gas channel.

For a rectangular conduit with one insulated side, the Nusselt number for fully developed laminar flow is 5.39 (uniform heat flux) and 4.86 (uniform surface temperature). Using analogy between heat transfer and mass transfer, we use the average Sherwood number here for our system, which is

$$\frac{K_c D_h}{D_{H2O2}} = \frac{5.39 + 4.86}{2} = 5.125 \tag{A35}$$

where K_C is mass transfer coefficient, $D_h=4A_C/P$ is effective diameter, D_{H2O2} is H_2O_2 diffusion coefficient in gas phase. Therefore, another boundary condition can be established using mass balance:

$$N_{H2O2} = K_c(C_{H2O2,S} - C_{H2O2,b}) = S * C_{H2O2,b} \tag{A36}$$

In fact, the mass transfer coefficient at the boundary doesn't have a significant impact on the H_2O_2 concentration inside membrane. From modeling results, the H_2O_2 concentration at GDL and gas channel boundary is always close to 0 and it makes sense because it's difficult to collect H_2O_2 in the exhaust water during fuel-cell operation. However, this boundary condition would be important while calculating the emission rate of HF and other chemical species.

APPENDIX B

KINETIC MODEL OF MEMBRANE DEGRADATION

Apply the stationary state assumption, which means all the radical concentrations are constant:

$$0 = \frac{d[\cdot OH]}{dt} = k_1[Fe^{2+}][H_2O_2] - k_2[Rf - CF_2COOH][\cdot OH] - k_3[Rf - CF_2\cdot][\cdot OH] \quad \text{(B1)}$$

$$0 = \frac{d[Rf - CF_2\cdot]}{dt} = k_2[Rf - CF_2COOH][\cdot OH] - k_3[Rf - CF_2\cdot][\cdot OH] - k_4[Rf - CF_2\cdot][O_2] + k_6[Rf - CF_2O\cdot] \quad \text{(B2)}$$

$$0 = \frac{d[Rf - CF_2O\cdot]}{dt} = 2k_5[Rf - CF_2OO\cdot]^2 - k_6[Rf - CF_2O\cdot] \quad \text{(B3)}$$

$$0 = \frac{d[Rf - CF_2OO\cdot]}{dt} = k_4[Rf - CF_2\cdot][O_2] - 2k_5[Rf - CF_2OO\cdot]^2 \quad \text{(B4)}$$

The following equations can be derived:

$$k_1[Fe^{2+}][H_2O_2] = 2k_2[Rf - CF_2COOH][\cdot OH] \quad \text{(B5)}$$

$$k_2[Rf - CF_2COOH] = k_3[Rf - CF_2\cdot] \quad \text{(B6)}$$

$$k_4[Rf - CF_2\cdot][O_2] = 2k_5[Rf - CF_2OO\cdot]^2 = k_6[Rf - CF_2O\cdot] \quad \text{(B7)}$$

Finally, the HF generation rate expression is:

$$\begin{aligned} \frac{d[HF]}{dt} &= 2k_2[Rf - CF_2COOH][\cdot OH] + 2k_6[Rf - CF_2O\cdot] \\ &= k_1[Fe^{2+}][H_2O_2] + 2k_4[Rf - CF_2\cdot][O_2] \\ &= k_1[Fe^{2+}][H_2O_2] + \frac{2k_4k_2}{k_3}[Rf - CF_2COOH][O_2] \end{aligned} \quad \text{(B8)}$$

The $[Rf - CF_2COOH]$ in the above equation can be calculated from side chain reaction:

$$\frac{d[Rf-CF_2COOH]}{dt} = 2k_8[Rf-CF_2SO_3H][X] - 2k_7[Rf-CF_2\cdot]^2$$
$$= k_8[Rf-CF_2SO_3H][X] - 2k_7(\frac{k_2[Rf-CF_2COOH]}{k_3})^2 \quad \text{(B9)}$$

Under steady state, the formation rate of $[Rf-CF_2COOH]$ is 0:

$$[Rf-CF_2COOH] = \frac{k_3}{k_2}(\frac{k_8}{2k_7}[Rf-CF_2SO_3H][X])^{1/2} \quad \text{(B10)}$$

APPENDIX C

MEMBRANE DURABILITY TEST PROTOCOL

C.1. Cell assembling

Since using gas diffusion electrode (GDE) instead of gas diffusion layer and catalyst coating will be much more convenient in removing membrane from MEA, here we assemble two GDEs and one Nafion® 112 membrane together into the fuel cell hardware before conducting durability test on fuel-cell test station.

(1) Cut one 8 × 8 cm^2 Nafion® 112 membrane and two 5 × 5 cm^2 GDEs.

(2) Assemble membrane, GDEs and gaskets onto fuel cell hardware.

(3) Connect fuel-cell hardware to the fuel cell test station.

One of the important parameters in a cell build is the thickness of the gaskets because the gasket thickness determines how good the contact between GDL and gas flow field. A good contact (low resistance) is important for fuel-cell performance. Therefore, it is essential that the ribs of the flow fields bite into the electrode providing good contact as shown in Figure C.1. Typical pinch values are 2-3 mils (0.002–0.003 inch) for a carbon paper backing and 10-15 mils for a carbon cloth backing.

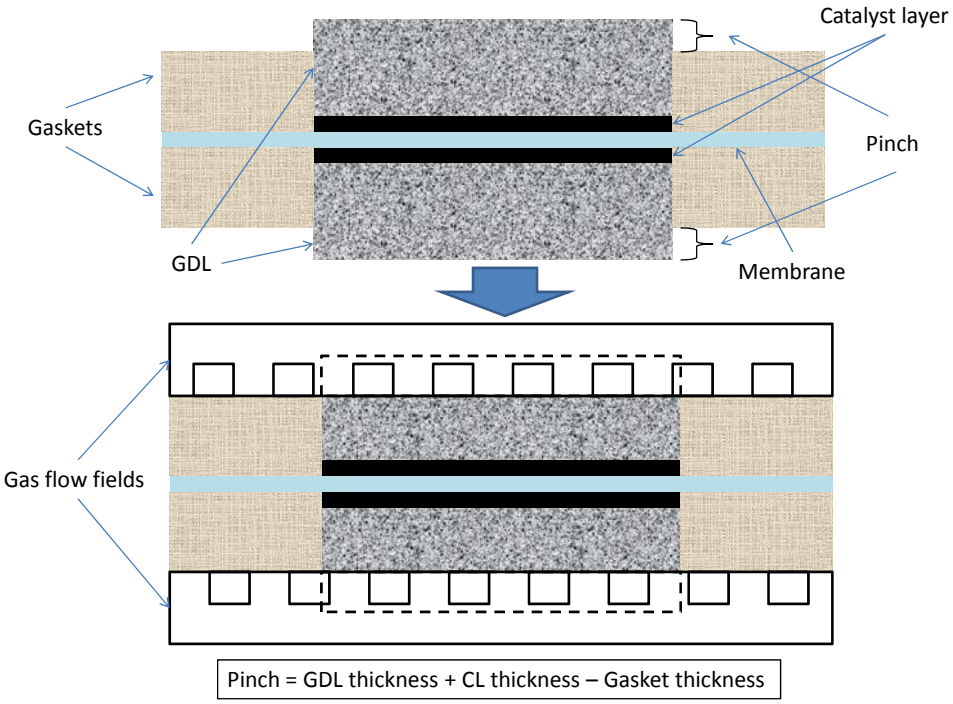

Figure C.1. A schematic diagram of pinch calculation.

C.2. Cell Start-up Procedures

C.2.1 Cell wet-up

The first step in the start-up sequence is to wet-up the MEA in order to hydrate membrane to its maximum water absorption capacity. First set cell temperature at 65 °C. Cathode humidifier temperature is set at 65 °C and anode humidifier temperature at 70 °C (5 °C above cell temperature). Set both anode and cathode flow rate to be 0.3 dm3/min. Without applying fuel, wait the system to warm up and reach the temperature set point. Continue flushing the system for 30 minutes with N_2. Then apply fuel and run the cell under OCV for 1 hour and decrease the anode saturator temperature to 65°C. Run the cell at OCV for another 1 hour.

C.2.2 Fuel crossover check

Hydrogen fuel diffused from anode to cathode will react with oxidant, which results in cell voltage loss. To check fuel crossover, shut off air supply (set air flow rate as zero) while maintaining hydrogen flow rate. Prevent external air entry by closing air effluent exit using Teflon tape. Or leave the air effluent tube end open if the tube is small and long. Monitor the open circuit voltage (OCV) for 10 minutes. If OCV continues dropping to zero, it indicates a gas crossover. No further fuel-cell test should be done before significant fuel crossover eliminated. Also, a H_2 detector (TIF 8800A) will be used to check for the leaking of hydrogen within the assembled fuel cell hardware.

C.2.3. Break-in procedure

Constant voltage or constant current break-in procedure is commonly applied to condition cell. Here constant current method is used for cell conditioning in the experiment.

Apply a small initial current density of 50 mA/cm^2 and then incrementally increase the current density to 200 mA/cm^2 (or 5 A), 500 mA/cm^2 (or 12.5 A), and finally 800 mA/cm^2 (or 20 A). Each current hold period is 5 hrs, which gives a total of 20 hrs cell conditioning. Fuel and air flow rates are load based and calculated as followings:

Fuel (pure H_2) = 0.3 L/min + 0.0385 (L/min/A) * Current (A)

Air = 0.3 L/min + 0.1464 (L/min/A) * Current (A)

Finally run the cell at open circuit for 10 minutes.

APPENDIX D

MEA FABRICATION PROCEDURE

D.1. Sample ink preparation

Table D.1 shows the properties of sample ink. Note that "Spraying Factor" is used to adjust for ink losses during spraying.

Table D.1 Ink properties.

Wt% Ionomer in solution	0.05	Wt% Pt/Support	0.40
Wt% IPA	1.00	Cell area (cm^2)	25.00
IPA (solvent%)	0.60	Target anode loading (mg Pt/cm^2)	0.30
g solid / g liquid	0.05	Target cathode loading (mg Pt/cm^2)	0.30
Spraying factor	5.00	Ionomer/support wt ratio	0.80

For the above ink properties, the coating parameters can be calculates in Table D.2. Then weigh the calculated amount of each component of the ink and mix them together followed by this sequence: catalyst, DI water, ionomer solution, and finally IPA. The mixture was sonicated for 5 minutes at the lowest power setting.

Table D.2. Adjustable Coating Parameters

Ink solution	
Catalyst Weight (mg)	187.50
DI Water Weight (mg)	510.00
Ionomer Solution (mg)	1800.00
IPA Weight (mg)	3330.00
Total Anode Weight (mg)	27.75
Total Cathode Weight (mg)	27.75

D.2 Decal Transfer Method

The ink is painted onto two 3 × 3 inches of the 2 mil Teflon™ sheets (one sheet for each side). Spray the sample by airbrush starting from the top left and proceeding horizontally across the Teflon™ sheet, changing directions and spraying lower on each consecutive pass. It is also important to change directions while not spraying the sample to ensure an even coat. Multiple coats are applied till achieve desired catalyst loading. The Teflon™ sheets are placed on preheated hotplate at 150 ^{o}C to dry the coatings.

Then a 3 × 3 inches Nafion® 112 membrane is sandwiched between two coated TeflonTM sheets and hot pressed between 140 and 160 ^{o}C at 1700 kPa for six minutes. After the sample has been removed and cooled down, the two Teflon sheets can gently be pulled away, and the MEA should be ready to use.

D.3. CCM (Catalyst Coated Membrane) Method

This method is to directly paint the ink onto Nafion® membrane surface. The whole procedure is similar to Decal Transfer method. No hot pressing procedure is needed.

REFERENCES

[1] V. Stamenkovic, B.N. Grgur, P.N. Ross and N.M. Markovica, J. Electrochem. Soc., 152 (2005) A277.

[2] L. Merlo, A. Ghielmi, L. Cirillo, M. Gebert and V. Arcella, J. Power Sources, 171 (2006) 140.

[3] S.J. Hamrock and M.A. Yandrasits, Journal of Macromolecular Science, Part C: Polymer Reviews, 46 (2006) 219.

[4] D.E. Curtin, R.D. Lousenberg, T.J. Henry, P.C. Tangeman and M.E. Tisack, J. Power Sources, 131 (2004) 41.

[5] A. Mahreni, A.B. Mohamad, A.A.H. Kadhum, W.R.W. Daud and S.E. Iyuke, J. Membr. Sci., 327 (2009) 32.

[6] R. Kannan, B.A. Kakade and V.K. Pillai, Angewandte Chemie International Edition, 47 2653.

[7] S. Sambandam and V. Ramani, J. Power Sources, 170 (2007) 259.

[8] Q. Li, R. He, J.O. Jensen and N.J. Bjerrum, Fuel Cells, 4 (2004) 147.

[9] W.G. Grott, Macromol. Symp., 82 (1994) 161.

[10] G.A. Olah, G.K.S. Prakash and J. Sommer, Science, 206 (1979) 13.

[11] K. Osseo-Asare and T. Xue, J. Membrane Sci., 43 (1989) 5.

[12] C. Heitner-Wirguin, J. Membrane Sci., 120 (1996) 1.

[13] http://www.fuelcells.dupont.com/.

[14] M. Mathias, H. Gasteiger, R. Makharia, S. Kocha, T. Fuller, T. Xie and J. Pisco, Preprints of Symposia - American Chemical Society, Division of Fuel Chemistry, 49 (2004) 471.

[15] T.A. Zawodzinski, C. Derouin, S. Radzinski, R.J. Sherman, V.T. Smith, T.E. Springer and S. Gottesfel, J. Electrochem. Soc., 140 (1993) 1041.

[16] V.O. Mittal, H.R. Kunz and J.M. Fenton, J. Electrochem. Soc., 153 (2006) A1755.

[17] Y. Shao, G. Yin, Z. Wang and Y. Gao, J. Power Sources, 167 (2007) 235.

[18] W. Bi, G.E. Gray and T.F. Fuller, Electrochem. Solid-state Lett., 10 (2007) B101.

[19] N. Takeuchi and T.F. Fuller, J. Electrochem. Soc., 155 (2008) B770.

[20] W. Bi and T.F. Fuller, J. Electrochem. Soc., 155 (2008) B215.

[21] T.F. Fuller and G. Gray, ECS Trans., 345 (2006) 1.

[22] E. Endoh, S. Terazono, H. Widjaja and Y. Takimoto, Electrochem. Solid-state Lett., 7 (2004) A209.

[23] A.B. LaConti, M. Hamdan and R.C. McDonald, in W. Vielstich, A. Lamm and H.A. Gasteiger (Editors), Handbook of Fuel Cells: Fundamentals Technology and Applications, Vol. 3, John Wiley & Sons Ltd, Chichester, 2003, p. 647.

[24] C. Chen and T.F. Fuller, Electrochim. Acta, 54 (2009) 3984.

[25] K. Teranishi, K. Kawata, S. Tsushima and S. Hirai, Electrochem. Solid-State Lett., 9 (2006) 475.

[26] C. Chen and T.F. Fuller, Polym. Degrad. Stab., accepted (2009).

[27] T. Kinumoto, M. Inaba, Y. Nakayama, K. Ogata, R. Umebayashi, A. Tasaka, Y. Iriyama, T. Abe and Z. Ogumi, J. Power Sources, 158 (2006) 1222.

[28] D.A. Schiraldi, Journal of Macromolecular Science, Part C: Polymer Reviews, 46 (2006) 315.

[29] T. Xie and C.A. Hayden, Polymer, 48 (2007) 5497.

[30] C. Huang, K.S. Tan, J. Lin and K.L. Tan, Chem. Phys. Lett., 371 (2003) 80.

[31] J. Yu, T. Matsuura, Y. Yoshikawa, M.N. Islam and M. Hori, Phys. Chem. Chem. Phys., 7 (2005) 373.

[32] V.O. Mittal, H.R. Kunz and J.M. Fenton, J. Electrochem. Soc., 154 (2007) B652.

[33] V.V. Atrazhev, E.N. Timokhina, S.F. Burlatsky, V.I. Sultanov, T.H. Madden and M. Gummalla, 211th Meeting of the Electrochemical Society - Meeting Abstracts, 701 (2007) 107.

[34] C. Chen, G. Levitin, D.W. Hess and T.F. Fuller, J. Power Sources, 169 (2007) 288.

[35] N.E. Cipollini, ECS Trans. , 11 (2007) 1071.

[36] W. Liu and D. Zuckerbrod, J. Electrochem. Soc., 152 (2005) 1165.

[37] C. Chen and T.F. Fuller, ECS Trans., 11 (2007) 1127.

[38] J. Qiao, M. Saito, K. Hayamizu and T. Okada, J. Electrochem. Soc., 153 (2006) A967.

[39] J. Healy, C. Hayden, T. Xie, K. Olson, R. Waldo, M. Brundage, H. Gasteiger and J. Abbott, Fuel Cells, 5 (2005) 302.

[40] S. Kundu, L.C. Simon and M.W. Fowler, Polym. Degrad. Stab., 93 (2008) 214.

[41] D.W. Rhoades, M.K. Hassan, S.J. Osborn, R.B. Moore and K.A. Mauritz, J. Power Sources, 172 (2007) 72.

[42] W.E.Delaney and W.K. Liua, ECS Trans., 11 (2007) 1093.

[43] F. Wang, M. Hichner, Y. Kim, Z. T and J. McGrath, J. Membr. Sci., 197 (2002) 231.

[44] M. Aoki, H. Uchida and M. Watanabe, Electrochem. Commun., 8 (2006) 1509.

[45] M. Inaba, T. Kinumoto, M. Kiriake, R. Umebayashi, A. Tasaka and Z. Ogumi, Electrochimica Acta, 51 (2006) 5746.

[46] H. Liu, J. Zhang, F.D. Coms, W. Gu, B. Litteer and H.A. Gasteiger, ECS Trans., 3 (2006) 493.

[47] V.O. Mittal, H. Russell Kunz and J.M. Fenton, Electrochem. Solid-State Lett., 9 (2006) 299.

[48] M.S. Sulek, S.A. Mueller and C.H. Paik, Electrochem. Solid-State Lett., 11 (2008) B79.

[49] E. Endoh, S. Hommura, S. Terazono, H. Widjaja and J. Anzai, ECS Trans., 11 (2007) 1083.

[50] A. Ohma, S. Suga, S. Yamamoto and K. Shinohara, J. Electrochem. Soc., 154 (2007) B757.

[51] A. Bosnjakovic and S. Schlick, J. Phys. Chem. B, 108 (2004) 4332.

[52] A. Panchenko, H. Dilger, J. Kerres, M. Hein, A. Ullrich, T. Kaz and E. Roduner, Phys. Chem. Chem. Phys., 6 (2004) 2891.

[53] A. Panchenko, H. Dilger, E. Möller, T. Sixt and E. Roduner, J. Power Sources, 127 (2004) 325.

[54] G. Hubner and E. Roduner, J. Mater. Chem., 9 (1999) 409.

[55] E. Endoh, ECS Trans., 16 (2008) 1229.

[56] F.D. Coms, ECS Trans., 16 (2008) 235.

[57] C. Zhou, M.A. Guerra, Z.-M. Qiu, T.A. Zawodzinski and D.A. Schiraldi, Macromolecules, 40 (2007) 8695.

[58] N. Ramasewamy, N. Hakim and S. Mukerjee, Electrochim. Acta, 53 (2008) 3279.

[59] C. Meredith, P. Zapata, K. Reed and P. Basak, Polymer Preprints, 47 (2006) 487.

[60] J.-L. Sormana and J.C. Meredith, Macromolecules, 37 (2004) 2186.

[61] K. Kodama, F. Miura, N. Hasegawa, M. Kawasumi and Y. Morimoto, 208th Meeting of the Electrochemical Society - Meeting Abstracts, (2005) 1185.

[62] J. Kiwi, N. Denisov, Y. Gak, N. Ovanesyan, P. Buffat, E. Suvorova, F. Gostev, A. Titov, O. Sarkisov, P. Albers and V. Nadtochenko, Langmuir, 18 (2002) 9054.

[63] S. Parra, I. Guasaquillo, O. Enea, E. Mielczarski, J. Mielczarki, P. Albers, L. Kiwi-Minsker and J. Kiwi, J. Phys. Chem. B, 107 (2003) 7026.

[64] M. Schulze, M. Lorenz, N. Wagner and E. Gülzow, Fresenius J Anal Chem, 365 (1999) 106.

[65] M. Laporta, M. Pegoraro and L. Zanderighi, Phys. Chem. Chem. Phys., 1 (1999) 4619.

[66] A. Gruger, A. Regis, T. Schmatko and P. Colomban, Vib. Spectrosc., 26 (2001) 215.

[67] R. Iwamoto, K. Oguro, M. Sato and Y. Iseki, J. Phys. Chem. B, 106 (2002) 6973.

[68] Y. Wang, Y. Kawano, S. Aubuchon and R. Palmer, Macromolecules, 36 (2003) 1138.

[69] V. Vacque, B. Sombret, J. Huvenne, P. Legrand and S. Suc, Spectrochimica Acta Part A, 53 (1997) 55.

[70] A. Alentiev, J. Kostina and G. Bondarenko, Desalination, 200 (2006) 32.

[71] M. Pianca, E. Barchiesi, G. Esposto and S. Radice, Journal of Fluorine Chemistry, 95 (1999) 71.

[72] S. Hommura, K. Kawahara, T. Shimohira and Y. Teraoka, J. Electrochem. Soc., 155 (2008) A29.

[73] C.A. Wilkie, J.R. Thomsen and M.L. Mittleman, J. Appl. Poly. Sci., 42 (1991) 901.

[74] D.R. Morris and X. Sun, J. Appl. Polymer Sci., 50 (1993) 1445.

[75] Y. Takamura, E. Nakashima, H. Yamada and M. Inaba, ECS Trans., 16 (2008) 881.

[76] T.F. Fuller and J. Newman, J. Electrochem. Soc., 140 (1993) 1218.

[77] C.E. Huckaba and F.G. Keyes, J. Am. Chem. Soc., 70 (1948) 1640.

[78] C.T. Kingzctt, J. Chem. Soc., 37 (1880) 792.

[79] P.A. Tanner and A.Y.S. Wong, Anal. Chim. Acta, 370 (1998) 279.

[80] H. Wang and S.-M. Park, Anal. Chem., 79 (2007) 240.

[81] B. Demirata-Oztiirk, G. Ozen, H. Filik, I. Tor and H. Afsar, J. Fluoresc., 8 (1998) 185.

[82] M. Feng, Z. Li, J. Lu and H. Jiang, Mikrochim. Acta, 126 (1997) 73.

[83] H. Gallati, J. Clin. Chem. Clin. Biochem., 17 (1979) 1.

[84] Y. Yamaguchi, H. Uenoyama, M. Yagi and X. Dou, U. S. Patent, Vol. 5,753,449, May 19, 1998.

[85] M.S. Lin and B.I. Jan, Electroanalysis, 9 (1997) 340.

[86] N.V. Klassen, D. Marchington and H.C.E. McGowan, Anal. Chem., 66 (1994) 2921.

[87] X.-S. Chai, Q.X. Hou, Q. Luo and J.Y. Zhu, Anal. Chim. Acta, 507 (2004) 281.

[88] A.O. Allen, C.J. Hochanadel, J.A. Ghormley and T.W. Davis, J. Phys. Chem., 56 (1952) 575.

[89] T.C.J. Ovenston and W.T. Rees, Analyst, 75 (1950) 204.

[90] T.A. Zawodzinski, T.E. Springer, F. Uribe and S. Gottesfeld, Solid State Ionics, 60 (1993) 199.

[91] http://www.see.ed.ac.uk/~jwp/newWork/Chemeng/Chemeng/water.html.

[92] X. Cheng, J. Zhang, Y. Tang, C.S.J. Shen, D. Song and J. Zhang, J. Power Sources, 167 (2007) 25.

[93] L. Zhang and S. Mukerjee, J. Electrochem. Soc., 153 (2006) 1062.

[94] Q. Dong, S. Santhanagopalan and R.E. White, J. Electrochem. Soc., 154 (2007) A816.

[95] R.P. Iczkowski and M.B. Cutlip, J. Electrochem. Soc., 127 (1980) 1433.

[96] M. Secanell, K. Karan, A. Suleman and N. Djilali, Electrochimica Acta, 52 (2007) 6318.

[97] W. Sun, B.A. Peppley and K. Karan, Electrochimica Acta, 50 (2005) 3359.

[98] K.-M. Yin, J. Appl. Electrochem., 37 (2007) 971.

[99] A.B. LaConti, M. Hanndan and R.C. McDonald, Mechanisms of membrane degradation, Wiley & Sons, Chichester, England, 2003.

[100] N.M. Markovic, H.a. Gasteiger and P.N. Ross, J. Phys. Chem., 99 (1995) 3411.

[101] J.S. Newman, Electrochemical Systems, Prentice-Hall, Englewood Cliffs, NJ, 1991.

[102] P. Ugo, L.M. Moretto, D. Rudello, E. Birriel and J. Chevalet, Electroanalysis, 13 (2001) 661.

[103] K. Mitsuda, NEDO Rep., FY. 1996, (1997) 90.

[104] Q. Wang, D. Song, T. Navessin, S. Holdcroft and Z. Liu, Electrochimica Acta, 50 (2004) 725.

[105] K. Schmidt-Rohr and Q. Chen, Nature Materials, 7 (2007) 75.

[106] D.W. McKee, Journal of Catalysis, 14 (1969) 355.

[107] H.F.M. Mohamed, K. Itoa, Y. Kobayashi, N. Takimoto, Y. Takeoka and A. Ohira, Polymer, 49 (2008) 3091.

[108] W. Noriaki, T. Masayuki, I. Masayuki, U. Hiroyuki and W. Masahiro, J. Electroanal. Chem., 574 (2005) 339.

[109] G.M. Haugen, F. Meng, N.V. Aieta, J.L. Horan, M.-C. Kuo, M.H. Frey, S.J. Hamrock and A.M. Herring, Electrochem. Solid-state Lett., 10 (2007) B51.

[110] S.J. Lee, S. Mukerjee, J. McBreen, Y.T. Rho and T.H. Lee, Electrochimica Acta, 24 (1998) 3693.

[111] H. Xu, R. Borup, E. Brosha, F. Garzon and B. Pivovar, ECS Trans., 6 (2007) 51.

[112] M.A. Hickner, H. Ghassem, Y.S. Kim, B.R. Einsla and J.E. McGrath, Chem. Rev., 104 (2004) 4587.

[113] S.A. Perusich, Macromolecules, 33 (2000) 3431.

[114] J. Qiao, M. Saito, K. Hayamizu and T. Okada, J. Electrochem. Soc., 153 (2006) A967.

[115] K.M. Cable, K.A. Mauritz and R.B. Moore, J. Polym. Sci. B 33 (1995) 1065.

[116] W.E. Delaney and W. Liu, ECS Trans., 11 (2007) 1093.

[117] A.B. LaConti, H. Liu, C. Mittelsteadt and R.C. McDonald, ECS Trans., 1 199.

[118] http://www.fuelcellmarkets.com/content/images/articles/nae101.pdf.

[119] A. Ohma, S. Yamamotoa and K. Shinoharaa, J. Power Sources, 182 (2008) 39.

[120] G. Hubner and E. Roduner, J. Mater. Chem., 9 (1999) 409.

[121] A. Buttafava, P.A. Guarda, G. Marchionni, R. Ronconi and A. Faucitano, J. Fluorine Chemistry, 114 (2002) 9.

[122] I. Dragutan and R.J. Mehlhorn, Free Radical Research, 41 (2007) 303.

[123] A. Samuni, S. Goldstein, A. Russo, J.B. Mitchell, M.C. Krishna and P. Neta, J. Am. Chem. Soc., 124 (2002) 8719.

[124] A. Panchenko, Journal of Membrane Science, 278 (2006) 269.

[125] W. Liu, K. Ruth and G. Rusch, J. New Mat. Electrochem. Sys., 5 (2001) 227.

[126] S. Prager, J. Chem. Phys. , 33 (1960) 122.

[127] S. Koter, J. Membrane Sci., 206 (2002) 201.